Resolution study of a Hyperspectral Sensor
using Computed Tomography
in the presence of Noise

DISSERTATION

Samuel V. Mantravadi, Major, USAF

AFIT/DEE/ENG/12-06

AFIT/DEE/ENG/12-06

RESOLUTION STUDY OF A HYPERSPECTRAL SENSOR
USING COMPUTED TOMOGRAPHY
IN THE PRESENCE OF NOISE

DISSERTATION

Presented to the Faculty

Graduate School of Engineering and Management

Air Force Institute of Technology

Air University

Air Education and Training Command

In Partial Fulfillment of the Requirements for the

Degree of Doctor of Philosophy
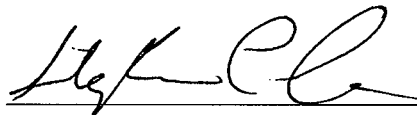
Samuel V. Mantravadi, BSEE, MSE

Major, USAF

June 2012

# RESOLUTION STUDY OF A HYPERSPECTRAL SENSOR USING COMPUTED TOMOGRAPHY IN THE PRESENCE OF NOISE
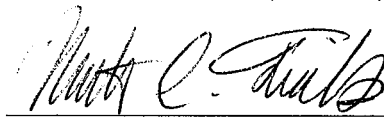
Samuel V. Mantravadi, BSEE, MSE

Major, USAF

Approved:

_____
Dr. Stephen Cain, PhD (Chairman)

_____3ᴐ May 2012_____
Date

_____
Dr. Richard Martin (Member)

_____30 May 2012_____
Date

_____
Dr. Matthew Fickus (Member)

_____30 May 2012_____
Date

Accepted:

_____
M. U. THOMAS
Dean, Graduate School of Engineering
and Management

_____12 Jun 2012_____
Date

## *Abstract*

A new type of hyperspectral imaging sensor is proposed, simulated and tested, which records both spectral and 2-dimensional spatial information. Dispersive imaging spectrometers typically measure multiple wavelengths and a single spatial dimension. Unlike dispersive imaging spectrometers, chromo-tomographic hyperspectral imaging sensors (CTHIS) record two spatial dimensions, as well as a spectral dimension, using computed tomography (CT) techniques with only a finite number of diverse images. CTHIS require a reconstruction algorithm in order to yield a usable hyperspectral data cube, and assume that the point spread function (PSF) is known. To date, the factors affecting resolution of these sensors have not been examined.

Lens-based CTHIS sensors use chromatic aberration of a lens and multiple images in varying levels of defocus to determine the chromatic scene of an object. This type of CTHIS sensor has many practical advantages including simplicity of its design and dual use as a broad band imager with no additional processing. The lens-based CTHIS concept has been largely unexplored up to this time. The results of this research effort serve to examine factors affecting the spectral and spatial resolution of a lens-based CTHIS sensor, specifically showing how many frames are needed to reconstruct the spectral cube of a simple object using a theoretical lower bound. In this research a new algorithm is derived and is used to successfully reconstruct a hyperspectral object in the presence of noise and background. This new algorithm is used to verify the number of frames predicted from the theoretical bound calculation using laboratory data, thereby demonstrating the validity of the bound calculation. Finally, a simple method is proposed and tested to use this sensor in the presence of atmospheric turbulence . This method is shown in simulation to successfully remove the effects of atmospheric turbulence and estimate the atmospheric seeing conditions blindly from raw lens-based CTHIS data.

## *Acknowledgements*

First and foremost, I owe a large debt of gratitude to my advisor Dr. Stephen Cain for his steadfast support in completing my dissertation, his ideas, and his wisdom.

I gratefully acknowledge the personal time given by many at the Air Force Office of Scientific Research in offering counsel in various aspects of the dissertation.

Finally, I wish to recognize the plethora of prayers, consistent support and constant encouragement of my family and family friends in completing this marathon, especially the love of my life.

Samuel V. Mantravadi

# Table of Contents

## List of Figures

## List of Tables

xi

## List of Symbols

## List of Abbreviations

# Resolution study of a Hyperspectral Sensor using Computed Tomography in the presence of Noise

## I. Introduction

### 1.1  Introduction

Imaging spectrometers have been used for multiple civilian and military applications for the last 20 years. Imagery obtained from these devices is useful since it contains both spectral and spatial information about the scene under observation. Imaging spectrometers measure the spectral content of a light source, utilizing either dispersive optics (such as prism or grating spectrometers) to spread the spectrum or Fourier transform spectra obtained by a scanning Michelson interferometer. These methods require scanning through either one spatial dimension (dispersive spectrometers - pushbroom or whiskbroom scanning), or the spectral dimension (Fourier transform spectrometers) to obtain a full spatial-spectral scene often referred to as a "data cube."

Recently a new method for generating spectral imagery has been developed which allows for simultaneous imaging of both spatial and spectral information using computed tomography (CT) algorithms. Such imagers typically are called Computed-Tomography Imaging Sensors (CTIS) or Chromo-tomographic Hyperspectral Imaging Sensors (CTHIS), although other names have been suggested. CTHIS use a dispersive element to project the 3D hyperspectral data cube multiple times onto a single 2D image or a few images (typically many fewer images than required for a pushbroom sensor). Multiple algorithms can be used to take these projection images and reconstruct the data cube generated from other imaging hyperspectral sensors. Unfortunately, the resulting resolution of the data cube can vary depending on the system setup and the reconstruction algorithm. This research will examine the effects of some

1

different parameters on the resolution for CTHIS, determine a lower bound to predict the number of defocus frames necessary to achieve a particular spectral resolution for a lens-based CTHIS, propose a method of reconstructing CTHIS in the presence of a large background, and verify this reconstruction method and lower bound using a laboratory experiment.

This dissertation is broken down into six sections. The first chapter will first examine previous work in the development of hyperspectral sensors, including CTHIS and the basic overall system designs and compare these sensor variations. Chapter I covers a description of the background material necessary to examining CTHIS performance. Chapter II develops the theoretical lower bound on CTHIS performance using the Cramer-Rao inequality (also called the Cramer-Rao Lower Bound or CRLB). Chapter III discusses the simulation parameters and setup of the lens-based CTHIS and develops a reconstruction algorithm. Chapter IV discusses the laboratory setup of the CRLB and how these were matched to the simulation described in chapter III. Chapter V discusses the results of the CRLB, the simulation and laboratory results of the resolution measurement and how the CRLB can be used as a parameter predictor for resolution performance in the presence of noise. Finally Chapter VI looks at a simple setup of a lens-based CTHIS simulation in the presence of an unknown atmospheric Point Spread Function (PSF) and a method for blind estimation of the atmospheric point spread function.

## 1.2  Uses of Spectral Imaging

Imaging spectrometers have been used for multiple applications including agriculture for urban planning, crop detection, mineral analysis, chemical signature detection, and environmental detection. The reflectance by various materials changes with respect to the wavelength of light incident on the material. As light is reflected from various materials, the waves mix additively to form a scene that may be imaged by a sensor. Typically sensors have very broad bands for visual imagery grouped into red (roughly $600 - 700$ nm), green ($500 - 600$ nm) and blue ($400 - 500$ nm). Hyper-
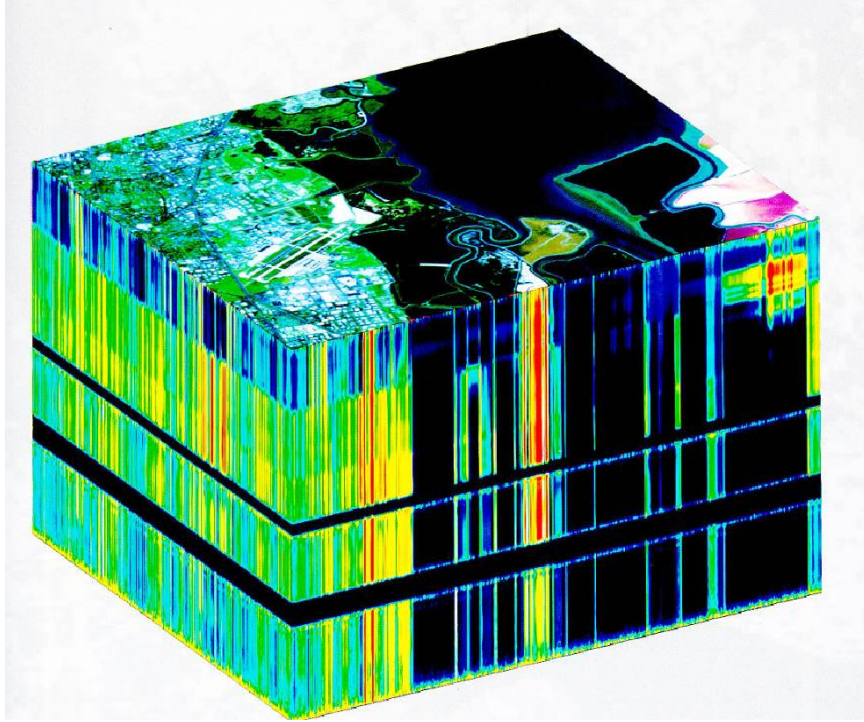
Figure 1.1:    AVIRIS Hyperspectral data cube of Moffet Field

spectral imagery defines these bands more narrowly and in more bands than typical visual imagery (as few as 5 to as many as 200 bands) that are typically contiguous. Figure 1.1 shows a picture from the Airborne Visual-Infrared Imaging Spectrometer (AVIRIS) which has approximately 200 bands from $400nm$ to $2.5\mu m$ [23]. Figure 1.1 includes two missing spectral bands (the image uses a pseudo-spectrum also known as false-color imagery). These missing bands correspond to wavelengths absorbed by the atmosphere due to water (top) and $CO2$ (bottom). Also, note the large red region in the upper right as this corresponds to a high density of shrimp in the pond near Moffet Field. Similar spectral features (such as the shrimp) can be used to determine where other materials of interest are. For instance, Figure 1.2 shows spectral imagery collected from a series of NASA satellites [24] indicating the growth of Las Vegas, Nevada from a small city in 1975 to a much larger urban area in 2009. The light green areas correspond to vegetation (usually golf courses or parks), the blue and dark gray areas correspond to cement (casinos and roads), the brown and white areas correspond to

3
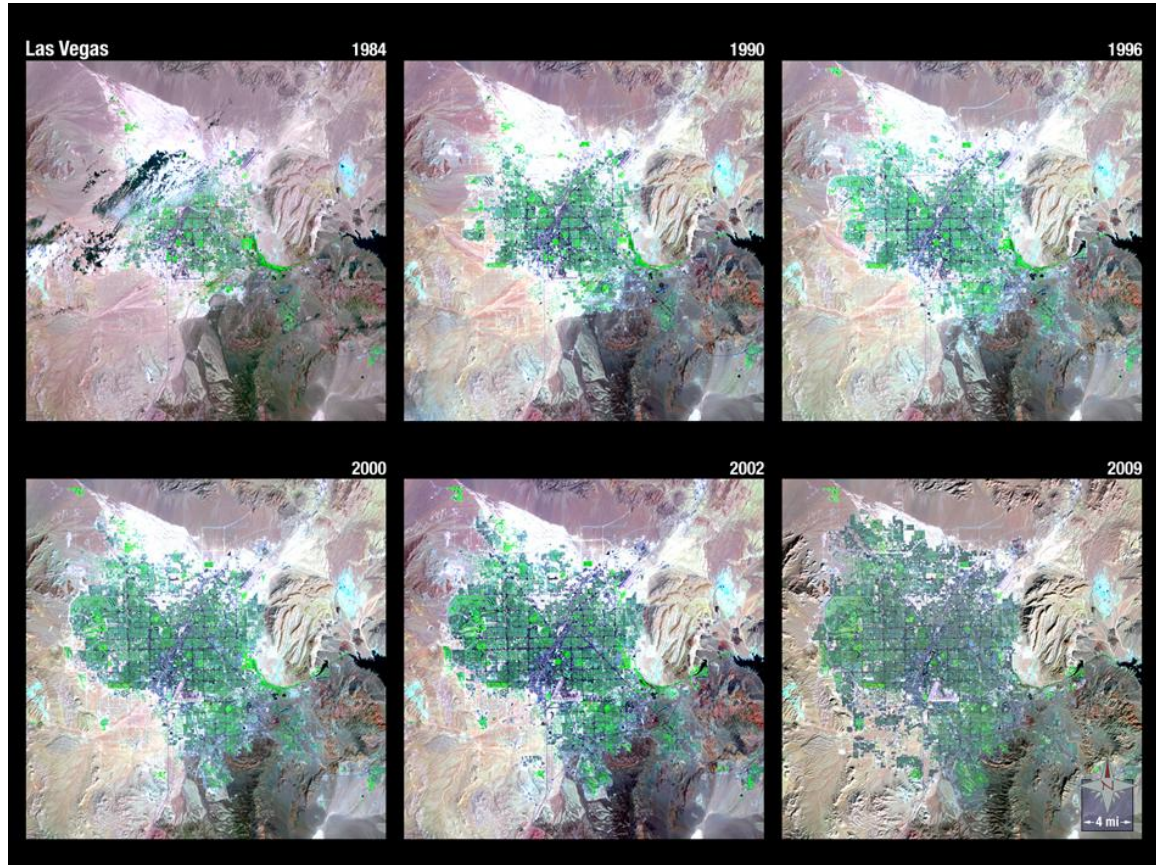
Figure 1.2:     Spectral Image showing urban sprawl in Las Vegas, NV over 1984-2009

different types of desert soil as well as some surface mining (open-pit) operations in the northwest of the city. This information from these pictures can be used by urban planners to determine where resources are or to plan the next phases of expansion of the city as the population grows. Similar data have been used in rural areas to determine materials for crop growth vs weeds [29] and by law enforcement or defense to determine the uncontrolled "farming" of illicit drugs in open areas [15,31]. Figure 1.3 is another example of spectral imagery (taken from [33]) shows the east coast of the United States. Central Park can be seen in the upper right hand corner as a black dot surrounded by green, which is surrounded further by dark grey corresponding to the Manhattan city streets where the Hudson and East rivers come together between Long Island and Manhattan. The black dot is the Jacqueline Kennedy Onassis Reservoir on the northern edge of Central Park. These data also have been used to determine

4

Figure 1.3:     False color image of Philadelphia, New York and New Jersey
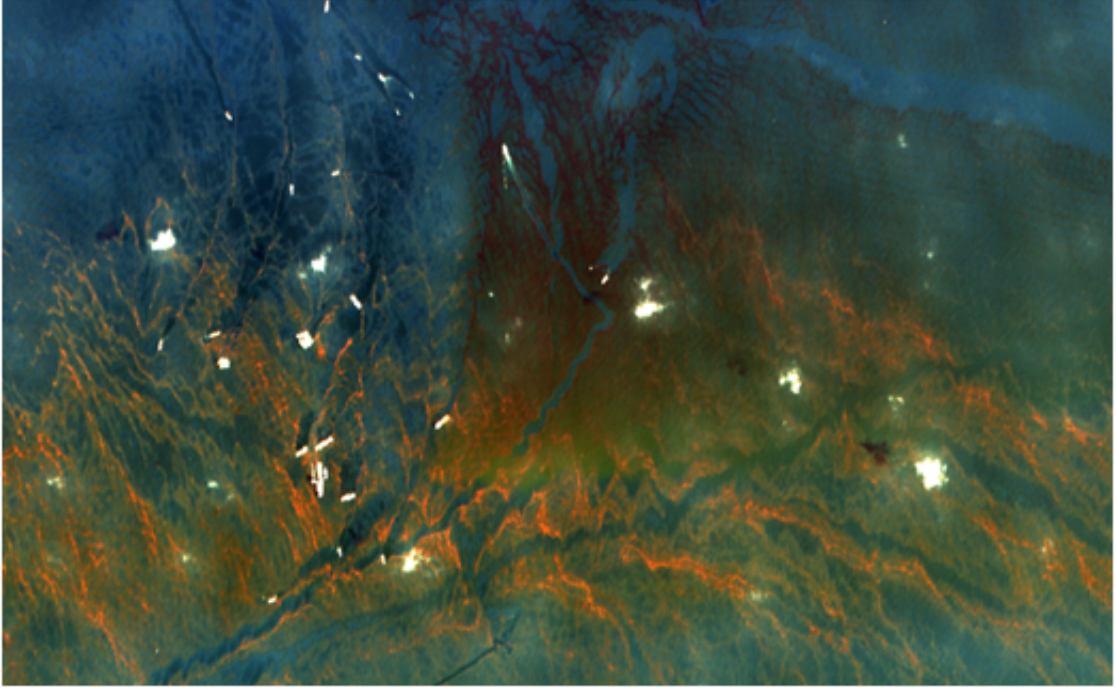
Figure 1.4:    Combined Visual/Hyperspectral image showing the Gulf of Mexico Oil spill 2010

mineral content under the presence of other materials (such as soil [4] or water [1]). Figure 1.4 shows an oil spill in the Gulf of Mexico in 2010. The oil spill is marked in yellow, while the sea is shown with standard visual spectrum colors to show stark contrast where oil is present. Figure 1.5 shows how the data was collected to make the image. Hyperspectral data were collected in 20 runs over the Gulf of Mexico using the AVIRIS sensor. AVIRIS can collect data at wavelengths from $370nm$ to $2.5\mu m$ [1]. AVIRIS is a type of sensor geometry called "pushbroom" sensing. The next section details how conventional hyperspectral imagers have been designed.

## 1.3   Design of Hyperspectral imagers

Several designs for hyperspectral imagers have been proposed, which fall mainly into two categories, dispersive imaging spectrometers and Fourier transform spectrometers. Dispersive imaging spectrometers disperse light typically by using a prism or diffraction grating, image a single spatial dimension and spread the spectrum across

6
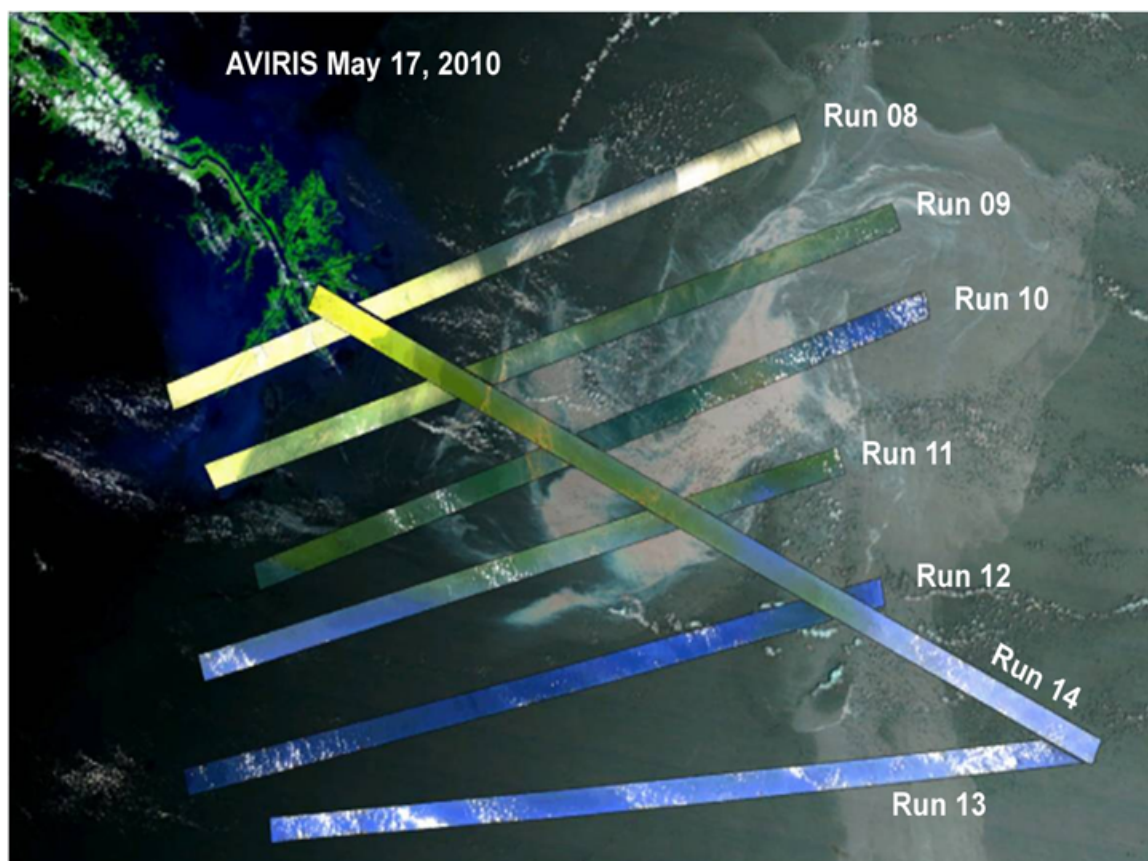
Figure 1.5:    Overplot of AVIRIS flights with visual imagery
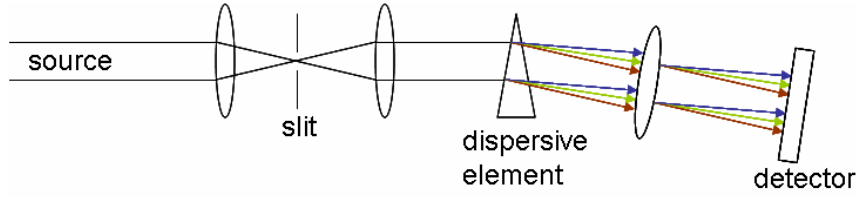
Figure 1.6:    A typical hyperspectral imaging sensor

a detector in the other dimension. Figure 1.6 shows a schematic for an imaging spectrometer using a prism. The slit is imaged through the prism onto the detector. The slit represents the single spatial dimension, and the spectrum is spread perpendicular to the slit onto the detector. Platform motion is used to develop a scene one line at a time. In a pushbroom configuration (see figure 1.7 for a typical pushbroom sensor configuration) as the platform moves perpendicular to the slit, the collection of lines imaged through the slit produces a hyperspectral data cube. Figure 1.11 gives a detailed sensor schematic for a pushbroom sensor. The $x$ dimension from Figure 1.7 is the same as the $x$ dimension in Figure 1.11. A simulated hyperspectral scene is shown in Figure 1.9 using spectra from the Advanced Spaceborne Thermal Emission and Reflection Radiometer (ASTER). ASTER data are available through a NASA website and can be searched according to material [22]. Figure 1.8 shows spectra for cement, glass and deciduous foliage. An output from a pushbroom sensor for the scene in 1.9 image of line 128 (the center of the image) can be seen in figure 1.10. These spectra were chosen because they reflect large portions materials in the image. The glass in Figure 1.10 in the infrared range corresponding to $8 - 12\mu m$ wavelengths although the deciduous foliage also mixes with the spectra in the same area. Deciduous foliage has a unique peak between $3.5 - 5\mu m$ which can be seen by yellow peaks in the pushbroom scene in Figure 1.10. And, hardly detectable without some processing (but conspicuous by its absence between the windows) is the cement with its notch around $1.4\mu m$. The cement between the windows can be seen in the low intensity areas around $11\mu m$ between the glass from the windows. There are about ten windows in the scene across the center, although the central four are obscured

8
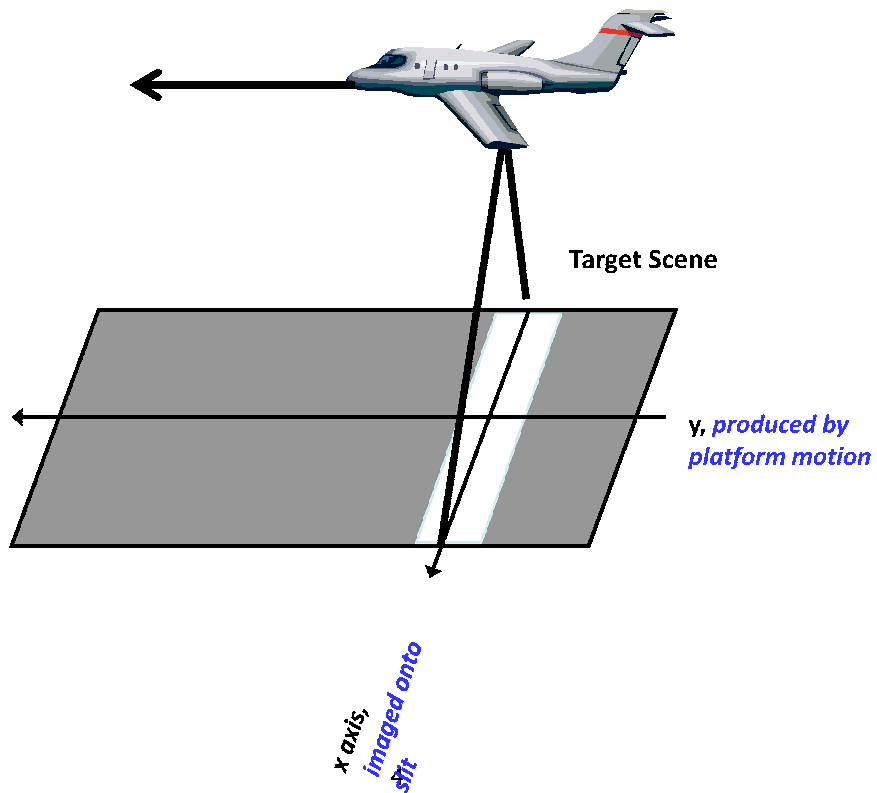
Figure 1.7:     Pushbroom Sensing Geometry
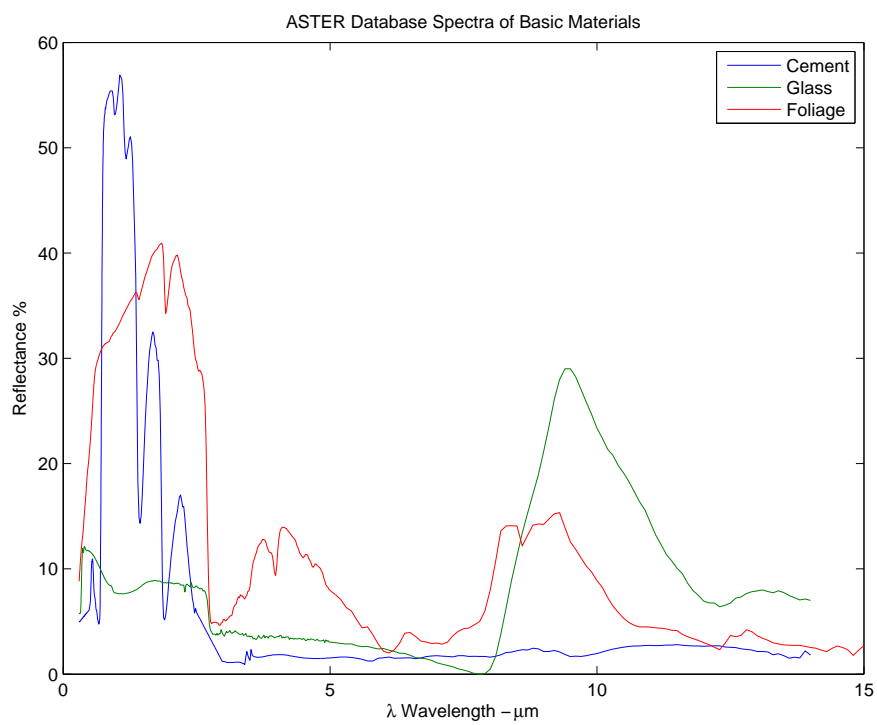


Figure 1.8:     Simulated hyperspectral scene using ASTER spectra

False Color Image of Building with Foliage
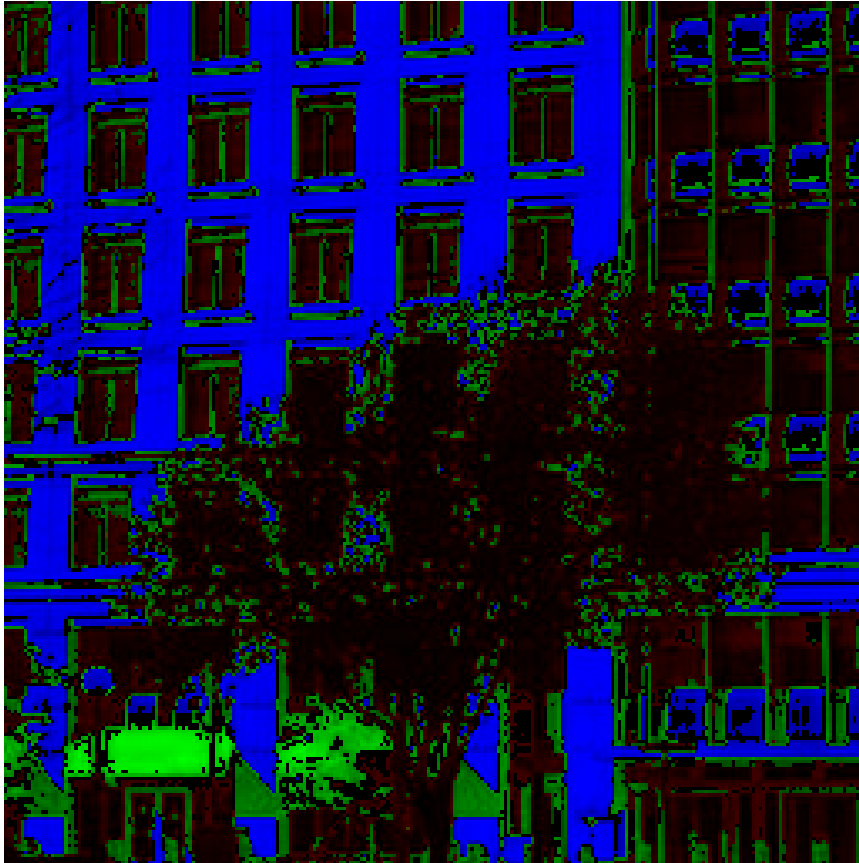


Figure 1.9:     Simulated hyperspectral scene using ASTER spectra

by foliage, and all have metal window panes (seen by the small lines in between the glass spectra. Another method of computing the spectrum of a scene involves using interferometers.

A Michaelson interferometer can determine the spectrum of an object. Light from a target scene is transmitted through a beam splitter which sends the light down two equidistant paths, with mirrors in each path and then mixed resulting in an interference pattern seen on the detector. A single mirror (called the scanning mirror) is moved to produce constructive and destructive interference. As the interferogram changes along with the motion of the scanning mirror, a profile of intensity is built up at each pixel on the detector. In a Fourier Transform Imaging Spectrometer (FTIS), the one-dimensional Fourier transform the intensity profile on each pixel is taken, and

10
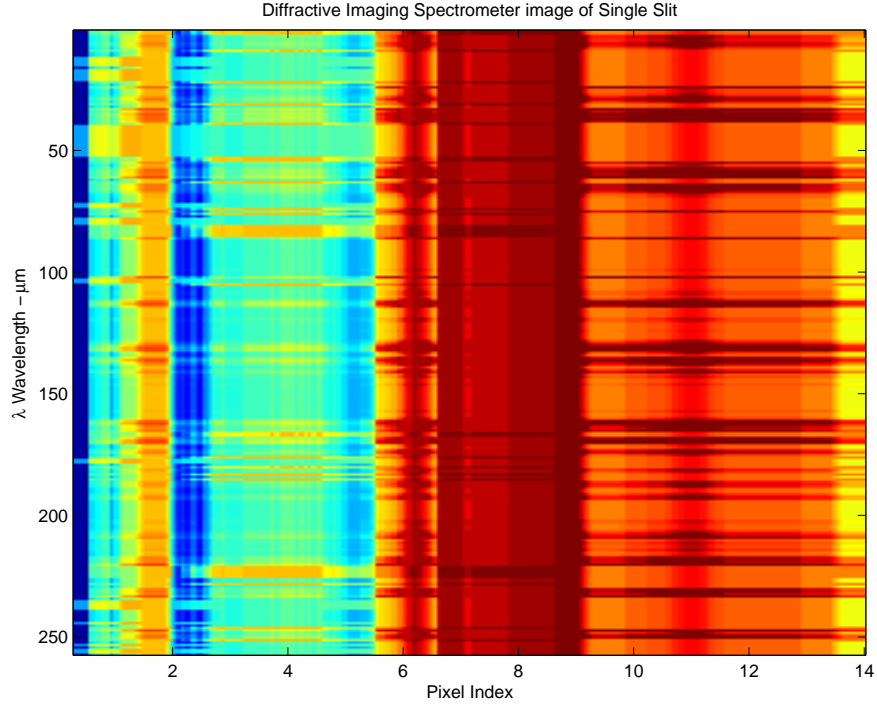
Figure 1.10:    Simulated hyperspectral image taken by a pushbroom sensor

the spectrum is derived by correlating this to the position of the scanning mirror. An example of the intensities seen by a pixel is given in Figure 1.13 using the same line as given in Figure 1.10. As the mirror is moved, the intensity on each pixel yields a spectrum correlated to the optical path length difference of the two legs. The center peak of figure 1.13 is the maximum intensity and corresponds to an optical path difference ($\Delta_{opd}$) of 0. The equation for the intensity $I(\Delta opd)$ seen by the FTIS is given by:

$$I(\Delta_{opd}) = \int_0^\infty I(\lambda) \left[ 1 + \cos\left(\frac{2\pi}{\lambda}\Delta_{opd}\right) \right] d\lambda \tag{1.1}$$

The intensity per wavelength spectra ($\lambda$) seen by each pixel can be reconstructed by using the inverse Fourier Cosine Transform by:

$$I(\lambda) = 4 \int_0^\infty \left[ I(\Delta_{opd}) - \frac{1}{2}I(\Delta_{opd} = 0) \cos\left(\frac{2\pi}{\lambda}\Delta_{opd}\right) \right] d\Delta_{opd} \tag{1.2}$$

 The dispersive imaging spectrometer has the advantage that the spectra are imaged directly, and the result can be understood directly if there is not a lot of clutter.

11
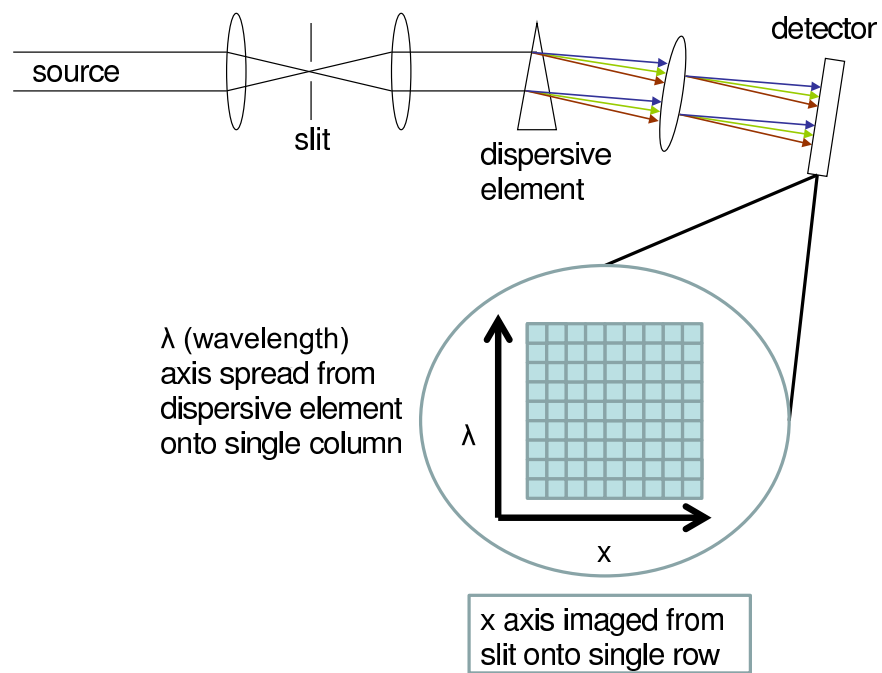
Figure 1.11:     Detailed sensor schematic for pushbroom hyperspectral data cube

.
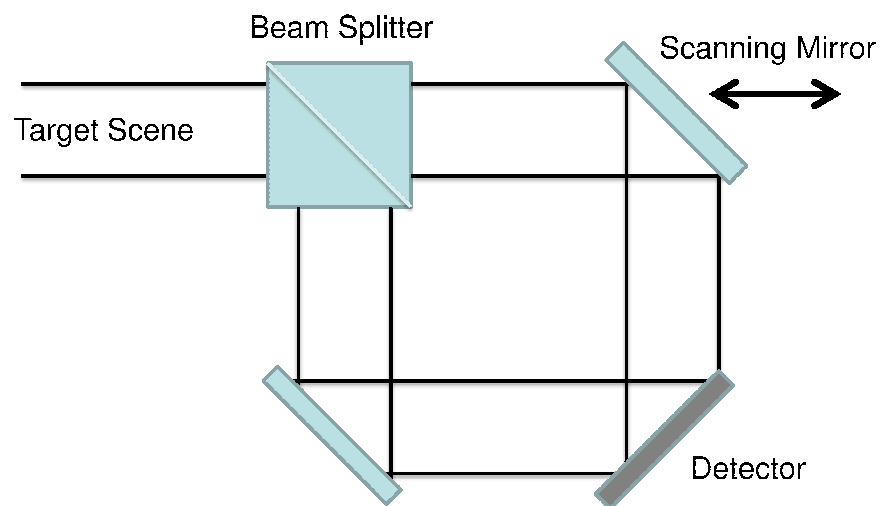


Figure 1.12:     Fourier Transform Imaging Spectrometer

Also, the imager takes advantage of the platform using the motion to form an image, which is beneficial for both air platforms and satellites. The number of spectra is fixed, but can be designed to have relatively high spectral resolution, however this resolution is fixed with the sensor design parameters. The FTIS can be configured to have an arbitrary spectral resolution depending on how finely the optical path length difference $\Delta_{opd}$ is controlled by the sensing mirror. This means that the sensor can be tuned for a very high spectral resolution, or a coarse resolution depending on the needs of the data collection. FTIS have a disadvantage of requiring a significant amount of precision in the setup and a stable platform to keep the precise orientation of the two paths of the interferometer.

Another main disadvantage of these spectrometers is that they both throw away a significant amount of light. Dispersive imaging spectrometers disregard any light outside of the slit and therefore need a significant amount of light in a scene. FTIS lose at least 50% of the incoming light, because the light gets reflected out of the front of the imager. The CTHIS originally were designed to take advantage of as much of the incoming light from a scene as possible.

## 1.4 Previous Work

*1.4.1 Early Work.* The use of tomographic imaging techniques for reconstructing images with two spatial and a third spectral dimension was postulated first by Levin and Vishnyakov [16]. Later, Okamoto and Yamaguchi [26] experimentally demonstrated the first chromotomographic sensor using a series of amplitude diffraction gratings yielding a diffraction efficiency constant over all wavelengths of interest. Later that same year, Levin et al. [3] demonstrated a simple one-dimensional reconstruction using prisms with variable dispersion believing they were the first to demonstrate the concept. Okamoto, et al. [25] used phase diffraction grating, yielding even more light, at the expense of a more complex reconstruction technique because, in this case, diffraction efficiency is dependent on wavelength. Compared to techniques developed by later work, simple algebraic reconstruction techniques were used similar
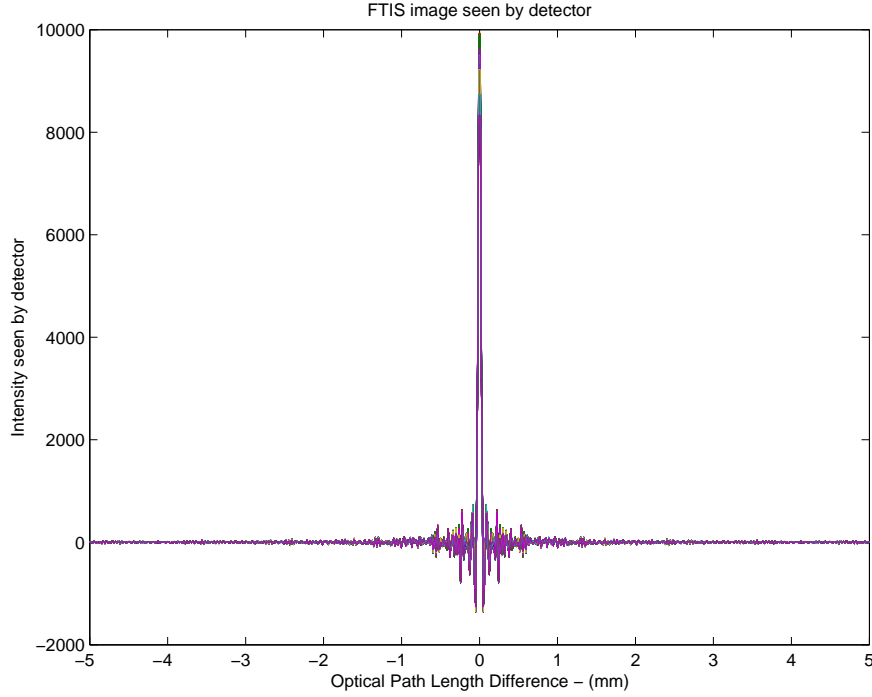
Figure 1.13:    Detailed sensor schematic for pushbroom hyperspectral data cube

to other computed tomography problems. However, both groups demonstrated the advantages of a chromotomographic sensor's potential for high optical throughput and the ability to image flash events over other spectral sensors. The disadvantage of these designs is that, while they are simple, they do not offer significant spectral resolution when compared with dispersive imaging spectrometers or FTIS.

*1.4.2   Crossed Phase Gratings.*    Descour and Dereniak [7] detail experimental results of a CTHIS using a series of crossed phase gratings. Their work can be seen as extended the work of Okomoto and Yamaguchi to an even larger number of wavelengths by using a statistical reconstruction technique. The authors further developed the theory of CT sensing using a discrete-to-discrete method for reconstructing the object cube that takes into account noise sources and diffraction efficiency. In  [7], a filter was used to reduce the spectral range of the orders allowing multiple diffraction orders to be detected, because these multiple orders correspond to differing angle projections of the hyperspectral data cube and therefore contain different information.

14

In [8], the authors use a computer generated hologram as a dispersion element which is specifically designed for diffraction efficiency and image location. The advantage of using diffraction gratings and holograms specifically designed for CTHIS extended the possibilities of this sensor to real-world applications rather than a simple laboratory setup [14], and also that these sensors can image flash (one-time) events. One of the disadvantages of using diffraction gratings is the inconsistent spectral efficiency at all wavelengths (the sensor will be more sensitive at some wavelengths than others). This was the first demonstration in the literature of a real-world use of a CTHIS, however as referenced in [14] there were significant issues that needed computer processing to recover the actual imagery, and some of this was directly due to the design of the sensor.

*1.4.3 Direct Vision Prism.* In [21], Mooney details a CTHIS design differing from earlier work using a rotated direct vision prism in order to sample the spatial-spectral object cube. All earlier work used a diffraction grating, or a series of prisms with different dispersions in order to change the angle sampling the object cube. The DV prism differs from a standard prism in that the central wavelength passes through without any angular deviation [20, 21], while a known angular dispersion is applied to other wavelengths. Using a DV prism also opens up an interesting opportunity to calculate vector-based images, similar to a linear dispersive imaging spectrometer [12]. This method differs from a standard CTHIS (using a DV prism) only by software and can be useful in quickly determining scenes of interest which can then be imaged using the standard DV prism CTHIS reconstruction. The disadvantage of these sensors is that they require multiple snapshots of a scene to be effective whereas the diffraction-based CTHIS sensors can image flash events.

*1.4.4 Chromatic Lens Aberration.* In [17] Lyons proposed the use of a diffractive optic element specifically designed to focus wavelengths to varying distances similar to a Fresnel lens. This research used simple images directly to determine the spectral content correlating that with the position of the lens. This element yields
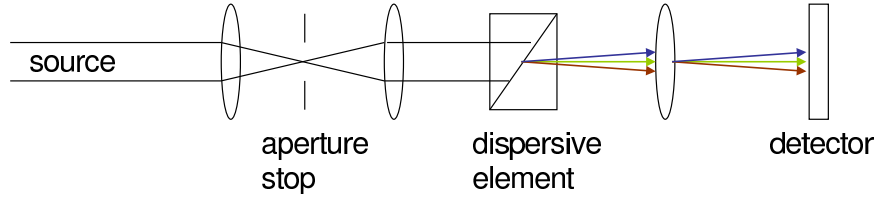
Figure 1.14:    design of a chromotomographic imaging sensor

a small change in the focus distance yielding large change in the focal length, but has the disadvantage of having a large changes in diffractive efficiency at different wavelengths. In [5] Cain also proposed using the chromatic aberration of a lens as a dispersion element and moving the images in and out of focus for successive wavelengths to capture multiple images. This has the advantage of a simple optical setup rather than using expensive optics for the dispersion element. Also, using this method, an existing optical system can be turned into a CTHIS using only slight modifications, such as the addition of a telescoping lens and an aperture stop. The disadvantage to this method is that the magnification changes with respect to each wavelength may need to be accounted for in the reconstruction depending on the lens. Also, this design suffers from the same disadvantage of direct vision prisms requiring multiple frames in order to compute a spectral scene.

## 1.5    CTHIS sensor design

The basic motivation for CTHIS is twofold: first, to make use of all available light and second, to reduce or eliminate the amount of scanning necessary. Typical dispersive imaging spectrometers make use of a slit which is re-imaged onto the detector. Figure 1.6 shows the design of a standard dispersive imaging spectrometer. This slit is typically the size of a single line of pixels. A typical CTHIS detector replaces the slit with a wider field of view field stop (figure 1.14), and the dispersion element with either a specially made diffraction grating or a direct vision (DV) prism.

Two methods can be used for capturing spatial-spectral frames for computed tomography, single-frame and multi-frame detection. Single-frame designs for a CTHIS
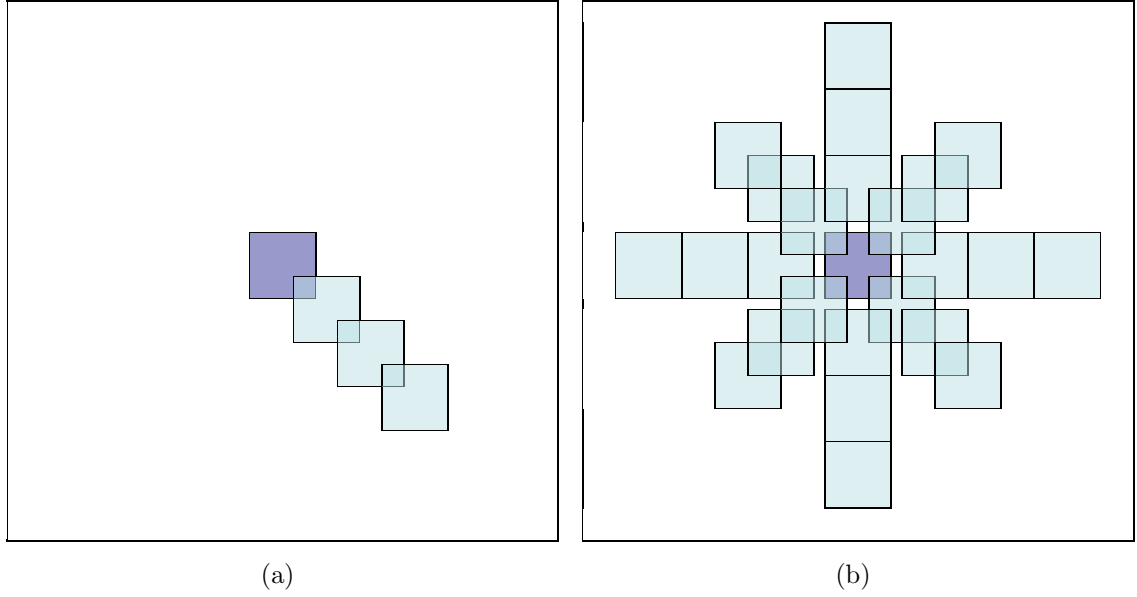
Figure 1.15: (a) a prism projects an object along a single prism axis, (b) a grating projects an object along multiple axis simultaneously

differ significantly from dispersive imaging spectrometers in that the gratings are designed to diffract light in two dimensions and over multiple diffraction orders. A single-frame design also has the added advantage of being able to capture all wavelengths at a single time. In [7], a filter was used to reduce the spectral range of the orders, allowing multiple diffraction orders to be detected, because these multiple orders correspond to differing angle projections of the hyperspectral data cube and therefore contain different information. The gratings (or other suitable diffraction element) designed for each of these configurations [7,8,34] were chosen to maximize the amount of light in each diffracted order used and to maximize the detector area used to capture CTHIS frames. However, since the goal is to spread multiple orders over the entire detector, diffraction efficiency is not constant with respect to wavelength or order.

In multi-frame detection, a DV prism is designed such that some center wavelength $\lambda_0$ (or the whole multi-color scene) passes through without deviation. Multiple frames are collected by rotating the prism along the axis of the undeviated wavelength (figure 1.15(a) [21]). DV prisms are generally manufactured from 2 prisms with dif-

ferent indices of refraction which cancel out the angular dispersion at the center wavelength. The object and viewing conditions are assumed to be constant during the rotation of the prism. The number of frames required can be much fewer than those required for scanning of other spectrometers. Pushbroom dispersive imaging spectrometers require the number of frames to be the spatial pixels in the scanning direction and Fourier transform spectrometers require the number of frames to vary as the total bandwidth of interest. Also of note is that keeping a single prism aligned should be much simpler than keeping two arms of an interferometer aligned, so the scanning of a DV prism CTHIS is a reduction in complexity over a Michelson-based Fourier transform spectrometer. CTHIS scanning is only required to adequately sample the projections of the data cube. Figure 1.16 shows an example of a DV prism as the rotation varies. Note that in this picture $\lambda_2$ represents the undeviated wavelength. As will be seen in the algorithms discussion, there is inherently some missing information in CTHIS data which must be reconstructed. This missing information can be traded off with processing time and estimated vs. measured resolution. The main disadvantage of using a DV prism is that they are difficult to manufacture, and may be expensive depending on the wavelengths of interest.

Another method using a multi-frame design is to use the chromatic aberration of a lens to achieve dispersion. Due to chromatic aberration, the focal length of the lens will be dependent on wavelength. A central wavelength for the lens is chosen, and the lens position is varied around the corresponding focal length. Note that in figure 1.15 that the dark square represents a single undeviated wavelength for the prism in (a), and corresponds to a sum over all wavelengths using the grating in (b).

## 1.6 Reconstruction Algorithms

Having discussed the basic design of a CTHIS, we now turn our examination to the reconstruction of the data cube. The processing is an essential step to using CTHIS imagery because without it, the spatial and spectral data are multiplexed in the image. The reconstruction mathematics borrow heavily from the already estab-
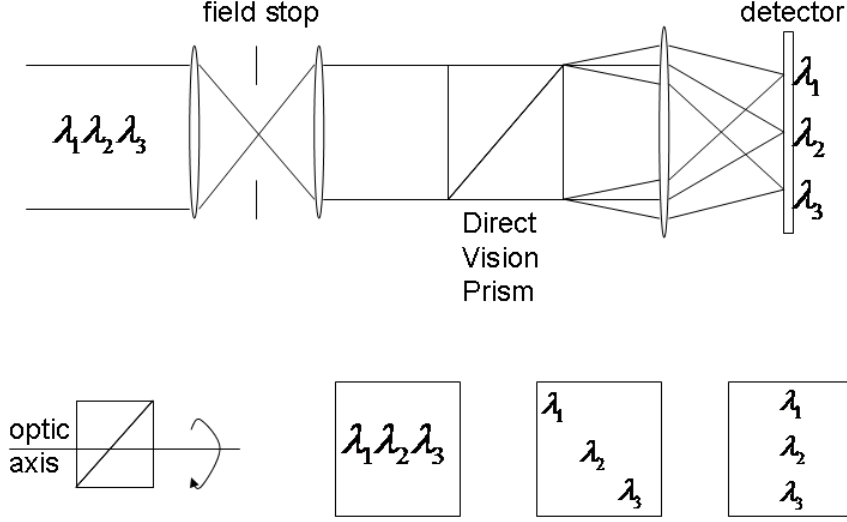
Figure 1.16:    Example of a DV prism in a CTHIS sensor

lished world of computed tomography, using many of the mathematical formulations applied to medical imaging, Synthetic Aperture Radar and other applications. Although some of the mathematical underpinnings from may be borrowed from CT, some parts of the reconstruction problem still require special considerations in order to accurately reconstruct the data cube. CTHIS suffer from a fundamental limitation in that the projection into the image plane cannot fully cover the information necessary to directly reconstruct the data cube. Methods have been proposed to overcome this limitation based on principle component analysis (PCA) and projections onto convex sets [20, 21]. We will first look at the reconstruction problem, followed by the problem areas associated with reconstruction. Then we will discuss reconstruction algorithm types, and finish this section with a discussion of comparisons and contrasts between the different algorithms.

*1.6.1 Algebraic Reconstruction.*    In [25], Okamoto and Yamaguchi develop the equations for the images seen by a single frame grating-based CTHIS. Using $x,y$ as index variables in the imaging plane, $\lambda$ as the wavelength, $o(u, v, \lambda)$ as the object, and $u,v$ as spatial coordinates in the object plane, an image seen by the detector is

19

given by:

$$i(x, y, \lambda) = \int_u \int_v o(u, v, \lambda)h(x - u, y - v, \lambda)dudv \tag{1.3}$$

where $h(x, y, \lambda)$ is the point spread function of the imaging system. In this case, the standard grating equation can be used, and yields:

$$h(x, y, \lambda) = \sum_{j,k=-1,0,1} \eta_{jk}(\lambda)\delta\left(x - \frac{\lambda u}{\Lambda}k, y - \frac{\lambda v}{\Lambda}k\right) \tag{1.4}$$

where $\eta_{j,k}$ are the diffraction efficiencies of the $j$th and $k$th diffraction orders, $\Lambda$ is the grating constant, and $\delta$ is a Dirac delta function. In [26], only the $-1, 0, 1$ diffraction orders were considered. Finally the noise-free signal detected by the imager is given as a simple example by:

$$i(x, y) = \int a(\lambda)i(x, y, \lambda)d\lambda = \sum_{j,k=-1,0,1} \eta'_{j,k}(\lambda)o\left(x - \frac{\lambda u}{\Lambda}j, y - \frac{\lambda v}{\Lambda}k, \lambda\right) \tag{1.5}$$

where $\eta'_{jk}$ is the product of diffraction efficiency $\eta_{jk}$ and corresponding detector spectral response $a(\lambda)$. The reconstruction given in [25] is a modified algebraic reconstruction technique (MART) which is an iterative technique useful for small number of projections. Setting an initial object estimate $o^0(x, y, \lambda)$ to a positive constant, successive object estimates are then calculated by iterating over:

$$o^{q+1}(x, y, \lambda) = \left(\frac{i(x, y)}{i^q(x, y)}\right) o^q(x, y, \lambda) \tag{1.6}$$

where $i^q(x, y)$ is the projection of the $q$th estimate of the signal and is recalculated using equation (1.5) with the $q$th estimate of the object. This algorithm is similar to the maximum likelihood estimator given in section 1.6.3.

*1.6.2 Projections onto Constraint Sets.* If the optical setup is based on the DV prism as in [20, 21], the formulation of the reconstruction becomes a convolution of multiple wavelengths with respect to each rotated frame. In [21], a DV prism setup with three separate wavelengths and four separate frames the forward model is given

by:

$$i_1(x,y) = h_{1,1}(x,y) * o_1(x,y) + h_{1,2}(x,y) * o_2(x,y) + h_{1,3}(x,y) * o_3(x,y)$$

$$i_2(x,y) = h_{2,1}(x,y) * o_1(x,y) + h_{2,2}(x,y) * o_2(x,y) + h_{2,3}(x,y) * o_3(x,y)$$

$$i_3(x,y) = h_{3,1}(x,y) * o_1(x,y) + h_{3,2}(x,y) * o_2(x,y) + h_{3,3}(x,y) * o_3(x,y)$$
(1.7)

$$i_4(x,y) = h_{4,1}(x,y) * o_1(x,y) + h_{4,2}(x,y) * o_2(x,y) + h_{4,3}(x,y) * o_3(x,y)$$

Where $o_m(x,y)$ is the spectral distribution corresponding to band $m$, $i_k(x,y)$ is the data recorded for the prism orientation $k$, $h_{k,m}(x,y)$ is the point spread function for spectral band $m$, with respect to prism orientation $k$ and the convolution operator is represented by the $*$. The summation form of (1.8) is given by:

$$i_k(x,y) = \sum_{m=1}^{N} h_{k,m}(x,y) * o_m(x,y)$$
(1.8)

A geometrical optics model for $h_{k,m}(x,y)$ [21] is given by:

$$h_{k,m}(x,y) = \delta[x - (k - k_0\Delta\cos(\phi_m)), y - (k - k_0\Delta\cos(\phi_m))]$$
(1.9)

where $k_0$ is the index of the initial prism orientation, $\Delta$ is an offset defined by the prism geometry, and $\phi_m$ is the angle for spectral band $m$ defined by the prisms relative index of refraction. In the Fourier domain, the rotation's spatial spectra are a product of the original spatial spectra multiplied by the optical function. Taking the Fourier transform representation of (1.8) using matrix notation becomes:

$$I(\xi,\zeta) = H(\xi,\zeta)O(\xi,\zeta)$$
(1.10)

where the $O$, $I$, and $H$ are the Fourier transforms of $o$, $i$, and $h$ respectively. The problem then becomes a larger number of inversions of smaller matrices which is the motivation for separating the projections over multiple prism rotations rather than a larger matrix inversion necessary for a single-frame approach. For instance, in [21],

21
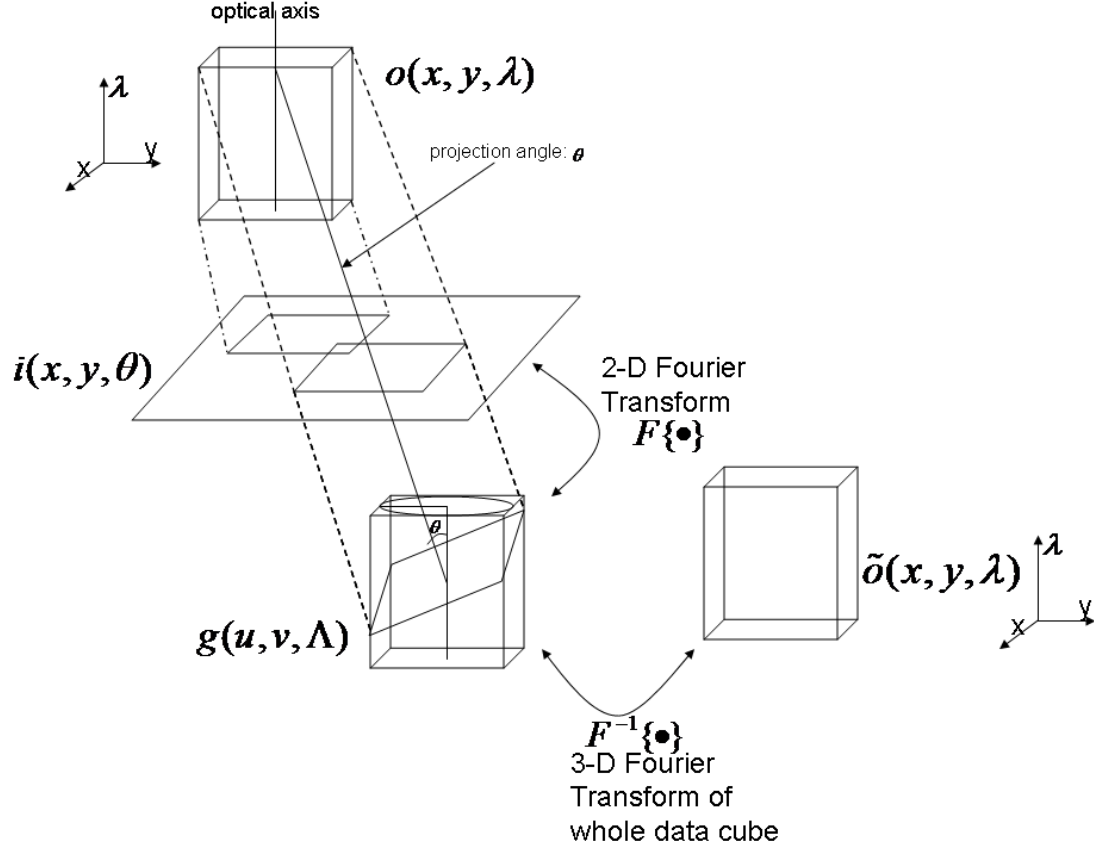
Figure 1.17:    Example of 3-D object reconstruction using Fourier transforms

the authors solve "50 240×240 spectral images from 80 240×240 images using 57600 80×50 matrix inversions rather than a single 4,608,000×2,880,000 matrix inversion" necessary for the same problem using a grating rather than a DV prism. This formulation directly correlates the spectral Fourier transform with the measured data. The Fourier transform exhibits a special property known as the projection-slice theorem, the Fourier slice theorem or the central slice theorem, all of which state that the Fourier transform of a projection can be used as slices through a higher-dimensional Fourier space (see figure 1.17).

The $H$ matrix and its pseudoinverse can be precomputed and stored. The pseudoinverse of $H$ can also be diagonalized using the singular value decomposition and the forward and inverse Fourier transform can be directly applied. Inverting the $H$ matrix is less complex computationally than inverting the similar matrix mentioned

22

in [7] because the matrices can be diagonalized due to the layout of the DV prism CTHIS. Diagonalizing $H$ yields:

$$H = UWV^{\dagger} \tag{1.11}$$

where $W$ is a weighted diagonal matrix according to equation 1.12, and $U$ and $V$ are the weighting matrices needed for the product to equal $H$. This is also the singular value decomposition (SVD) of $H$, where $U$ and $V$ are unity when multiplied by their transpose conjugate (also called the Hermetian adjoint). Inverting (1.11) and substituting back in to equation (1.10) we find equation (1.13) in which the inverse of $W$ (elements referred to as $w_{i,j}$)) is replaced by $\widetilde{W}^{-1}$ (elements referred to as $\widetilde{w}_{i,j}$) where the small singular values elements of $W^{-1}$ are replaced with:

$$\widetilde{w}_{i,j}(\xi, \zeta) = \frac{w_{i,j}(\xi, \zeta)}{w_{i,j}^2(\xi, \zeta) + \eta^2} \tag{1.12}$$

so as not to amplify noise. In this case, $\eta$ is a tuning parameter (dependent on noise, data and sampling) generally close to unity.

$$\widetilde{O} = V\widetilde{W}^{-1}U^{\dagger}I \tag{1.13}$$

In practice however, the direct matrix inversion (or pseudo-inverse) is not solely the solution to the reconstruction problem, but it is used as an estimate to determine the input to an iterative algorithm which then calculates the reconstruction. We can make use of the relationship between the Fourier domain and the captured images [2] to construct a simple iterative algorithm. For the rest of this development, we assume that we can reorganize the two-dimensional matrices as single-dimensional vectors to simplify notation. By adding the forward and inverse Fourier transforms to $H$, adding noise, and expanding the psuedoinverse, equation (1.8) becomes:

$$i = F^{-1}UWV^{\dagger}Fo + n \tag{1.14}$$

where $n$ is a noise vector, and $F, F^{-1}$ are the forward and inverse Fourier transforms respectively. Our iterative estimate of $o$ becomes:

$$\widetilde{o}_j = F^{-1}F[L\widetilde{V}^{-1}U^{\dagger}Fi + Rv^{\dagger}FF\widetilde{o}_{j-1}] \tag{1.15}$$

where $L$ and $R$ are diagonal with elements:

$$L_{i,j}(\xi, \zeta) = \frac{w_{i,j}^2(\xi, \zeta)}{w_{i,j}^2(\xi, \zeta) + \beta^2} \tag{1.16}$$

$$R_{i,j}(\xi, \zeta) = 1 - L_{i,j}(\xi, \zeta) \tag{1.17}$$

This algorithm doesn't directly take into account fixed pattern noise of the focal plane array (FPA), however the authors note that typically these errors get mapped to the undeviated (central) spectral band. In [20] Brodzick and Mooney further generalize the model developed in [21] and note that it is of a class of algorithms called projections onto convex sets (POCS). One POCS algorithm that is also well-known is the Gercheberg-Papoulis algorithm, and is similar to the generalization of the algorithm mentioned in [21]. Their derivation amounts to projecting the Fourier domain along the principle component axes of the range space (the known portion) of the system transfer function matrix $H$ (called $A$ in [20] and $P$ in [21]) and the projection of the unknown portion into the null space of $H$. This null space projection is called the transform domain constraint. Then the algorithm uses the fact that the object domain (the hyperspectral data cube) has a high degree of correlation between bands. This redundancy can give an advantage by using the PCA projection of the object domain along the principle components to fill in the unknown portion of the frequency domain. By using PCA, the algorithm is forcing the Fourier domain data to be consistent with the object domain principle component projection. This second constraint is called the object domain constraint and is a generalization of [21]. Small singular values of this constraint correspond to a loss of information. This algorithm effectively iterates between projections in the object plane and back to the Fourier

24

plane to determine the CTHIS reconstruction similar to the popular Gercheberg-Saxton algorithm which is another type of POCS algorithm [9].

*1.6.3 Maximum Likelihood Estimators.* In [7] Descour and Dereniak simply propose mapping each volumetric element (voxel) from the data cube to the pixel projection in the image plane. They experimentally determined the system transfer matrix $H$:

$$d(x, y) = h(x, y, \lambda) * o(x, y, \lambda) + n(x, y) \tag{1.18}$$

where $d(x, y)$ is the sensed data, $o(x, y, \lambda)$ is the spatial-spectral object, and $n(x, y)$ is a noise vector. Equation (1.18) directly maps the discrete image pixels to their discrete object voxel counterparts. Descour et al. [7] chose to use a monochrometer and physically translated the input at each $(x,y)$ value determining the point spread function $(h(x, y, \lambda))$ directly (each voxel to pixel projection forms a single PSF). This step maximizes the probability density of the object given the data $Pr(o|d)$ iteratively (equation (1.19)) with a stopping criterion such that the quotients go to unity, or when $||d(x, y) - h(x, y, \lambda) * o(x, y, \lambda)||$ is minimized below a certain threshold.

$$o^{k+1}(x, y, \lambda) = o^k(x, y, \lambda) \sum_{m=1}^{M} h_m(x, y, \lambda) * \frac{d_m(x, y)}{d_m^k(x, y)} \tag{1.19}$$

In this step $d_m^k(x, y)$ is the estimate of the noisy data using the object calculated in the previous iteration.

## 1.7 Reconstruction Problems

Even with algorithms for image reconstruction understood, there are still some problems which make it difficult to completely restore all of the information about the object. The fact that the sensor cannot fully control the orientation of the object leads to a fixed angle of projection. The result is that the system transfer matrix has a null-space and is not fully invertible. This yields two related problems, first, that we desire more outputs than we have inputs for (the result is that the problem is

underdetermined), and second, that because of the fixed angle of projection, we have a cone of missing information in the spatial-spectral Fourier domain corresponding to the null-space of the transfer matrix.

*1.7.1 Underdetermined Problem.*   Given either CTHIS design discussed previously, both spatial and spectral information are collected simultaneously. Because of the simultaneous collection, it is not possible to directly design the sensor to decouple the spatial and spectral resolutions. Because of this, changing the design to increase resolution in one domain (say spatial) affects the resolution in the other domain. Also, because of the fixed angle of the object with the imager, some of spatial frequencies of the original object are never sampled. The transfer matrix for this case therefore cannot be directly inverted. The pseudo-inverse of this matrix (as observed in section 1.6.2), will provide a good first step to an estimation problem, but is almost unusable as a complete object estimate.

*1.7.2 Cone of Missing Information.*   As mentioned earlier, a CTHIS image in the FPA can be considered as a projection of the 3D data cube into the 2D CTHIS image plane. Figure 1.15 (b) shows the data cube projected onto the CTHIS image plane. The angle of the projection is determined by the angular deviation from the dispersion element for the wavelength of interest. According to [2] "the 2D (Fourier) transform of a 2D projection yields one plane through the 3D transform of the original object", in this case, the original object is the hyperspectral data cube. Each of these planes pass through the origin and the angle of the Fourier plane slice is orthogonal to the direction of the corresponding Fourier axis of the projection from the data cube onto the 2D CTHIS image. This indicates that we can reconstruct the 3D Fourier data cube simply by taking the Fourier transform of a continuum of 2D projections (see figure 1.17). We can then recover the hyperspectral data cube simply by taking the inverse 3D Fourier transform. According to [7] "Recovery of a 3D distribution from 2D projections is known as the x-ray transform." Also according to [7], the x-ray transform has 4 assumptions: the imager is continuous, there are no diffraction

26

effects or aberrations (aberration free geometric optics), the data is not corrupted by noise (perfect detector), and that the projections can be obtained at any azimuth and projection angles. All of these assumptions are violated by a CTHIS, especially in the presence of atmosphere.

If a projection of the data cube could be taken at any azimuth and projection angles, we could choose a projection angle perpendicular to the wavelength axis. Then the Fourier plane slices are perpendicular to the spatial frequency axes and then we can simply sweep through 180 degrees to fully reconstruct the 3D Fourier cube. Unfortunately, we cannot do this for two reasons, first the projections are taken at discrete azimuth angles (finite number) which yields a discrete covering set spanning the 3D Fourier space, and second we cannot take a 90 degree projection to the wavelength axis. The finite number of angles can be overcome by accepting a discrete reconstruction (which we have already accepted from any hyperspectral data cube), in other words, making the object cube discrete. The non-orthogonal projection angle, on the other hand will yield a "cone of missing information" in the Fourier plane.

This cone means that a truly unique reconstruction is not possible from the measurements alone, however a-priori (object or transform) domain specific constraints can be used to fill in the missing cone. The missing cone by itself shows that object features which have higher spatial-frequency have more spectral frequency content represented in the data [7, 20]. The problem of reconstructing the cone of missing information is equivalent to the limited-angle computed-tomography problem [7]. Due to the cone of missing information and the fact that spatial and spectral information is correlated, there is ambiguity in determining the resolution of these sensors. To date no study of CTHIS resolution has been performed.

## 1.8  Literature Study Conclusions

This section detailed the current research into imaging spectrometers based on computed tomography. Various designs of other hyperspectral imaging sensor designs

27

were discussed as well as some of the advantages and disadvantages of each. CTHIS was discussed starting with early work in the field to current designs using diffractive elements, prisms and chromatic aberration of a lens for providing spectral diversity. These were examined with advantages and disadvantages from each one. From there, various reconstruction algorithms were discussed. Finally, the problem of missing information from the data was discussed as this problem affects every CTHIS sensor. The main advantage of CTHIS over other sensors is that they more fully utilize the light coming in from a scene versus diffractive imaging spectrometers or FTIS. They also have the ability to be configured to image flash events (unlike a diffractive sensor), and are not as sensitive to vibration due to their simple design (unlike a FTIS). While they have some significant advantages, CTHIS sensors have an ambiguity due to the general nature of the sensor setups with the cone of missing information, and this leads to ambiguity of the resolution of the CTHIS information. Specifically the spectral resolution has not been studied in the presence of noise. Also, very little has been done to make the CTHIS sensor available outside the laboratory environment with only one author actually referencing data taken outside. No discussion is present in the literature of using a CTHIS in the presence of atmospheric turbulence which would be necessary for the use of CTHIS in real-world applications. Techniques for evaluating the limiting factors of the CTHIS spectral resolution and solutions for determining the spectral resolution will be discussed in the following chapters.

# II. Theoretical Lower Bound on Resolution of CTHIS in the Presence of Noise

This chapter develops the theoretical lower bound on the spatial and spectral resolution of an unbiased object estimator for a lens-based CTHIS. First, the variance obtained by the CRLB is related to the Rayleigh resolution criteria in section 2.1. Next, a description of the Cramer-Rao Inequality is developed in 2.2. Third, an image model is developed from a simple object model. Finally, the lower bound on estimator performance for a simple object is given in section 2.4.

## 2.1 Relationship of Estimator Uncertainty to the Rayleigh Criteria

The Cramer Rao Lower Bound (also called the CRLB) gives us a lower bound on the variance of an estimator. However, we wish to determine the resolution of our system. The Airy disc is the PSF from a circular aperture. Using a standard resolution criteria such as a Rayleigh criteria [11], two point sources are considered resolved when they are separated so that the peak of an Airy disc from one point source is in the null the Airy disc of another point source next to it. The Airy disc is the PSF from a circular aperture which has a peak in the center, and concentric rings of reduced intensity with null rings in between. In the case of a circular aperture, Figure 2.1 shows an example of two points barely resolvable with the Rayleigh criteria. However we seek to apply the CRLB in an attempt to capture the effects of noise on resolution. Specifically when the actual point separation is equal to twice the standard deviation of the estimate of the separation, we can say that we are statistically resolved according to the Rayleigh criteria of separation because a single standard deviation represents the uncertainty of points in either spatial or spectral dimensions. So the resolution criteria can be stated as:

$$\frac{\Delta}{2\sigma_\Delta} = 1 \tag{2.1}$$
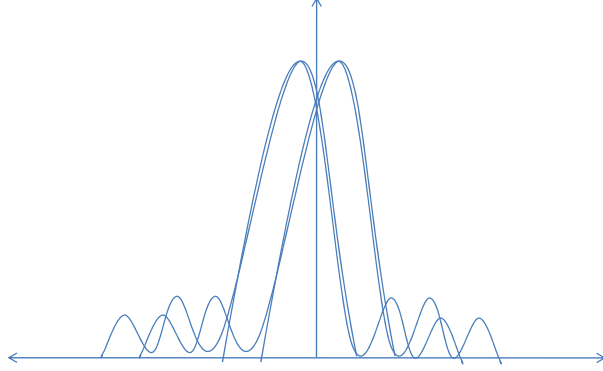
Figure 2.1:    Two points resolved according to the Rayleigh criteria

where $\Delta$ is the separation of the two points in question, and $\sigma_\Delta$ is the lower bound on the standard deviation of the estimate of $\Delta$ according to the CRLB.

## 2.2  *Cramer-Rao Lower Bound and Fisher Information of an Image with Poisson Noise*

The Cramer-Rao inequality states that the variance of an unbiased estimator of a parameter is no smaller than the inverse of the Fisher Information of the parameter estimated [32]. This provides a lower-bound on the variance of an estimator, commonly called CRLB. Specifically:

$$\sigma_\phi^2 \geq F_\phi^{-1} = -E\left[\frac{\partial^2 L}{\partial \phi^2}\right]^{-1} \tag{2.2}$$

where $\sigma_\phi^2$ is the variance of the estimated parameter $\phi$. Also, $L_k$ is the natural logarithm of the conditional Probability Density Function (PDF) of the data with

respect to the estimated variable:

$$L_k = \ln P(d_k|\phi) \tag{2.3}$$

where $P(d_k|\phi)$ is the probability mass function of the data $d_k$ given the parameter $\phi$. If more than one parameter is being estimated, then the joint probability is used, and the Fisher Information becomes a matrix. For multiple parameters estimation, we refer to them as $\phi_i$ and $\phi_j$ where $i$ and $j$ where the parameters are the same only when $i = j$. The log-likelihood over all data collected is given by $L$. Each element of the matrix is calculated from the second partial derivative of the log-likelihood function with respect to the parameters being estimated.

$$F_{ij} = -E\left[\frac{\partial^2 L}{\partial \phi_i \partial \phi_j}\right] \tag{2.4}$$

The CRLB for each parameter is the main diagonal of the inverse of the Fisher information matrix $(i = j)$.

$$\sigma^2_{\phi_i \phi_j} \geq F_{ij}^{-1} \tag{2.5}$$

The Probability Mass Function (PMF) of a collection of two dimensional images with Poisson noise is given by:

$$P(d|o_1, o_2, \Delta x, \Delta \lambda) = \prod_y \prod_x \prod_k i_k(x,y)^{d_k(x,y)} e^{-i_k(x,y)} (d_k(x,y)!)^{-1} \tag{2.6}$$

where the $d_k$ indicates a single frame in a series of images. The intensities of two points are $o_1$ and $o_2$. This equation assumes that the location of the first point is known Only two points are used because this will yield the simplest object to study both spatial and spectral resolution. More complex objects and features could be estimated, however the CRLB requires a specific object, therefore the simplest object is chosen for this resolution study. The two points are separated by $(\Delta_x, \Delta_\lambda)$. The location of the first point is assumed known and is set at the origin for convenience.

A simple object is given by

$$o(u, v, \lambda) = o_1 \delta(\lambda - \lambda_0) \delta(u - x_0, v - y_0) + o_2 \delta(\lambda - (\lambda_0 + \Delta \lambda)) \delta(u - (x_0 + \Delta_x), v - y_0) \quad (2.7)$$

With this simple object, the resolution of imaging systems can be determined by moving one point with respect to the other, and using the resulting image to compute the CRLB. The image equation is given by:

$$i_k(x, y) = \sum_{\lambda} o_1 h_k(x, y, \lambda) + o_2 h_k(x - \Delta_x, y - \Delta_y, \lambda + \Delta_\lambda) \quad (2.8)$$

where $h_k(x, y, \lambda)$ is the point spread function of our imaging system. As mentioned in section 2.1, these parameters are related to the resolution of two points using the standard deviation as a measure of the ability to resolve two points. This relationship allows a determination of resolution based on the CRLB and gives a parameter that can be used to predict how many images will be required to achieve a particular resolution. The log-likelihood function then becomes:

$$L = lnP(d|o_1, o_2, \Delta x, \Delta \lambda) = \sum_{y} \sum_{x} \sum_{k} d_k(x, y) ln[i_k(x, y)] - i_k(x, y) - ln[d_k(x, y)!] \quad (2.9)$$

We wish to find the lower bound for the variance of a parameter estimated from the data $d_k$. The parameters of interest will be discussed in the next section, however we can greatly simplify the CRLB for the Poisson PMF with generic parameters. Computing the first partial derivative with respect to a generic parameter of interest:

$$\frac{\partial L}{\partial \phi_i} = \sum_{y} \sum_{x} \sum_{d} \left( d_k(x, y) \frac{1}{i_k(x, y)} \frac{\partial i_k(x, y)}{\partial \phi_i} - \frac{\partial i_k(x, y)}{\partial \phi_i} \right) \quad (2.10)$$

where $\phi_i$ is the parameter of interest. Because we are interested in more than a single parameter, the second partial derivative needs to be taken. The second partial

derivative of a different parameter $\phi_j$ is:

$$\frac{\partial L}{\partial \phi_i \partial \phi_j} = \sum_y \sum_x \sum_d d_k(x,y) \frac{1}{i_k(x,y)^2} \left( \frac{\partial i_k(x,y)}{\partial \phi_i \partial \phi_j} i_k(x,y) - \frac{\partial i_k(x,y)}{\partial \phi_i} \frac{\partial i_k(x,y)}{\partial \phi_j} \right) - \frac{\partial^2 i_k(x,y)}{\partial \phi_i \partial \phi_j}$$

(2.11)

Then we take the expected value to get the Fisher information matrix, keeping in mind that the expected value is:

$$E\left[d_k(x,y)\right] = i_k(x,y)$$

(2.12)

that is, the expected value of the noisy data $d_k(x,y)$ is the image $i_k(x,y)$. Using this, the second derivative:

$$-E\left[\frac{\partial L}{\partial \phi_i \partial \phi_j}\right] = \sum_y \sum_x \sum_d -E[d_k(x,y)] \frac{1}{i_k(x,y)^2} \left( \frac{\partial^2 i_k(x,y)}{\partial \phi_i \partial \phi_j} i_k(x,y) - \frac{\partial i_k(x,y)}{\partial \phi_i} \frac{\partial i_k(x,y)}{\partial \phi_j} \right) - \frac{\partial^2 i_k(x,y)}{\partial \phi_i \partial \phi_j}$$

(2.13)

becomes greatly simplified:

$$-E\left[\frac{\partial L}{\partial \phi_i \partial \phi_j}\right] = \sum_y \sum_x \sum_d -\frac{i_k(x,y)}{i_k(x,y)^2} \left( \frac{\partial^2 i_k(x,y)}{\partial \phi_i \partial \phi_j} i_k(x,y) - \frac{\partial i_k(x,y)}{\partial \phi_i} \frac{\partial i_k(x,y)}{\partial \phi_j} \right) - \frac{\partial^2 i_k(x,y)}{\partial \phi_i \partial \phi_j}$$

(2.14)

And after cancelling all the extra terms, the final form of the Fisher information matrix elements are given by:

$$F_{ij} = \sum_y \sum_x \sum_k \frac{1}{i_k(x,y)} \frac{\partial i_k(x,y)}{\partial \phi_i} \frac{\partial i_k(x,y)}{\partial \phi_j}$$

(2.15)

meaning that we only need to compute the first derivatives of any parameter of interest and use the cross products to compute the Fisher information matrix elements.

## 2.3  Image model

As mentioned above, we wish to find a bound on the spatial and spectral resolution of our CTHIS system. One method is to compute the estimator variance for a scene with a known spectral and spatial separation $(\Delta_\lambda, \Delta_x)$, and compare the standard deviation to the actual separation. The scene consists of two point sources separated by a shift of $(\Delta_\lambda, \Delta_x)$ in space and wavelength respectively. The separation for spatial dimension is only a single dimension used for simplicity (figure 2.2). An
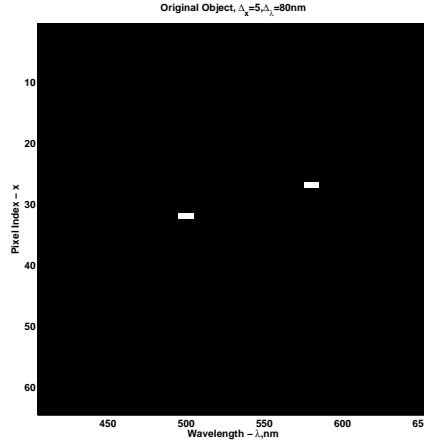


Figure 2.2:     Example Object

image of a simple object with two point sources at $(x_0, y_0, \lambda_0)$ with a shift of $(\Delta_x, \Delta_\lambda)$ between them, with an arbitrary point spread function (PSF) is modelled by:

$$
\begin{aligned}
i_k(x, y) = \sum_\lambda \sum_{u,v} [ & o_1 \delta(\lambda - \lambda_0) \delta(u - x_0, v - y_0) \\
& + o_2 \delta(\lambda - (\lambda_0 + \Delta\lambda)) \delta(u - (x_0 + \Delta_x), v - y_0)] \\
& \times h_k(u - x, v - y, \lambda) + \beta
\end{aligned}
\tag{2.16}
$$

where k is an index to a particular image or PSF in a set. The variable $\beta$ is a background that is not affected by the PSF, and is discussed later. Assuming a spatially shift-invariant PSF and the using sifting property of the dirac-delta function,

the image becomes:

$$i_k(x, y) = \sum_\lambda o_1 \delta(\lambda - \lambda_0) h_k(x - x_0, y - y_0, \lambda) \cdot$$

$$+ o_2 \delta(\lambda - (\lambda_0 - \Delta_\lambda)) \times h_k(x - (x_0 + \Delta_x), y - y_0, \lambda) d\lambda + \beta \quad (2.17)$$

noting that the Dirac delta for the spatial dimension of the point source fixes the PSF at its location. Finally defining the central wavelength $\lambda_0$ and integrating over all wavelengths applies the sifting property of the Dirac delta yielding:

$$i_k(x, y) = o_1 h_k(x - x_0, y - y_0, \lambda_0) + o_2 h_k(x - (x_0 + \Delta_x), y - y_0, \lambda_0 + \Delta_\lambda) + \beta. \quad (2.18)$$

Given the equations developed above for the CRLB (equation (2.15)), we can use our image model developed in this section to derive a more specific form of the CRLB for our simple test object. We are interested in our ability to estimate the intensities ($o_1$ and $o_2$) and the relative position ($\Delta_x, \Delta_\lambda$) of the two point sources in the scene. These are the specific parameters of interest used for $\phi_i$ and $\phi_j$ in the previous section to compute the CRLB. Notice that the background $\beta$ is a constant with respect to the parameters of interest, and drops out after taking the derivative. It will only affect the divisor from equation (2.15).

$$\frac{\partial i_k(x, y)}{\partial o_1} = h_k(x - x_0, y - y_0, \lambda_0) \quad (2.19)$$

$$\frac{\partial i_k(x, y)}{\partial o_2} = h_k(x - (x_0 + \Delta_x), y - y_0, \lambda_0 + \Delta_\lambda) \quad (2.20)$$

Note that the intensity partial derivatives are simply the fixed point spread functions which can be computed directly. However, for the other parameters ($\Delta_x, \Delta_\lambda$)

$$\frac{\partial i_k(x, y)}{\partial \Delta_x} = o_2 \frac{\partial}{\partial \Delta_x} h_k(x - (x_0 + \Delta_x), y - y_0, \lambda_0 + \Delta_\lambda) \quad (2.21)$$

$$\frac{\partial i_k(x, y)}{\partial \Delta_\lambda} = o_2 \frac{\partial}{\partial \Delta_\lambda} h_k(x - (x_0 + \Delta_x), y - y_0, \lambda_0 + \Delta_\lambda) \quad (2.22)$$

35

more simplification will be needed.

## 2.4 Theoretical Lower Bound on Spectral Resolution of a Defocused Image with Poisson Noise

We need to determine the PSF to further simplify equations (2.19)-(2.22) in order to compute the CRLB. The intensity point spread function ($h_k(x, y, \lambda)$ in equations (2.21) and (2.22)) of a given optical system can be computed by the amplitude point spread function $h_k^a(x, y, \lambda)$. The amplitude point spread function is the field resulting from a plane wave propagating through the optical system, corresponding to a point source (impulse) at infinity (equivalent to the impulse response discussed in classical linear systems):

$$h_k(x, y, \lambda) = \frac{|h_k^a(x, \lambda)|^2}{\left| \int_{x,y} h_k^a(x, y, \lambda) \right|^2} \tag{2.23}$$

Because this is a shift invariant amplitude PSF, the denominator will later be shown to be simply a scaling constant which does not vary with respect to $x$ or $\lambda$.

In the case of a defocused lens with a square aperture of side $2w$ and a defocus in meters of $W_d$, ignoring scaling constants and pure phase factors, the amplitude point spread function (impulse response) is computed by [11]:

$$h_k^a(x, y, \lambda) = \iint\limits_{-\infty}^{\infty} rect(2w\xi) rect(2w\zeta) \exp\left[ \frac{-2\pi j}{\lambda} \left( \frac{W_d(\xi^2 + \zeta^2)}{w^2} + \frac{x\xi + y\zeta}{z_d} \right) \right] d\xi d\zeta \tag{2.24}$$

where $(\xi, \zeta)$ are the spatial coordinates corresponding to the field in the lens plane, and $z_d$ is the distance between the lens and the focal plane for frame number $k$. $W_d$ is given by:

$$W_d = -\frac{w^2}{2} \left( \frac{1}{z_d} - \frac{1}{z_i} \right) \tag{2.25}$$

where $z_i$ is the distance from the lens to the image forming plane (where an image would be in focus). The variable $z_i$ depends on focal length which is dependent on

the index of refraction (and thereby wavelength). The actual focal length can be calculated from material properties, however for the sake of this analysis, the change in focal length due to a change in wavelength is assumed to be directly proportional to a parameter $\alpha$, with a possible bias term ($\beta_{fl}$ a minimal focal length) therefore:

$$f(\lambda) \approx \alpha\lambda + \beta_{fl} \tag{2.26}$$

and because we are considering a point source at infinity (a plane wave field propagation through the lens), $z_i$ becomes:

$$z_i(\lambda) = f(\lambda) \tag{2.27}$$

Therefore, $W_d$ becomes:

$$W_d = -\frac{w^2}{2}\left(\frac{1}{z_a} - \frac{1}{\alpha\lambda + \beta_{fl}}\right) \tag{2.28}$$

Substituting equation (2.28) into (2.24) we get:

$$h_k^a(x, y, \lambda, d) = \iint_{-w}^{w} \exp\left[\frac{\pi j}{\lambda}\left(\frac{(\xi^2 + \zeta^2)}{z_d} - \frac{(\xi^2 + \zeta^2)}{\alpha\lambda + \beta_{fl}} - \frac{2(x\xi + y\zeta)}{z_d}\right)\right] d\xi d\zeta \tag{2.29}$$

Where the limits are based on the size of the aperture. Note that this can be extended to a generic aperture function:

$$h_k^a(x, y, \lambda, d) = \iint_{-\infty}^{\infty} A(\xi, \zeta)\exp\left[\frac{\pi j}{\lambda}\left(\frac{(\xi^2 + \zeta^2)}{z_d} - \frac{(\xi^2 + \zeta^2)}{\alpha\lambda + \beta_{fl}} - \frac{2(x\xi + y\zeta)}{z_d}\right)\right] d\xi d\zeta \tag{2.30}$$

We extend this to a generic aperture function so that the limits of our equation extend from $-\infty$ to $\infty$ and correspond to a Fourier transform.

Because we are also estimating the intensities of the point source, we also compute the Fisher information matrix with respect to the parameters $o_1$ and $o_2$, which are measured in photons. Because the intensities in number of photons are much

37

higher quantities than the pixel size and the wavelength (typically measured in micrometers), the Fisher information matrix quickly becomes singular as the number of images $k$ increases. In order to avoid this, we make the parameters a discrete step size and take derivatives with respect to the number of steps. We also scale our aperture variable to keep constant sampling in the focal plane. We define $L_d$ as the size of the aperture, and keep the ratio $\frac{z_d}{L_d}$ fixed. Keeping this ratio fixed scales the sampling to a constant focal plane array pixel size yielding a more accurate model of the focal plane. So:

$$
\begin{aligned}
dx &= \frac{\lambda z_d}{L_d} & dy &= \frac{\lambda z_d}{L_d} \\
\Delta_\xi &= \frac{L_d}{N} & \Delta_\zeta &= \frac{L_d}{N} \\
x &= k\, dx & y &= p\, dx \\
\xi &= m\Delta_\xi & \zeta &= n\Delta_\xi
\end{aligned}
\tag{2.31}
$$

where $N$ is the number of points in the focal plane. We assume square pixels, and square sampling of the aperture plane, where $dx$ is the pixel size in the focal plane, and $\Delta_\xi$ is the sampling in the aperture plane. Now to compute the normalized Point Spread Function, we substitute equations (2.30) and (2.31) into (2.23), and replace the integrals with summations.

$$
h_k(k,p,\lambda) = \frac{\Delta_\xi^4 \left| \sum\limits_{m,n} A(m,n) \exp\left[\frac{\pi j(m^2+n^2)}{\lambda}\left(\frac{\lambda^2 z_d}{N^2 dx^2} - \frac{\lambda^2 z_d^2}{(\alpha\lambda+\beta_{fl})N^2 dx^2}\right)\right] \exp\left[\frac{-2\pi j(km+np)}{N}\right] \right|^2}{\Delta_\xi^4 \left| \sum\limits_{m,n} A(m,n) \exp\left[\frac{\pi j(m^2+n^2)}{\lambda}\left(\frac{\lambda^2 z_d}{N^2 dx^2} - \frac{\lambda^2 z_d^2}{(\alpha\lambda+\beta_{fl})N^2 dx^2}\right)\right] \sum\limits_{x,y} \exp\left[\frac{-2\pi j(km+np)}{N}\right] \right|^2}
\tag{2.32}
$$

As seen in equation (2.15), the Fisher information matrix elements are computed by the first derivatives of the image with respect to the variables under consideration. Specifically we are interested in the $\Delta x$ and $\Delta\lambda$ paramaters. Using a discrete change of variable for $\Delta_x$ and $\Delta_\lambda$. The variables $\Delta'_x$ and $\Delta'_\lambda$ signify a step size in meters (for simplicity, we fix $\Delta'_x$ as the size of 1 pixel), and $P_x$ and $P_\lambda$ signify the number of steps

in discrete space:

$$\Delta_x = \Delta'_x P_x = dx P_x$$

$$\Delta_\lambda = \Delta'_\lambda P_\lambda$$

(2.33)

So the the image equation (2.34) becomes:

$$i_k(k,p) = o_1 h_k(k,p,\lambda_0) + o_2 h_k(k - P_x, p, \lambda_0 + \Delta'_\lambda P_\lambda)$$

(2.34)

assuming $x_0 = 0$ and $y_0 = 0$ for the sake of notational simplicity. The derivatives are now taken with respect to $P_x$ and $P_\lambda$. This necessitates taking the derviatives of the PSF with respect to these variables. Utilizing the product rule and an identity of the absolute value function, the derivative of the PSF with respect to $P_x$ becomes:

$$\frac{\partial}{\partial P_x} h_k(k - P_x, p, \lambda_0 + \Delta'_\lambda P_\lambda) = \frac{\partial}{\partial P_x} \kappa^{-1} h_k^a(k - P_x, p, \lambda_0 + \Delta'_\lambda P_\lambda)$$
$$\times h_k^{a*}(k - P_x, p, \lambda_0 + \Delta'_\lambda P_\lambda)$$
$$= 2\kappa^{-1} Real \left[ \frac{\partial}{\partial P_x} h_k^a(k - P_x, p, \lambda_0 + \Delta'_\lambda P_\lambda) \right.$$
$$\left. \times h_k^{a*}(k - P_x, p, \lambda_0 + \Delta'_\lambda P_\lambda) \right]$$

(2.35)

leading to:

$$= 2\kappa^{-1} Real \left[ \sum_{m,n} A(m,n) \frac{2\pi j m}{N} \exp \left[ \frac{\pi j (m^2 + n^2)(\lambda_0 + \Delta'_\lambda P_\lambda) z_d^2}{N^2 dx^2} \right. \right.$$
$$\times \left( \frac{1}{z_d} - \frac{1}{(\alpha(\lambda_0 + \Delta'_\lambda P_\lambda) + \beta_{fl})} \right) \Bigg]$$
$$\exp \left[ \frac{-2\pi j (km + np)}{N} \right] \exp \left[ \frac{2\pi j m P_x}{N} \right]$$
$$\times \sum_{m,n} A(m,n)$$
$$\exp \left[ \frac{\pi j (m^2 + n^2)(\lambda_0 + \Delta'_\lambda P_\lambda) z_d^2}{N^2 dx^2} \left( \frac{1}{z_d} - \frac{1}{(\alpha(\lambda_0 + \Delta'_\lambda P_\lambda) + \beta_{fl})} \right) \right]$$
$$\exp \left[ \frac{-2\pi j (km + np)}{N} \right] \exp \left[ \frac{2\pi j m P_x}{N} \right] \Bigg]$$

(2.36)

where $\kappa$ is a scaling constant normalizing the area under the PSF to unity and is the same as the denominator in (2.23). The derivative of the PSF with respect to $P_\lambda$ is given by:

$$
\begin{aligned}
\frac{\partial}{\partial P_\lambda} h_k^a(k - P_x, p, \lambda_0 + \Delta_\lambda' P_\lambda) =& \frac{\partial}{\partial P_\lambda} \kappa^{-1} h_k^a(k - P_x, p, \lambda_0 + \Delta_\lambda' P_\lambda) \\
& \times h_k^{a*}(k - P_x, p, \lambda_0 + \Delta_\lambda' P_\lambda) \\
=& 2\kappa^{-1} Real\left[ \frac{\partial}{\partial P_\lambda} h_k^a(k - P_x, p, \lambda_0 + \Delta_\lambda' P_\lambda) \right. \\
& \left. \times h_k^{a*}(k - P_x, p, \lambda_0 + \Delta_\lambda' P_\lambda) \right]
\end{aligned}
\tag{2.37}
$$

yielding:

$$
\begin{aligned}
=& 2\kappa^{-1} Real\left[ \sum_{m,n} A(m,n) \left[ \frac{\pi j (m^2 + n^2)\Delta_\lambda' z_d^2}{N^2 dx^2} \right. \right. \\
& \left( \frac{1}{z_d} - \frac{1}{(\alpha(\lambda_0 + \Delta_\lambda' P_\lambda) + \beta_{fl})} \right) \\
& \left. + \frac{\pi j (m^2 + n^2)(\lambda_0 + \Delta_\lambda' P_\lambda) z_d^2}{N^2 dx^2} \frac{\alpha\Delta_\lambda'}{(\alpha(\lambda_0 + \Delta_\lambda' P_\lambda) + \beta_{fl})^2} \right] \\
& \exp\left[ \frac{\pi j (m^2 + n^2)(\lambda_0 + \Delta_\lambda' P_\lambda) z_d^2}{N^2 dx^2} \right. \\
& \left. \times \left( \frac{1}{z_d} - \frac{1}{(\alpha(\lambda_0 + \Delta_\lambda' P_\lambda) + \beta_{fl})} \right) \right] \\
& \times \exp\left[ \frac{-2\pi j(km + np)}{N} \right] \exp\left[ \frac{2\pi jmP_x}{N} \right] \\
& \times \sum_{m,n} A(m,n) \exp\left[ \frac{\pi j (m^2 + n^2)(\lambda_0 + \Delta_\lambda' P_\lambda) z_d^2}{N^2 dx^2} \right. \\
& \left. \left( \frac{1}{z_d} - \frac{1}{(\alpha(\lambda_0 + \Delta_\lambda' P_\lambda) + \beta_{fl})} \right) \right] \\
& \left. \exp\left[ \frac{-2\pi j(km + np)}{N} \right] \exp\left[ \frac{2\pi jmP_x}{N} \right] \right]
\end{aligned}
\tag{2.38}
$$

It should be noted that the discrete summations in equations (2.32), (2.38) and (2.36) can all be computed by using a Discrete Fourier Transform (DFT), and as such, the DFT is conveniently used to compute these functions.

# III. Data simulation and reconstruction

This chapter discusses the development of a projection-based Expectation Maximization (EM) Estimator based on Poisson noise in section 3.1, followed by a discussion of the simulation setup in section 3.2.

## 3.1 Projection Based Reconstructor

In this section, a reconstructor to estimate the object from a series of images is developed. This reconstructor is the basis for the simulation and the laboratory experiment results shown in section 5.4.2. The lens-based chromotomagraphic hyperspectral sensor takes a series of images each having a known defocus from the next image in the series. Given the collected image data, the originating scene is unknown so an estimator the must be used. A well known technique, known as maximum-likelihood estimation (MLE) is to maximize the conditional probability over all values of a parameter to be estimated. In this case, the unknown parameter is the scene and the data is the image produced by our known transfer function [32].

The reconstructor is further simplified to a projection based reconstructor as we only intend to explore the spatial separation in one dimension, as well as spectral separation. The data is modeled as:

$$d_k(x, y) = i_k(x, y) + n_k(x, y) \tag{3.1}$$

and is a random variable with a Poisson probability mass function given by $P_D(d)$:

$$P_D(d) = \prod_y \prod_x \prod_k i_k(x, y)^{d_k(x,y)} e^{-i_k(x,y)} (d_k(x, y)!)^{-1} \tag{3.2}$$

where $i_k(x, y)$ is the expected value of the data $d_k(x, y)$ for frame number $k$ with the 2 dimensional location $(x, y)$, this assumes that each pixel is statistically independent from the others. The value $i_k(x, y)$ is also the image formed by the unknown object

at plane $k$. Specifically, the image is given by:

$$i_k(x,y) = \sum_{\lambda}\sum_{u}\sum_{v} \gamma_{\lambda}o(u,v,\lambda)h_k(u-x,v-y,\lambda) \qquad (3.3)$$

where $\gamma_{\lambda}$ is the spectral weighting paramater for the number of photons, $o(u,v,\lambda)$ is object at spatial coordinates $(u,v)$ in the object plane and wavelength $\lambda$, and $h_k(x,y,\lambda)$ is the point spread function at frame number $k$. The spectral weighting parameter $\gamma_{\lambda}$ is given so that initially $\sum_{u}\sum_{v} o(u,v,\lambda) = 1$ that is the object is unity for each wavelength. The MLE is developed by maximizing the conditional probability given an image $i_k(x,y)$ using an object estimate $\hat{o}(x,y,\lambda)$ and a spectral weighting estimate.

Because the natural logarithm is an increasing function, the computation of the probability mass function can be greatly simplified by applying the natural logarithm and maximizing it instead:

$$L_D(d) = ln[P_D(d)] = \sum_{y}\sum_{x}\sum_{k} d_k(x,y)ln[i_k(x,y)] - i_k(x,y) - ln[d_k(x,y)!] \quad (3.4)$$

the logarithm of the factorial term in this equation does not contribute to the maximization and is ignored in further development. This likelihood function is recast in terms of the estimated parameters.

A different method of computing the object was proposed in [12] where a projection operation produced a single spatial dimension and a spectral dimension. This method features a significantly lower computation cost. The image is related to a one-dimensional image projection $i_k(x)$ by the equation:

$$i_k(x) = \sum_{y}\sum_{\lambda}\sum_{u}\sum_{v} \gamma_{\lambda}o(u,v,\lambda)h_k(x-u,y-v,\lambda) \qquad (3.5)$$
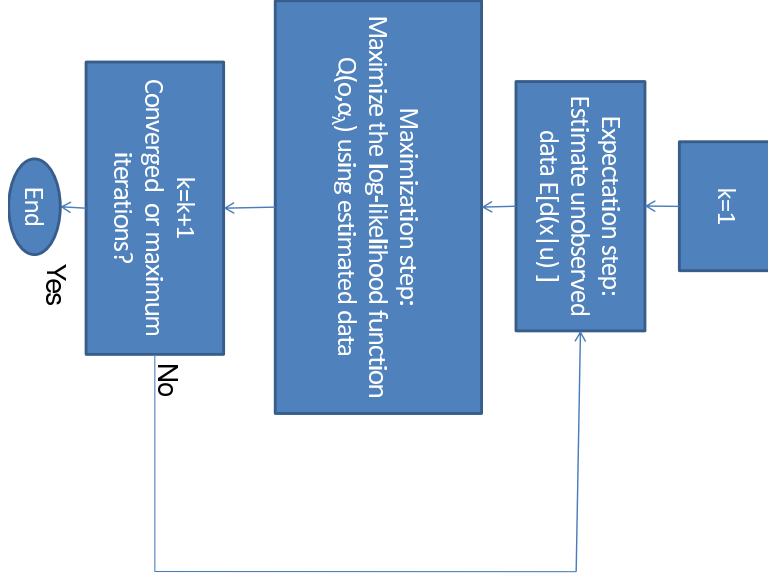
Figure 3.1:    Description of the EM algorithm

by using the projection of the object and PSF:

$$i_k(x) = \sum_{\lambda} \sum_{u} \gamma_{\lambda} \acute{o}(u, \lambda) \acute{h_k}(x - u, \lambda) \tag{3.6}$$

where $\acute{h_k}(x, \lambda) = \sum_y h_k(x, y, \lambda)$ and $\acute{o}(u, \lambda) = \sum_v o(u, v, \lambda)$. Using these projections significantly reduces computation time, but still allows the study of the effect of the number of defocus frames on spatial and spectral resolution.

The next step in estimating the scene is to maximize the log-likelihood which we call $Q(o, \gamma_{\lambda})$ restated in terms of our estimated variables with respect to an object estimate $\hat{o}(u, \lambda)$ and spectral weighting estimate $\hat{\gamma_{\lambda}}$. This could be done in multiple ways, however a well known method is the Expectation Maximization (EM) algorithm [6]. In order to use the EM algorithm, we first surmise the existence of an a set of unknown variables. We also surmise that there exists a mapping, in this case a many-to-one mapping, between the set of unknown variables and the measured data. The EM algorithm then maximizes the PMF of the unknown variables conditioned on the measured data using the conditional expected value derived from the assumed mapping. Figure 3.1 gives a flowchart for the EM algorithm. Stated simply, we seek

an object $\hat{o}(u, \lambda)$ and spectral energy parameter $\hat{\gamma}_\lambda$ with $Q(\hat{o}^{old}, \hat{\gamma}_\lambda{}^{old})$ such that:

$$Q(\hat{o}^{new}, \hat{\gamma}_\lambda{}^{new}) \geq Q(\hat{o}^{old}, \hat{\gamma}_\lambda{}^{old}) \tag{3.7}$$

where $\hat{o}^{new}$ and $\hat{\gamma}_\lambda{}^{new}$ are iterative updates to our previous (old) object and spectral energy estimates respectively. We begin by modelling the measured (incomplete) data $d_k(x)$ as a sum of the unknown random variables $d_k(x) = \sum_u d_k(x|u)$, where the collection of unknown variables $d_k(x|u)$ is called the complete data. In creating the complete data, each variable $d_k(x|u)$ is assumed to be independent for each unique value of $u$ and Poisson distributed. The complete data only needs to be statistically consistent with our measurements [27] and may not have a physical meaning as is the case in our problem statement. The mean of the complete data is given by:

$$E[d_k(x|u)] = \gamma_\lambda o(u, \lambda) h_k(x - u, \lambda) \tag{3.8}$$

The complete data is then further related to the modelled data and image by:

$$E[d_k(x)] = \sum_u E[d_k(x|u)] = \sum_u \gamma_\lambda o(u, \lambda) h_k(x - u, \lambda) = i_k(x) \tag{3.9}$$

yielding an expression from which we can develop the complete data log-likelihood. The complete data log-likelihood is given by:

$$L(o, \gamma_\lambda) = \sum_k \sum_x \sum_u d_k(x|u) ln[\gamma_\lambda o(u, \lambda) h_k(x-u, \lambda)] - \sum_k \sum_x \sum_u \gamma_\lambda o(u, \lambda) h_k(x-u, \lambda) \tag{3.10}$$

The incomplete data log-likelihood is given by the expected value of the incomplete log-likelihood conditioned on the measured data $d_k(x)$:

$$
\begin{aligned}
Q(\hat{o}^{new}, \hat{\gamma_\lambda}^{new}) =& E\left[L(\hat{o}^{new}, \hat{\gamma_\lambda}^{new}) | d_k(x)\right] \\
=& \sum_k \sum_x \sum_u E^{old}[d_k(x|u) | d_k(x)] ln[\hat{\gamma_\lambda}^{new} \hat{o}^{new}(u, \lambda) h_k(x - u, \lambda)] \\
& - \sum_k \sum_u \sum_x \hat{\gamma_\lambda}^{new} \hat{o}^{new}(u, \lambda) h_k(x - u, \lambda)
\end{aligned}
$$

(3.11)

where the expected value is based on old estimates (designated by the operation $E^{old}[*]$) for the object ($\hat{o}^{old}$) and spectral energy coefficient ($\hat{\gamma_\lambda}^{old}$). We designate the object ($\hat{o}^{new}$) and spectral energy coefficient ($\hat{\gamma_\lambda}^{new}$) as iterative updates whose equations are derived later, the old values of which are previous estimates to the data. This portion of the process where we develop the conditional log-likelihood whose expected value is the log-likelihood of interest is called the expectation step of the EM algorithm. At this point, it is necessary to develop the expression for the expected value of a single Poisson variable conditioned on the sum of a number of independent Poisson variables, in this case, $d_k(x|u)$ conditioned on $d_k(x)$.

$$
E[d_k(x|u) | d_k(x)] \tag{3.12}
$$

In order to determine the expected value of a single Poisson variable conditioned on the sum, we start with the sum of 2 independent Poisson variables:

$$
d = d_1 + d_2 \tag{3.13}
$$

with the expected values:

$$
\begin{aligned}
E[d_1] &= i_1 \\
E[d_2] &= i_2
\end{aligned}
\tag{3.14}
$$

45

where $d_1$ is the Poisson random variable of interest given the conditional expectation of the poisson incomplete data $d_k(x)$. We wish to find the PMF of $d_1$ conditioned on the sum $d$. Using Bayes rule we get the following,

$$P_{(D_1|D)}(d_1|d) = \frac{P_{(D_1,D_2))}(d_1,d_2)}{P_D(d)} \tag{3.15}$$

that is, the joint density of $d_1$ and $d_2$ divided by the marginal density for the sum. Because $d_1$ and $d_2$ are independent, the joint density is given the product of their marginal Poisson mass functions:

$$P_{(D_1,D_2)}(d_1,d_2) = P_{D_1}(d_1)P_{D_2}(d_2) = \frac{i_1^{d_1} i_2^{d_2} e^{-(i_1+i_2)}}{d_1!d_2!} \tag{3.16}$$

and the marginal is given by:

$$P_D(d) = \frac{i^d e^{-i}}{d!} \tag{3.17}$$

Noting that the expected value of $d$ is the sum of the expected values of $d_1$ and $d_2$

$$i = E[d] = E[d_1] + E[d_2] = i_1 + i_2 \tag{3.18}$$

and also, that $d_2$ can be re-written as a difference between the sum and $d_1$

$$d_2 = d - d_1 \tag{3.19}$$

we can find the conditional expected value. Substituting (3.19) into (3.16) and (3.18) into equation (3.17), we can see that (3.15) becomes:

$$P_{(D_1|D)}(d_1|d) = \frac{d!}{d_1!(d-d_1)!} \frac{i_1^{d_1} i_2^{(d-d_1)}}{(i_1+i_2)^d} = \frac{d!}{d_1!(d-d_1))!} \frac{i_1^{d_1} i_2^{(d-d_1)}}{(i_1+i_2)^{d_1}(i_1+i_2)^d(i_1+i_2)^{-d_1}} \tag{3.20}$$

we can rearrange (3.20) into the following form.

$$P_{(D_1|D)}(d_1|d) = \frac{d!}{d_1!(d-d_1))!} \left(\frac{i_1}{(i_1+i_2)}\right)^{d_1} \left(\frac{i_2}{(i_1+i_2)}\right)^{(d-d_1)} \tag{3.21}$$

Noting that the two fractions sum to unity:

$$1 - \frac{i_1}{i_1 + i_2} = \frac{i_1 + i_2}{i_1 + i_2} - \frac{i_1}{i_1 + i_2} = \frac{i_2}{i_1 + i_2} \tag{3.22}$$

it becomes apparent that this conditional probability is in the form of a binomial distribution. A binomial distribution in general form is given by:

$$P_K(k) = \frac{n!}{k!(n-k)!} p^k (1-p)^{(n-k)} \tag{3.23}$$

where $k$ is the random variable out of $n$ independent experiments (called Bernoulli trials) with a probability of success $p$. The expected value of a binomial random variable is given by $np$. Letting $k = d_1$ as our random variable, with $n = d$ trials and also letting:

$$p = \frac{i_1}{i_1 + i_2} \tag{3.24}$$

the expected value of a single Poisson conditioned on the sum becomes the following

$$E[d_1|d] = d \frac{i_1}{i_1 + i_2}. \tag{3.25}$$

Substituting in $d_k(x)$ and $i_1 = E[d_k(y|x)]$ into 3.25 we get the following( [28]):

$$E[d_k(x|u)|d_k(x)] = d_k(x) \frac{\gamma_\lambda o(u, \lambda) h_k(x - u, \lambda)}{i_k(x)}. \tag{3.26}$$

It is also desirable to incorporate the effect of background noise in order to make the simulation more realistic. A flat Poisson background $b_k(x)$ with a constant mean ($E[b_k(x)] = c$) is incorporated by adding it to the previous data model $d_k(x, y)$ (equation (3.9)) and the incomplete data is relabeled $d_k^b(x)$ to signify the addition of a background $d_k^b(x, y) = d_k(x, y) + b_k(x, y)$. This background is similar to adding a flat field to the image. The background in this case is assumed to be known or measured separately and is not estimated in this algorithm. This model is effectively diffuse

background light and can also be considered similar to the effect of additive Gaussian noise if the diffuse light level is high enough.

Since we are only interested in the portion of the data dependant on the object, $b_k(x)$ can be considered another unknown variable added together with the complete data with a total expectation of:

$$E[d_k^b(x)] = i_k(x) + b_k(c) \tag{3.27}$$

However, because we measure the data in our experiment, the measured or known background is used instead of estimating the expected value and no further estimator for the background is developed. This means that the expected value in (3.26) is given by:

$$E^{old}[d_k(x|u)|d_k^b(x)] = d_k^b(x)\frac{\gamma_\lambda^{old}\hat{o}^{old}(u,\lambda)h_k(x-u,\lambda)}{i_k(x) + b_k(x)} \tag{3.28}$$

where $i_k(x)$ is the image formed at distance plane k by a current object estimate $\hat{o}^{old}$ and $b_k(x)$ is the background measured previously.

The next step is to maximize the complete data log-likelihood which is called the maximization step of the EM algorithm. To maximize the complete data log-likelihood, the derivatives of equation (3.11) are taken with respect to $\hat{o}^{new}$ and $\hat{\gamma}_\lambda^{new}$ giving equations (3.29) and (3.30).

$$\frac{\partial Q}{\partial \hat{o}^{new}(u,\lambda)} = \sum_k \sum_x \frac{E^{old}[d_k(x|u)|d_k(x)]}{\hat{o}^{new}(u,\lambda)} \\ - \sum_k \sum_x \hat{\gamma}_\lambda^{new} h_k(x,\lambda) \tag{3.29}$$

Where maxima exist, the first partial derivative will equal zero.

$$\frac{\partial Q}{\partial \gamma_\lambda^{new}} = \sum_k \sum_x \sum_u \frac{E^{old}[d_k(x|u)|d_k(x)]}{\gamma_\lambda^{new}} \\ - \sum_k \sum_x \sum_u \hat{o}^{new}(u,\lambda)h_k(x-u,\lambda) \tag{3.30}$$

48

We then set these equations equal to zero solve for $\hat{o}^{new}$ and $\gamma_\lambda^{new}$. We further make the assumptions:

$$\begin{aligned}
\sum_x h_k(x, \lambda) &= 1 \\
\sum_u \hat{o}^{new}(u, \lambda) &= 1
\end{aligned} \tag{3.31}$$

which can be controlled based on our initial guess for the object and by scaling the PSFs. The spectral energy parameter contains the energy in the series of data frames, and is assumed equal over all wavelengths to start with:

$$\gamma_\lambda^{old} = \frac{\sum_k \sum_x d_k(x)}{\epsilon} \tag{3.32}$$

where $\epsilon$ is the number of wavelengths of interest. Therefore the spectral energy is weighted equally across all wavelengths according to the total energy in the collection of frames. Also, we assume that for each iteration

$$\gamma_\lambda^{new} \approx \gamma_\lambda^{old} \tag{3.33}$$

meaning that we do not expect the estimate for $\gamma_\lambda$ to vary significantly with each iteration. Finally, we need to take the expected value of the incomplete data conditioned on the complete data with background given in equation (3.28). Substituting the expected value (3.26) into equations (3.29) and (3.30) gives:

$$\sum_k \sum_x \frac{d_k^b(x) \gamma_\lambda^{old} \hat{o}^{old}(u, \lambda) h_k(x - u, \lambda)}{(i_k(x) + b_k(x)) \hat{o}^{new}(u, \lambda)} - \hat{\gamma_\lambda}^{new} \sum_k \sum_x h_k(x, \lambda) = 0 \tag{3.34}$$

$$\sum_k \sum_x \sum_u \frac{d_k^b(x) \gamma_\lambda^{old} \hat{o}^{old}(u, \lambda) h_k(x - u, \lambda)}{(i_k(x) + b_k(x)) \gamma_\lambda^{new}} - \sum_k \sum_u \hat{o}^{new}(u, \lambda) \sum_x h_k(x - u, \lambda) = 0 \tag{3.35}$$

49

with the summations rearranged. The PSFs are shift invariant and because of our earlier assumption of $\sum_x h_k(x - u, \lambda) = 1$, we get:

$$\sum_k \sum_x \frac{d_k^b(x) \gamma_\lambda^{old} \hat{o}^{old}(u, \lambda) h_k(x - u, \lambda)}{(i_k(x) + b_k(x)) \hat{o}^{new}(u, \lambda)} - \hat{\gamma}_\lambda^{new} K = 0 \qquad (3.36)$$

$$\sum_k \sum_x \sum_u \frac{d_k^b(x) \gamma_\lambda^{old} \hat{o}^{old}(u, \lambda) h_k(x - u, \lambda)}{(i_k(x) + b_k(x)) \gamma_\lambda^{new}} - K = 0 \qquad (3.37)$$

where the value $K$ is the total number of frames. Solving the equations for our estimates, we get:

$$\hat{o}^{new}(u, \lambda) = K^{-1} \frac{\hat{\gamma}_\lambda^{old}}{\hat{\gamma}_\lambda^{new}} \hat{o}^{old}(u, \lambda) \sum_k \sum_x \frac{d_k^b(x)}{i_k(x) + b_k(x)} h_k(x, \lambda) \qquad (3.38)$$

$$\hat{\gamma}_\lambda^{new} = K^{-1} \sum_k \sum_x \frac{d_k^b(x)}{i_k(x) + b_k(x)} \sum_u \hat{\gamma}_\lambda^{old} \hat{o}^{old}(u, \lambda) h_k(x, \lambda) \qquad (3.39)$$

Finally we use the assumption in (3.33) to cancel the dependence on $\gamma_\lambda$ from equation (3.38) giving us the final form.

$$\hat{o}^{new}(u, \lambda) = K^{-1} \hat{o}^{old}(u, \lambda) \sum_k \sum_x \frac{d_k^b(x)}{i_k(x) + b_k(x)} h_k(x, \lambda) \qquad (3.40)$$

Equation (3.40) is very similar in form to the object expressed in [12], and the added spectral energy term (3.39) allows us to constrain total energy in the object estimate while allowing the energy in each wavelength to vary independently. This solution is similar in form to the equations in section 1.6, it differs on two key points. First, $\gamma_\lambda$ is allowed to range and is estimated jointly with the object. This helps to separate the spatial and the spectral dimensions of the estimate. Secondly, this algorithm also has an independent background which could allow this algorithm to perform better in the case of a large amount of diffuse clutter.

## 3.2 Simulation Setup

A simulation was performed using the parameters listed in table 3.1. Varying numbers of frames and spectral separations were used to accurately quantify the relationship between spectral resolution and the number of frame positions (also called defocus planes).

A simple experimental setup was modelled in simulation and set up in the laboratory for a single instance of the simulation. Figure 3.2 gives a notional schematic for the optical design of a lens-based CTHIS. The parameters for the simulation and experiment setup are given in table 3.1. Light-emitting diodes were simulated to approximate the object modelled in the CRLB mentioned in section 2.4.

The source object was modelled with a circular pattern at multiple wavelength spacings ($\Delta_\lambda$), and then convolved with the PSF (over multple wavelengths) corresponding to a lens with chromatic aberration.

The dispersion element and the two lenses closest to the camera were simulated as a single converging lens for this setup, and the dispersion is provided by the chromatic aberration of the converging lens. This chromatic aberration changes the focal length at which each wavelength gives the sharpest picture. The wavelength is modelled as in the CRLB section as a linear change given by:

$$f_\lambda = \alpha\lambda + f_{bias} \tag{3.41}$$

where $\alpha$ is the dispersion parameter measured from the lens and $\lambda$ is the wavelength. The $f_{bias}$ parameter is inherent to the lens and is dependent on both the radius of curvature and the index of refraction. Both $\alpha$ and $f_{bias}$ were measured in the lab, and used in simulation. Equation (3.42) gives the un-normalized PSF of the lens which is normalized to unit magnitude for the reconstruction algorithm (see previous section).

$$h_k(x,y,\lambda) = \left| \iint_{-w}^{w} \exp\left[ \frac{\pi j}{\lambda} \left( \frac{(u^2+v^2)}{z_d} - \frac{(u^2+v^2)}{\alpha\lambda+f_{bias}} - \frac{2(xu+yv)}{z_d} \right) \right] du dv \right|^2 \tag{3.42}$$

51
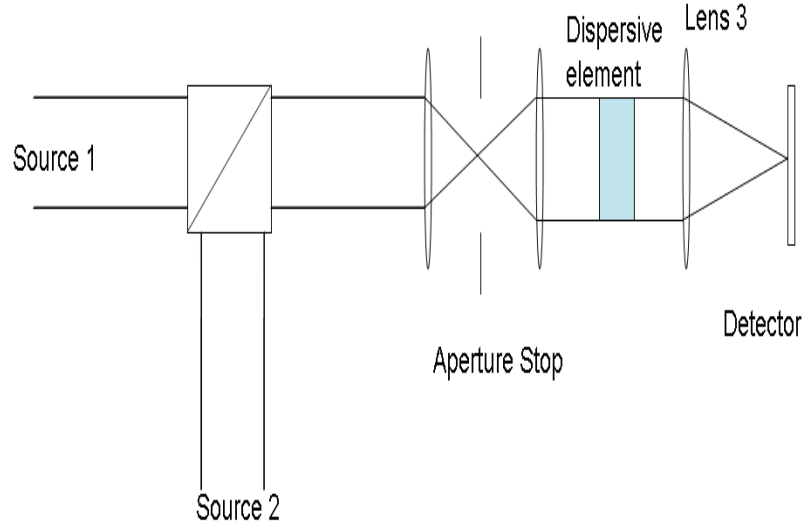
Figure 3.2:     Schematic of experiment set up with two sources

The distance $z_d$ represents the physical distance between the lens and the detector plane. Multiple distances for $z_d$ are used by moving the lens further away from to the detector plane from an inital starting point. The initial starting point is determined by the wavelengths of interest and the parameters of the lens. Specifically, the shortest distance to the focal plane should be closer than the focal length $f_\lambda$ of the shortest wavelength of interest. Similarly, the farthest $z_d$ from the focal plane should be farther away than the focal length of the longest wavelength of interest.

The number of defocus frames was varied giving various reconstructions of the object to determine the specific effect of on spectral resolution. A multiplier was used to vary the exposure time so that higher numbers of images did not result in larger numbers of photons thereby resulting in an automatically higher signal to noise ratio. The exposure time was varied corresponding to the number of frames used, with a longer exposure (more images added together) corresponding to fewer frames, and shorter exposure (fewer images added together) corresponding to more frames used.

Table 3.1:  Simulation and Experiment Parameters

| Parameter | Value | Units |
|---|---|---|
| $dx$ (Detector Pitch) | 16 | $\mu$m |
| $N$ (Detector size) | 512 | pixels |
| Aperture Diameter | 1 | cm |
| Number of wavelengths | 10 | |
| $\lambda_0$ (center wavelength) | 560 | nm |
| $\Delta\lambda$ (wavelength spacing simulation) | 10-100 | nm |
| Minimum-Maximum simulated wavelengths ($\lambda_{min} - \lambda_{max}$) | 560-645 | nm |
| $f_{\lambda_0}$ (Focal length @ $\lambda_0$) | 441.6 | mm |
| $\alpha$ ($\frac{\Delta_f}{\Delta\lambda}$ measured from lens) | 1.2406x10$^5$ | |
| $f_{bias}$ (minimum focal length) | 373.4 | mm |
| $K$ (Number of defocus planes) | 3-20 | |
| Minimum/Maximum Distance ($z_d$) | 420.4/469.2 | mm |
| $\Delta_{z_d}$ (Distance between each defocus plane) | 0.26 | mm |
| Number of iterations for reconstruction | 2000 | |
| Number of noisy realizations | 500 | |

This normalizes the energy (number of photons) used for each set of defocus frames so that taking more frames will not be better simply because of a longer exposure time. A constant background was then simulated and then a noisy realization was taken (using Poisson statistics). The simulated images and background were scaled according to the parameters of a realistic camera to convert the units to photons based on the photon transfer characteristics of the camera.

# IV.  Experimental Setup

This chapter discusses the experimental parameters in Section 4.1 and the reasons for design choices for the experiment. Then in Section 4.2 the calibration of sources using a double-slit experiment is discussed. Finally, modelling calibration of the lens and the comparison to the CRLB are discussed in Section 4.3.

## *4.1    Experimental Parameters*

The two sources were two light-emitting diodes (LED) with a pinhole in front of them to approximate the object modelled by the CRLB in the previous section. The sources were aligned using a beamsplitter (to combine the two LEDs) so that they overlapped to give the appearance of a single source. After the beamsplitter, the source was collimated using an achromatic collimating lens, so that the distance between the source and dispersion element did not affect the measurement. In the experimental setup, only two diodes with center wavelengths at at $560nm$ and $645nm$ were used in the setup. The center wavelengths were determined by a Young's double-slit experiment. The double-slit experiment is discussed in more detail in section 4.2.

The $f_{bias}$ parameter is inherent to the lens and is dependent on both the radius of curvature and the index of refraction. Both $\alpha$ and $f_{bias}$ were measured in the lab, and used in simulation. Equation (3.42) gives the un-normalized PSF of the lens which is normalized to unit magnitude for the reconstruction algorithm (see previous section). Experimentally, multiple images were taken at each defocus plane. The images were then added together to simulate varying exposure times. In the experimental setup, there was a significant amount of stray light present adding to a non-wavelength specific diffuse background. To compensate for the diffuse lighting experimentally, a background image was taken along with each defocus plane. If a background is otherwise unavailable, the amount of background could also be estimated after the fact similar to the derivation given above for estimating the image from an object estimate. However this research simply uses a measured background.

Table 4.1:     Experiment Parameters

| Parameter | Value | Units |
|-----------|-------|-------|
| $dx$ (Detector Pitch) | 16 | $\mu$m |
| $N$ (Detector size) | 512 | pixels |
| Aperture Diameter | 1 | cm |
| Number of wavelengths | 10 | |
| $\lambda_0$ (center wavelength) | 560 | nm |
| $\Delta\lambda$ (wavelength spacing simulation) | 10-100 | nm |
| Minimum-Maximum simulated wavelengths ($\lambda_{min} - \lambda_{max}$) | 560-645 | nm |
| Experimental wavelengths | 560/645 | nm |
| $f_{\lambda_0}$ (Focal length @ $\lambda_0$) | 441.6 | mm |
| $\alpha$ ($\frac{\Delta_f}{\Delta\lambda}$ measured from lens) | 1.2406x$10^5$ | |
| $f_{bias}$ (minimum focal length) | 373.4 | mm |
| $K$ (Number of defocus planes) | 3-20 | |
| Minimum/Maximum Distance ($z_d$) | 420.4/469.2 | mm |
| $\Delta_{z_d}$ (Distance between each defocus plane) | 0.26 | mm |
| Number of images per defocus plane | 500 | |
| Number of iterations for reconstruction | 2000 | |
| Number of noisy realizations | 500 | |
| Diode 1 intensity (550nm) | 3.64 x $10^{18}$ | Photons/frame |
| Diode 2 intensity (645nm) | 1.82 x $10^{18}$ | Photons/frame |
| Background intensity (645nm) | 3.56 x $10^{12}$ | Photons/frame |

A digital camera only measures light intensity in digital counts. Because the projection-based reconstructor assumes Poisson statistics, the measured data needs to be scaled to reflect the number of photons sensed, not the number of photoelectrons generated (whole number digital counts). Knowing that the Poisson statistics have both an expected value that equals the variance, the data was assumed scaled so that the variance matched the mean by dividing by the standard deviation of the data itself, and multiplying by the square root of the mean thus scaling the variance to the mean of the digital counts and enforcing Poisson statistics:

$$d_{photons}(x,y) = E_{x,y}[d_{counts}(x,y)]\frac{d_{counts}(x,y)}{std[d_{counts}(x,y)]} \tag{4.1}$$

Both the simulated and collected images, were scaled in this way according to the data measured from the camera, thus converting the units to photons for the reconstruction algorithm. Any read noise or other additive white Gaussian noise is assumed to be measured in the background. These simulated or experimental images were then summed down each row to use the projection algorithm discussed in section 3.1.

## 4.2   Laboratory Calibration of Sources

An experiment was set up to mimic the schematic in figure 3.2. Two diodes were chosen to provide 100nm separation. The diodes were found to be approximately 560nm and 645nm (red and green) using a simple Young's double-slit experiment setup. In Young's double-slit experiment, two slits are used to form a diffraction pattern similar to the one in figure 4.2. The wavelength, the slit separation and the distances between the screen and the slits are related by:

$$L = \frac{\bar{\lambda}z}{a} \tag{4.2}$$

where $a$ is the slit separation, $L$ is the distance between the maxima, $z$ is the distance from the slits to the screen and $\bar{\lambda}$ is the center wavelength of the source (from [10]). This equation can be rearranged to give the wavelength as a function of the fringe
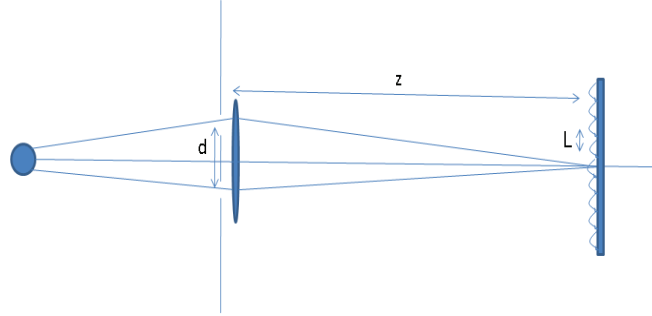
Figure 4.1:    Young's double-slit experiment setup

separation $(L)$ and ratio of the slit distance to lens distance $\left(\frac{z}{a}\right)$.

$$\bar{\lambda} = L\frac{a}{z} \tag{4.3}$$

A laser with a wavelength of 632.8nm was used to determine the distance ratio $\frac{a}{z}$ (figure 4.2). Images were taken and the fringe separation $L$ was calculated. Figure 4.3 shows the measurement of this ratio for the calibration wavelength. The distance ratio was then calculated to be 79.1 nm/pixel. This ratio used with other diodes to determine the wavelength center of each diode. Figure 4.4 shows the fringe pattern from the higher wavelength diode chosen for this experiment. Because the fringes are saturated, it is not possible to find the center peak. However the distance between the outermost fringe peaks can clearly be seen. The distance between the two outer peaks was found, and the average period calculated. It can be shown from figure 4.5 that
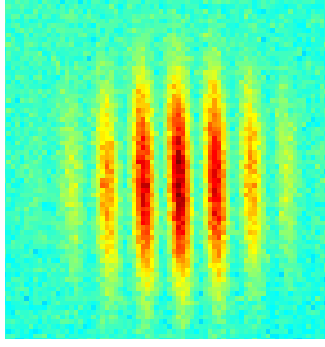
Figure 4.2:    Fringes for calibration source at $\bar{\lambda}$=632.8nm

the average fringe period distance $L = 8.17$ pixels and from equation (4.2), the diode wavelength is found to be $\lambda = 645nm$. Only the center wavelength can be determined from a simple double-split experiment. It is not possible to determine an accurate line-width with this setup. Therefore, the diodes were chosen with center wavelengths far enough apart so the bandwidth would not interfere with the verification of spectral resolution.

## 4.3   Determination of Lens Dispersion

In this section, a Focus Aberration Detection (FAD) algorithm is adapted to determine the amount of focus aberration present at each wavelength using an algorithm developed for a polarimeter using phase diversity (a defocus aberration) [30]. Since the diversity element between this research and the polarimeter research is a defocus aberration, the FAD algorithm is easily adapted to the determination of the lens-dispersion parameter. This algorithm pre-computes the focus aberrations and uses a step similar to the Richardson-Lucy algorithm to deconvolve the focus from the object. Finally, the log-likelihood ratio is computed and a probability of the focus aberration is applied computing the Maximum-a-Posteriori probability of the focus aberration. In this implementation, because the approximate focal length is known to within a certain range, only the Maximum-Likelihood estimation is needed.
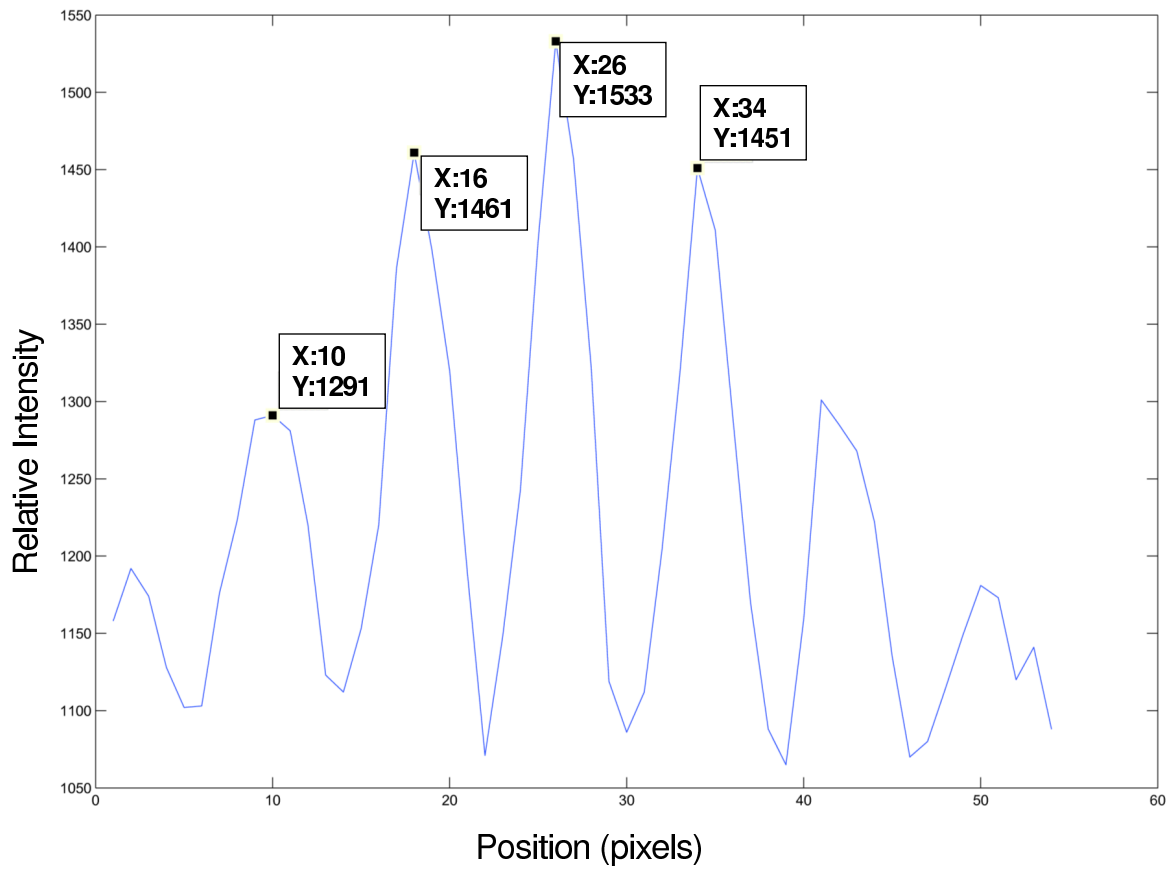
Figure 4.3:    Calibration fringe distance was found to be $L = 8$ pixels
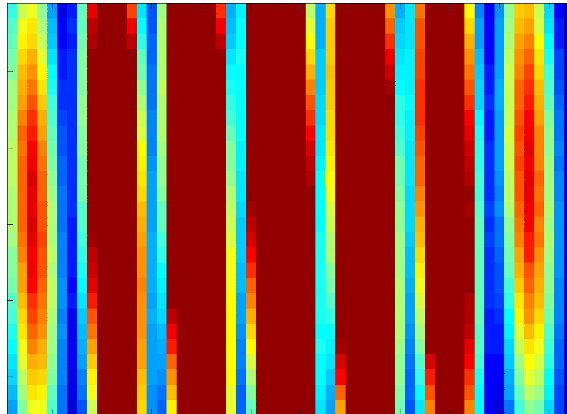


Figure 4.4:    Young's double-slit interference pattern with $\lambda_0$=645nm
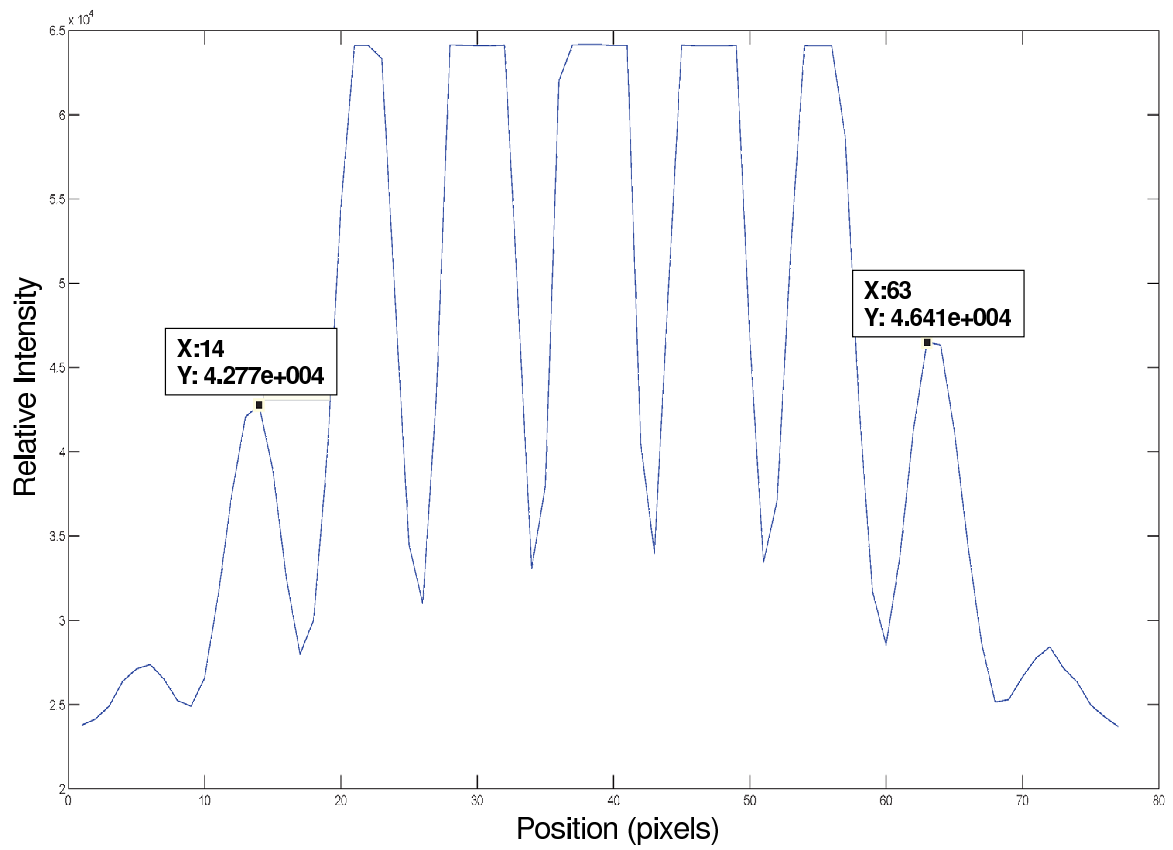
Figure 4.5:     Data to determine diode wavelength

The modification to the FAD algorithm has 4 steps. First start by generating a series of phases between minimum aberration and some upper limit of focus in this case chosen to be between minimal and maximal focal lengths observed in the lab for the LEDs above. Secondly, deconvolve the object from the measured image. Third, calculate the log likelihood for each focus aberration. Finally, find the maximum likelihood which corresponds to the focus aberration for the lens at the specific wavelength.

A PSF for defocus is given by:

$$h_k(k,p,\lambda) = \frac{\Delta_\xi^4 \left| \sum_{m,n} A(m,n) \exp\left[ \frac{\pi j(m^2+n^2)}{\lambda} \left( \frac{\lambda^2 z_d}{N^2 dx^2} - \frac{\lambda^2 z_d^2}{(\alpha\lambda+\beta_{fl})N^2 dx^2} \right) \right] \exp\left[ \frac{-2\pi j(km+np)}{N} \right] \right|^2}{\Delta_\xi^4 \left| \sum_{m,n} A(m,n) \exp\left[ \frac{\pi j(m^2+n^2)}{\lambda} \left( \frac{\lambda^2 z_d}{N^2 dx^2} - \frac{\lambda^2 z_d^2}{(\alpha\lambda+\beta_{fl})N^2 dx^2} \right) \right] \sum_{x,y} \exp\left[ \frac{-2\pi j(km+np)}{N} \right] \right|^2}$$

$$(4.4)$$

(the same as equation (2.32)). From this PSF, the defocus $W_d$ is varied over the distances listed in table 4.1 around the focus for the center wavelength $\lambda_0$. This is done for both wavelengths determined above.

The log likelihood for a single defocus frame is given by:

$$L_D(d) = ln[P_D(d)] = \sum_y \sum_x \sum_k d_k(x,y)ln[i_k(x,y)] - i_k(x,y) - ln[d_k(x,y)!] \quad (4.5)$$

(the same as equation (3.1)).

The equation for $W_d$ is given by:

$$W_d = -\frac{w^2}{2}\left( \frac{1}{z_d} - \frac{1}{z_i} \right) \quad (4.6)$$

(the same as equation (2.28)), and using the two wavelengths determined above, the lens model parameters $\alpha$ and $\beta_{fl}$ can be computed. The parameters are listed in table 4.1 given above. Figures 4.6 and 4.7 show the results of the laboratory calibration. Notice that the PSFs for the $645nm$ LED do not visually match as well, however the
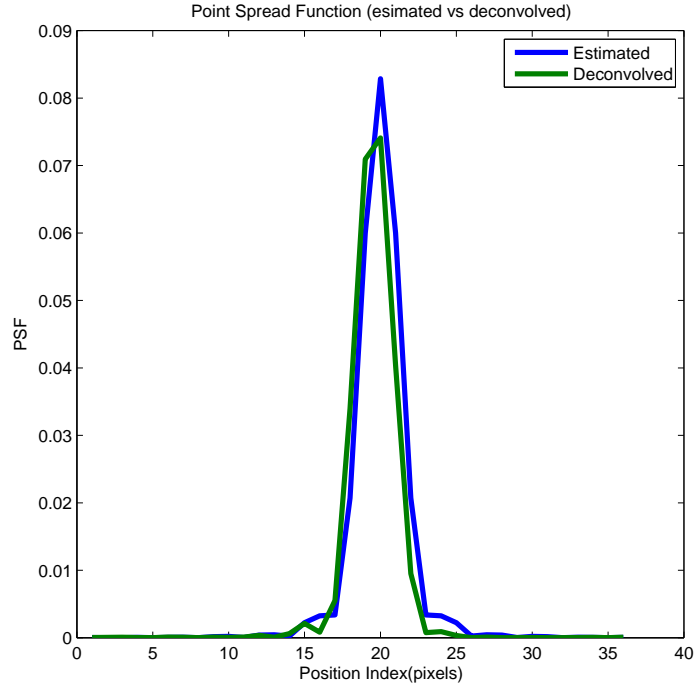
Figure 4.6:    PSF estimated vs deconvolved for $\lambda = 560nm$

defocus of the log-likelihood function was found to match closely. This is due to the fact that although defocus is the main aberration present in the lens, some of the higher order aberrations may also be present. The energy away from the peak has a much greater overlap and thus this correlation is much higher in the first ($\lambda = 560nm$) LED.
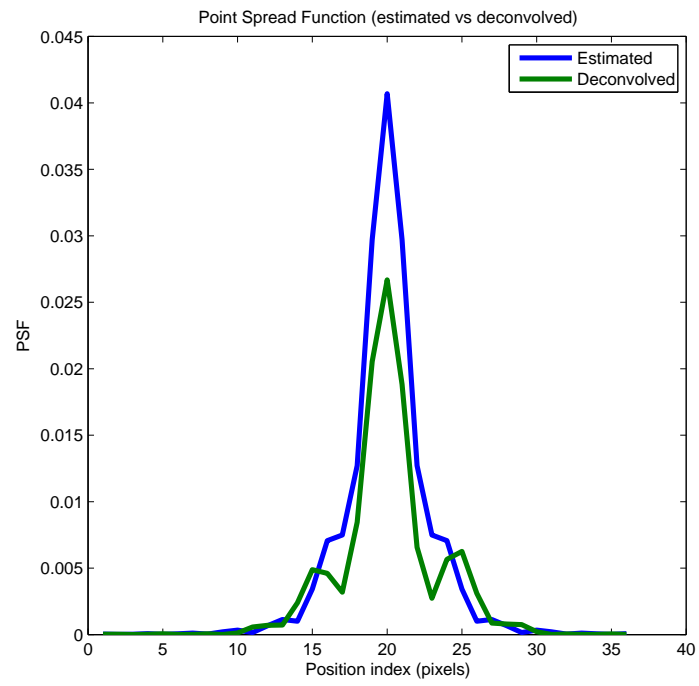
Figure 4.7: PSF estimated vs deconvolved for $\lambda = 645nm$

# V.  Simulation and Experiment Results

The purpose of this chapter is to describe a simulation and laboratory verification of the resolution limits of lens-based chromotomagraphic hyperspectral sensor. In order to accomplish this, a simulation was performed using to determine the effect of number of defocus planes on spectral resolution. These simulations were performed for multiple wavelength spacing and varying numbers of defocus planes. In the previous chapter, comparisons of various parameters for the CRLB indicated that the largest factor affecting lens-based CTHIS resolution is the spacing and number of defocus planes. Each increase in the number of defocus planes in the simulation was accompanied by a corresponding reduction in integration time, thus the total energy in each set of collected images is the same. In section 3.1, a projection based reconstructor was developed similar to a previous method [12] that solves for the spectrum of the scene in a single spatial dimension and single spectral dimension. Next, in section 3.2, the setup for the laboratory and the experiment are described. Finally, a laboratory experiment performed to verify a single instance of the CRLB and simulation for the lens-based CTHIS is described in section 5.4.

## 5.1  Effects of Lens-Based Dispersion on Spatial and Spectral Resolution

As mentioned in section 3.1, the reconstruction is given as an iterative EM estimator that attempts to maximuze the likelihood. The object estimator began to converge around 200 iterations. The image photon bias $\beta$ was chosen to be 10 so that the estimator would converge to a reasonable solution. As seen in figures 5.5 and 5.6, even this small amount of bias adds a great deal of noise to the images, and results in a longer convergence time for the estimator. Figure 5.1 gives an example of object reconstructions without and with bias (using only 1 spatial dimension). The results of bias on the reconstruction are easily seen. The peaks can be clearly shown in the reconstruction with bias, although there are many false peaks and the spectrum is blurred across many more wavelengths. Even though the of the bias reconstructed spectrum is blurred, there are peaks at the expected locations. The

64
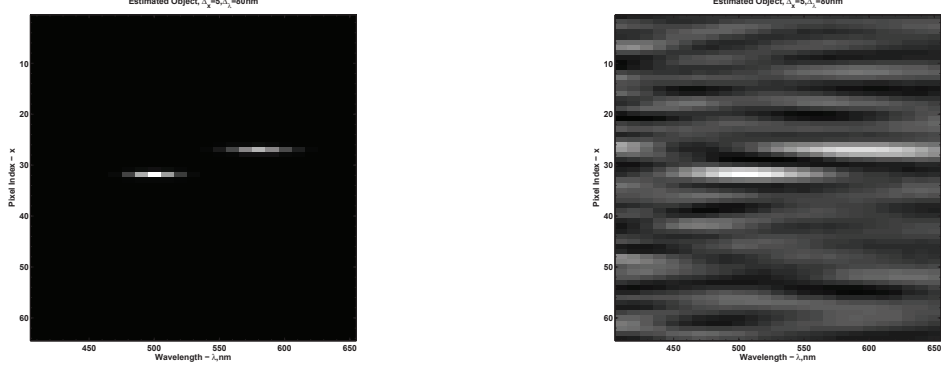
Figure 5.1: Example Reconstructions without (left) and with (right Bias after 200 iterations

spatial reconstruction converges quickly to the locations of the point sources (requiring only a few iterations). However the spectrum takes many more iterations to show obvious peaks.

The CRLB is used as a metric to describe the spatial and spectral resolution of a system. Specifically, we use the standard deviation (the square root of the CRLB), and where our standard deviation is lower, the resolution is considered higher [19]. This is equivalent to saying that when our estimator standard deviation is greater than our actual point source separation, it is impossible to resolve the object. The lens-based implementation differs from other CTHIS implementations, and using the CRLB is not as straightforward as a spatial resolution criteria. In previous work, a CRLB was used as an estimate of the resolution of two variations of CTHIS sensors [19]. The prism and grating CTHIS configurations correlate spatial and spectral information across the resulting images, and therefore an ambiguity of the actual spatial resolution results. Because a change in spatial location in a resulting image may be due to a spatial variation of the extended object, or due to a different wavelength feature, the variance of the spatial separation estimates were compared with the actual wavelength separation. This showed that the spatial resolution of the CTHIS sensor for the grating and prism configurations varied with the spatial separation of the object.

65
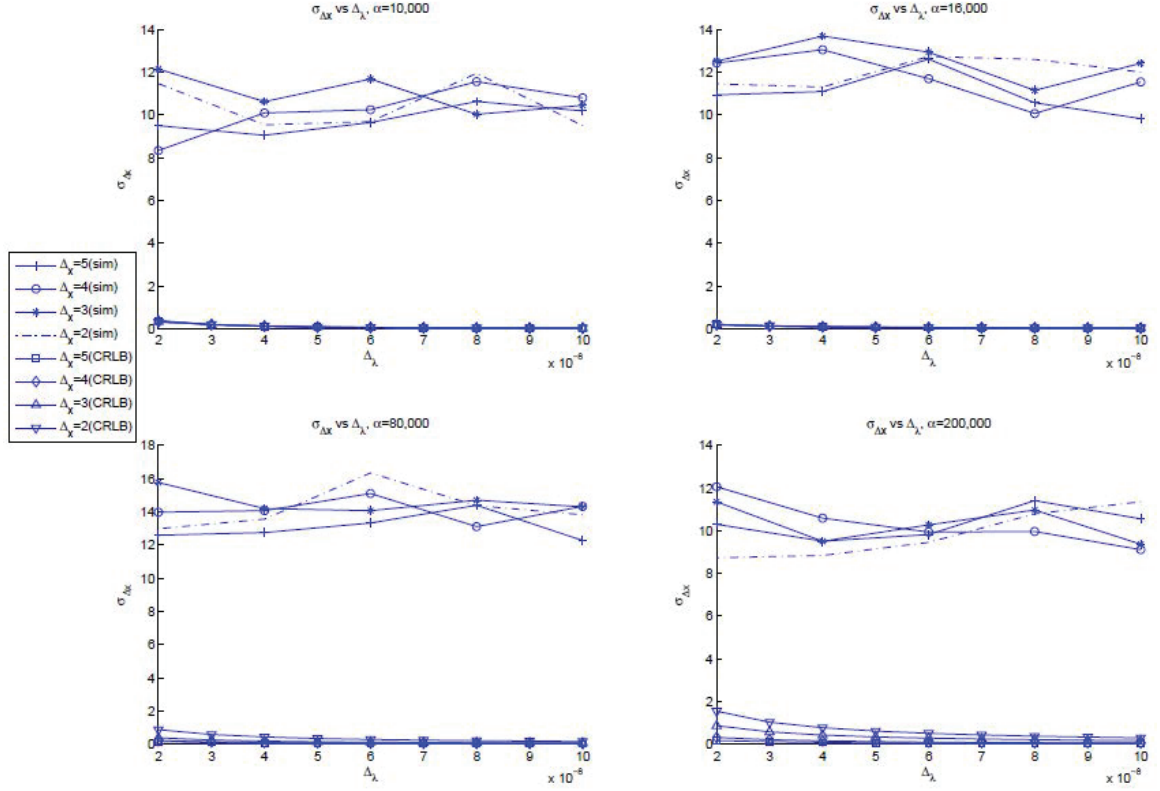
Figure 5.2: Spatial Resolution Estimates vs. Spectral Separation

However, in the case of the lens-based CTHIS, because the spectral diversity varies across multiple images, we do not expect the spatial resolution to be different than a diffraction-limited optical system. Figure 5.2 shows the standard deviation and simulation results across varying values of both spectral separation and the dispersion parameter $\alpha$. The lower bound obviously bounds the performance of the simulation, and matches the general trend. The CRLB is relatively flat with a changing spectral separation. Changing the object's spatial separation also does not appear to affect the standard deviation. Almost all of the simulated points are below the Rayleigh limit (the minimum Rayleigh limit for this system is 2.5 pixels at $\lambda = 410nm$). The CRLB is only a bound on the best estimator performance, and is not necessarily achievable. When the calculated standard deviation is below the Rayleigh limit, the defocused images must be providing more information than a typical imaging system. There may be special object cases where, for this configuration, beyond diffraction-limited

resolution is possible. For instance, the object under consideration with two points spaced closely, but distant spectrally obviously benefits from the increased information provided by the extra frames (which happens to be the object we are estimating). In this case, it would be obvious there are two points present due to the fact that there will be almost mutually exclusive zones where one point is in focus, and the other point is out of focus (see figure 5.5 for an example). Simply observing that there are two zones where points are in focus renders the conclusion that there are two points. This problem is much more difficult when the object has many closely spaced points at various wavelengths because there is no obvious distinction between the defocused images. Although the trend of the simulation is not flat, there is no obvious trend with the changing spectral or spatial separation. As a result, we conclude that for an average object that the best spatial separation we can expect from a lens-based CTHIS would be around the same as the diffraction-limited optical system.

The spectral resolution is of significant interest. Figure 5.3 shows the standard deviation of spectral resolution estimates against the spectral dispersion parameter $\alpha$. There is a trend in both the simulation and the CRLB. As $\alpha$ varies, there is a minima where both the CRLB and the simulation give the lowest $\sigma_{\Delta_\lambda}$ before and after which, the standard deviation increases. This minima occurs for each spectral separation $\Delta_\lambda$, as it increases this minima requires a stronger dispersion (a higher $\alpha$). When $\Delta_\lambda = 100nm$, the minima occurs for $\alpha = 80,000$, when $\Delta_\lambda = 60nm$, the minima occurs at or near $\alpha = 200,000$, and beyond this (for $\Delta_\lambda < 40nm$), the minima occurs for $\alpha$ beyond the simulation and CRLB parameters. This indicates that for a desired spectral separation (object), there is a particular chromatic aberration that will resolve the object, but beyond which the resolution will get worse. In other words, for a particular lens with a known chromatic aberration, there is a "sweet spot" for its spectral resolution showing the best performance we can expect for the CTHIS system. That minima is the limit of performance for the given optical setup, given the particular object.
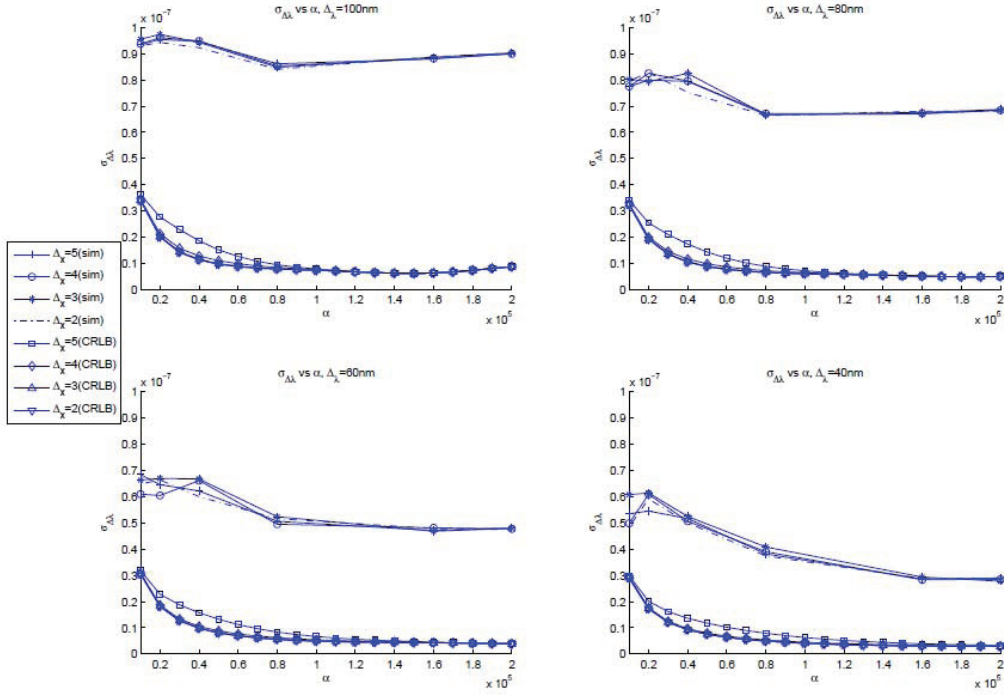
Figure 5.3:    Spectral Resolution Estimates vs. Spectral Dispersion

The number of defocused planes and the distances ($z_d$) also affects the standard deviation of the estimator, and these results are discussed in 5.4, however for this initial study it was fixed at 20 (planes) and varied $\pm 1cm$. Increasing the number of defocused planes would require a precision stage with which to move the lens with respect to the focal plane, but it was determined that it is relatively simple to move the stage in approximately $1mm$ increments. We would expect the $\alpha$ parameter to dictate an appropriate number of defocus planes, and in turn, the effects on spectral resolution. These results mentioned in [18], became the basis for the results reported in section 5.4.

The Cramer-Rao lower bound was used as a method for determining the expected resolution performance of a lens-based hyperspectral imaging sensor based on the lens-dispersion parameter. This bound was verified to be a lower bound on the expected spatial and spectral resolution of the CTHIS using simulation. Due to the fact that the spectral variation is spread across multiple images, and not spatially

68
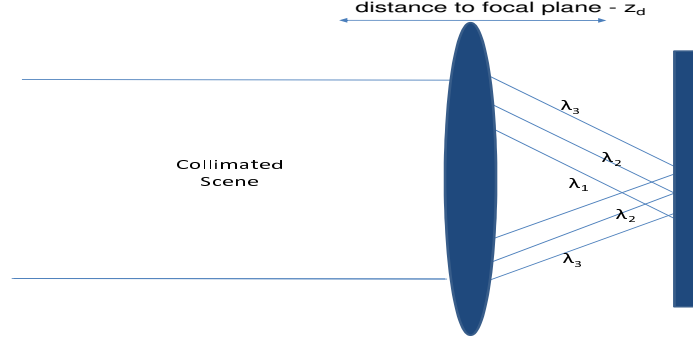
Figure 5.4:    Simplified Optical Setup

as in the grating and prism based CTHIS, the spatial resolution was determined to be similar to that of a diffraction-limited imaging system. The spectral resolution is heavily dependent on the spectral dispersion of the lens in the system. It was determined that each value of $\alpha$ yields a particular "best" point of spectral resolution. However it was also determined that the number of defocus planes was another parameter that affects spectral resolution and was not captured in this particular use of the CRLB.

## 5.2    Numerical CRLB Computation

The CRLB given in section 2.4 was computed for the properties given in table 5.1. Then, the resulting images had a bias $\beta$ added and noise was then applied according to Poisson statistics. The bias simulates unrelated points in a scene, and also arbitrarily increases the signal to noise ratio (SNR) of the images. The bias was also added to the CRLB, and then calculated to make the bound more realistic. The final image then becomes:

$$i_k(x, y) = o_1 h_k(x - x_0, y - y_0, \lambda_0) + o_2 h_k(x - (x_0 + \Delta_x), y - y_0, \lambda_0 + \Delta_\lambda) + \beta \quad (5.1)$$

and is used in equation (2.15). Because $\beta$ is a constant, it only modifies $i_k(x, y)$ and does not contribute to the derivatives for the Fisher information matrix elements.

69
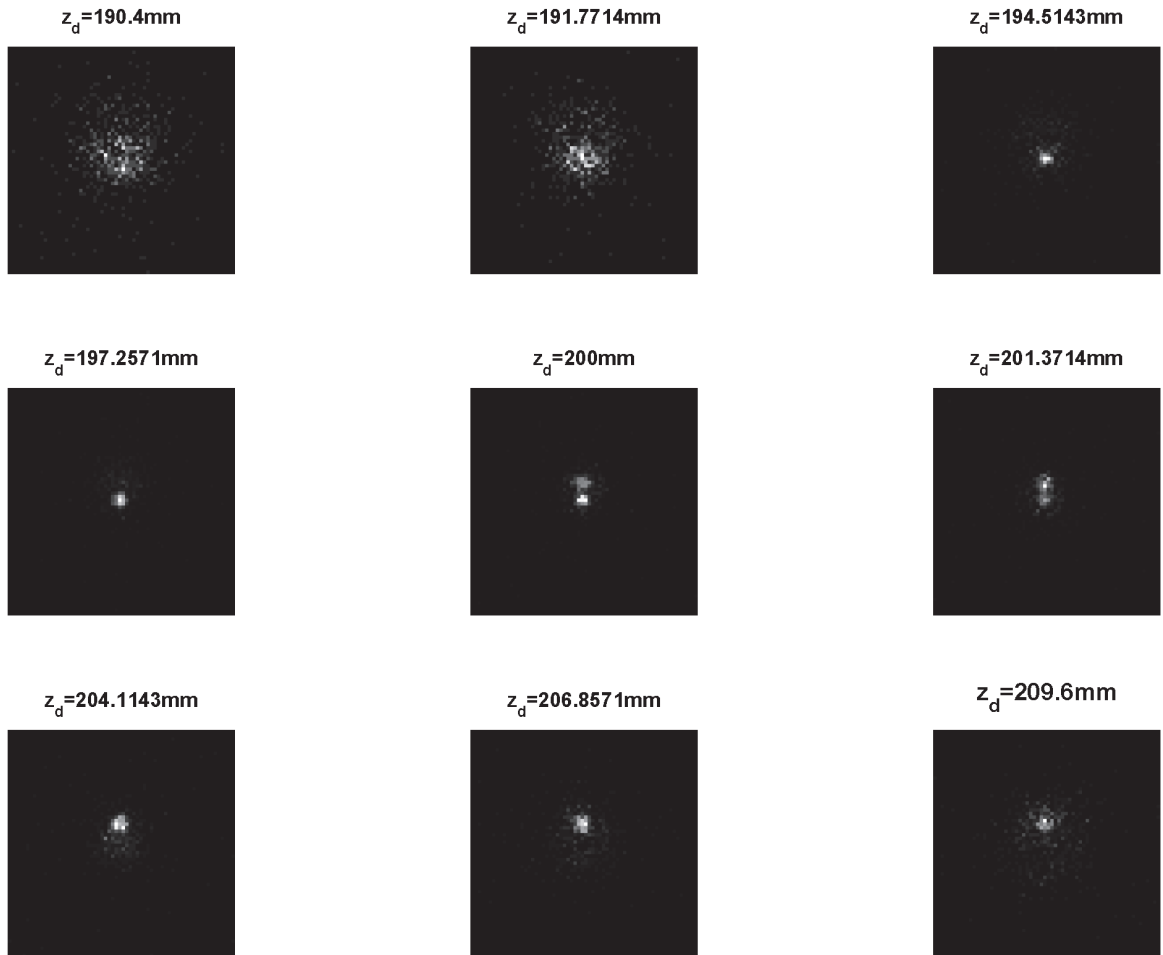
Figure 5.5:    Simulated Defocused Images with Poisson Noise

Examples of images with Poisson noise are given in figures 5.5 and 5.6 without and with a bias respectively.

| Parameter Name | Value |
|---|---|
| $\lambda$ | $410nm - 650nm$ |
| $\lambda_0$ | $530nm$ |
| $f@\lambda_0$ | $200mm$ |
| $\beta_{fl}$ | 158mm |
| $z_d$ | 190-210mm |
| # of defocused planes | 3-40 |
| pixel size (dx) | $8\mu m$ |
| # of pixels | 64 |
| Source Intensity ($o1, o2$) | 300 photons |
| Image Bias $\beta$ | 10 photons |
| Aperture Radius | $2.1mm$ |
| $\alpha$ | $12 \times 10^4$ |
| $\Delta_x$ | $1 - 10$ pixels |
| $\Delta_\lambda$ | $10 - 100nm$ |

Table 5.1:    CRLB Parameters

The wavelengths were chosen over the visible spectrum because many lenses with severe chromatic aberration are available, and a wide variety of inexpensive detectors are available. The parameters for pixel size ($dx$), defocused distances ($z_d$), and aperture diameter were chosen because they reflect a realistic optical system setup. The aperture diameter specifically samples at twice the Nyquist rate for the Rayleigh criteria of the pixel size. The spectral dispersion parameter $\alpha$ was chosen to correspond to a real lens used in a laboratory setup (see chapter V). The maximum number of defocused planes $k$ was fixed at 40 because it corresponds to a physical distance of approximately 0.5mm. The number of defocus planes were varied between 3 and 40 and varying starting positions were chosen so as to reduce the dependance of the variance on the start position, and to characterize the resolution dependance simply on the number of frames. The point source intensities were chosen for a very low signal setup, and the image bias was chosen to be much less severe because it was determined that any higher bias noise significantly degrades the performance of
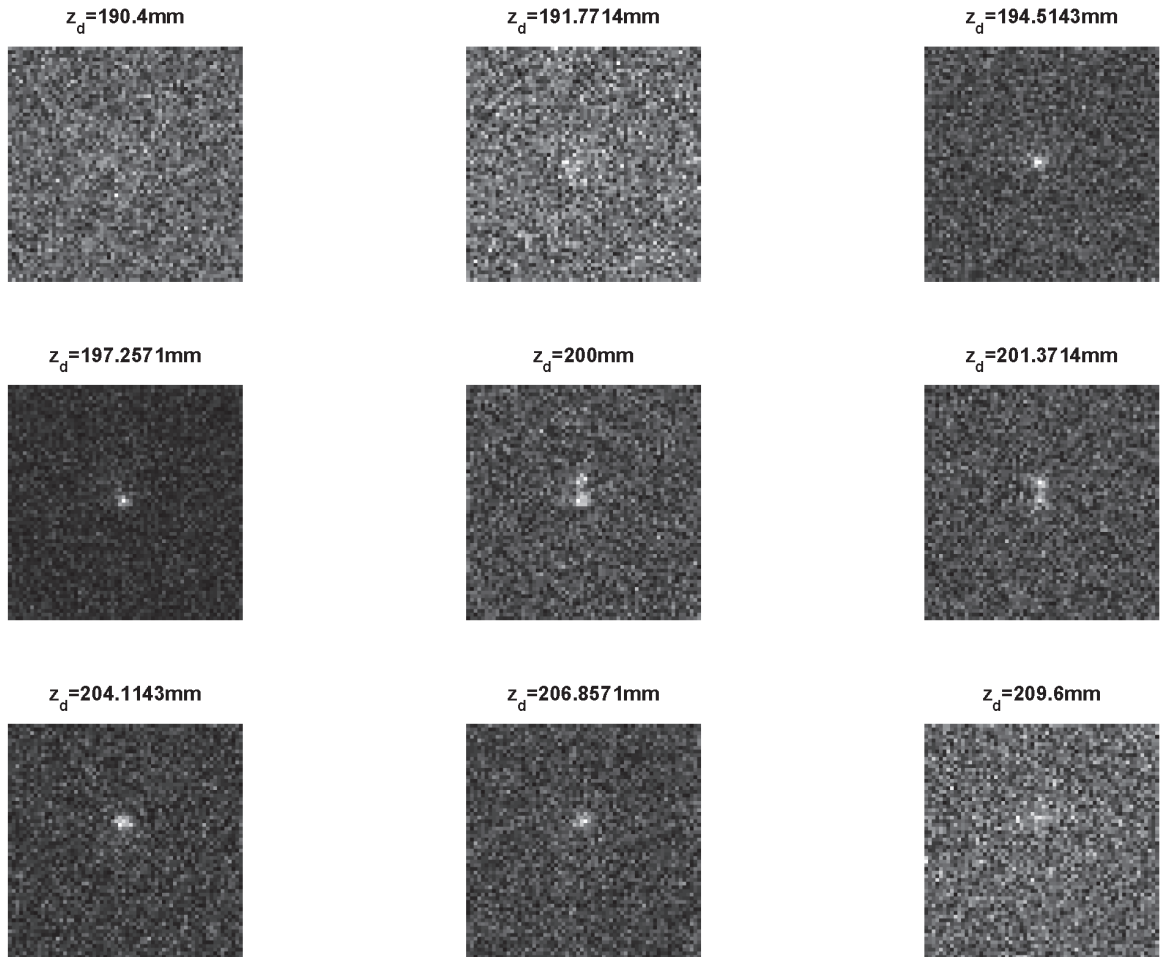
Figure 5.6:    Simulated Defocused Images with Poisson Noise and Bias

an estimator. The $k$, $\Delta_x$ and $\Delta_\lambda$ parameters were then varied in the simulation over the specified ranges in table 5.1.

After the CRLB was computed for the individual images, the summation over $k$ was taken last. Recalling that equation (2.15) is an element of the Fisher information matrix for a series of images, if $o_1$ and $o_2$ are held constant for each image, then the amount of light collected will be greater the more frames are collected. To scale the photon count for the number images collected, equation (2.15) was modified to:

$$F_{ij} = \frac{1}{K} \sum_y \sum_x \sum_k \frac{1}{i_k(x,y)} \frac{\partial i_k(x,y)}{\partial \phi_i} \frac{\partial i_k(x,y)}{\partial \phi_j} \tag{5.2}$$

where $K$ is the total number of frames collected. This normalizes the number of photons across the all the images computed to be constant regardless of the number of frames collected. This ensures that collecting more images does not result in a lower variance simply because more photons were collected. This is the same as scaling the photons in each object to account for camera integration time.

### 5.3   CRLB Results

As mentioned in section 2.1, the CRLB is used as a metric to describe the spatial and spectral resolution of a system. Specifically, we use the standard deviation (the square root of the CRLB), and where our standard deviation is lower, the resolution is considered higher [19]. This is equivalent to saying that when our estimator standard deviation is greater than our actual point source separation, it is impossible to resolve the object. The standard deviations from the CRLB $\sigma_{\Delta_x}$ and $\sigma_{\Delta_\lambda}$ were then compared with $\Delta_x$ and $\Delta_\lambda$ used to generate them, and to the number of frames for varying CRLB calculations. Specifically using the criteria in equation (2.1), we have

$$\frac{\Delta_x}{2\sigma_{\Delta_x}} = 1$$
$$\frac{\Delta_\lambda}{2\sigma_{\Delta_\lambda}} = 1 \tag{5.3}$$

73

The number of frames required to resolve a spectral feature were calculated. For example in figure 5.7, the line for $\Delta_\lambda = 10nm$ never is never below $20nm$ and is therefore not resolvable using up to 40 frames to estimate the scene. It may be that it is resolvable with greater than 40 frames, however for this research, the 40 frames was the maximum number considered. Only values for $\Delta_\lambda = 10 - 40nm$ are shown because for $\Delta_\lambda > 50nm$, the lines are too closely spaced to differentiate them significantly in a graph. For spatial resolution, figure 5.8 shows an example of the
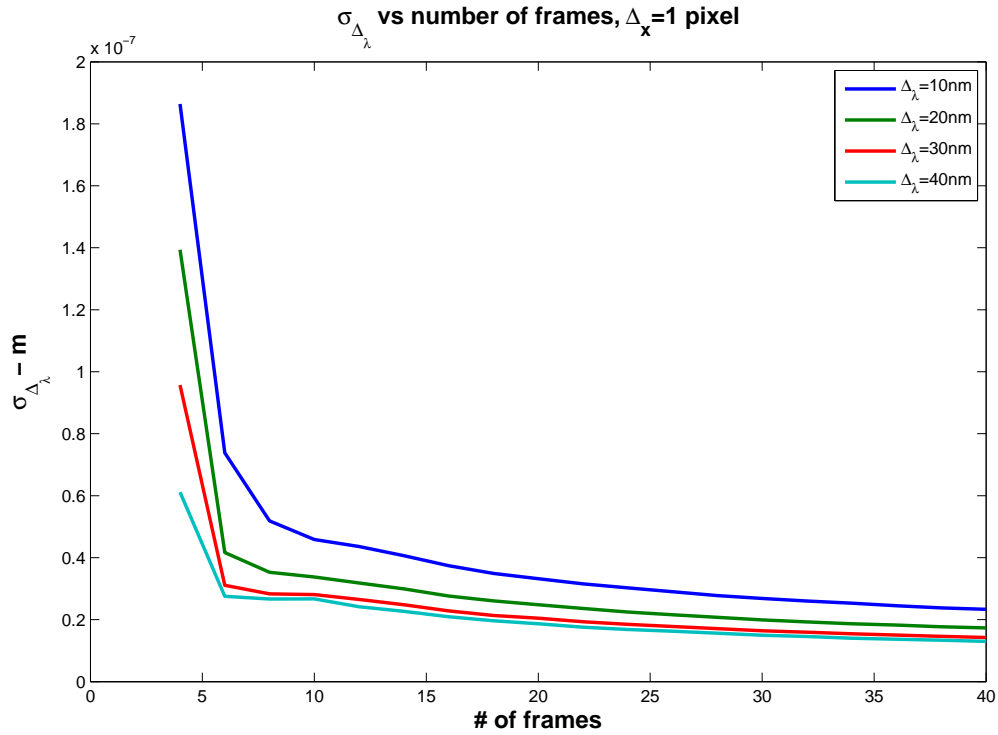


Figure 5.7: Spectral Standard Deviation versus the number of frames. Notice that the $\Delta_\lambda = 10nm$ line is not resolvable.

standard deviation $\sigma_{\Delta_\lambda}$ as a function of the number of frames. In this graph, there is also an unresolvable line. Notice how for $\Delta_x = 1$, the standard deviation is always greater than 2. This shows that for $\Delta_x = 1$ with 40 or fewer frames, two closely-spaced points are unlikely to ever be resolvable. These calculations were made for $\Delta_x = 1 - 10$ pixels and $\Delta_\lambda = 10 - 100nm$. The point where the ratio in equation (2.1) is closest to one, was calculated and the number of frames required for resolving

74
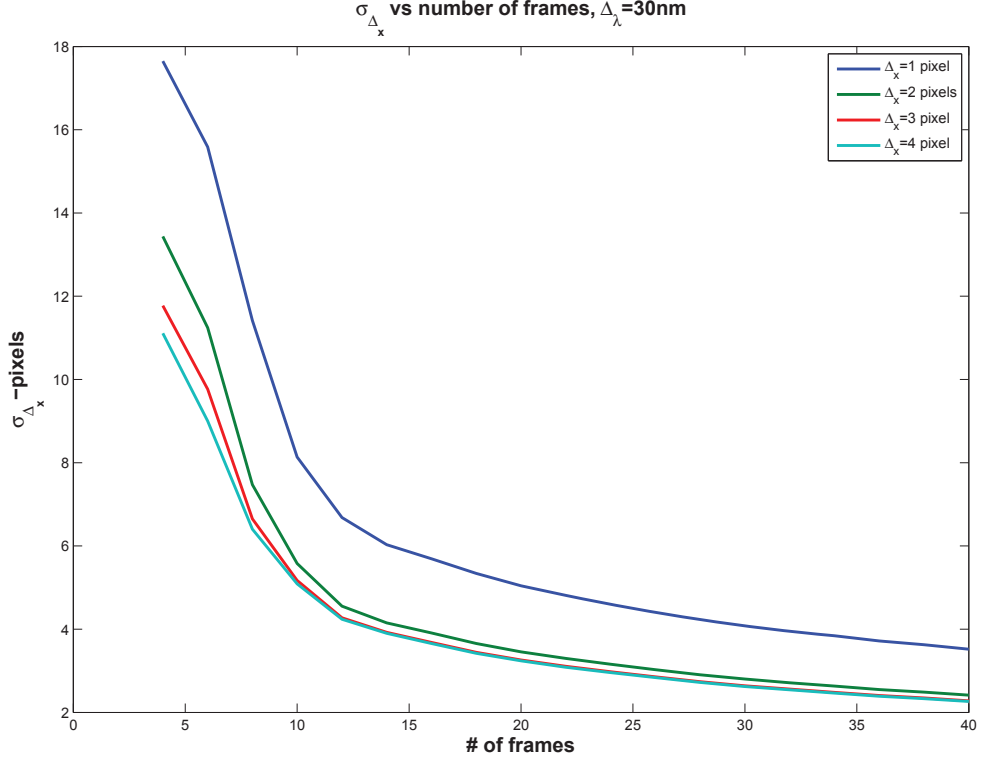
Figure 5.8: Spatial Standard Deviation computed from the CRLB versus the number of frames. Notice $\Delta_x = 1$ pixel is not resolvable.

the two points was recorded. Figure 5.9 shows this calculation for spatial resolution. Only $\Delta_\lambda = 10 - 40nm$ points are shown to illustrate the trend. This figure shows that only a few frames more or less are needed for even a large difference in $\Delta_\lambda$. As one would expect, this indicates that the spatial resolution of a CTHIS system behaves similarly to a diffraction-limited optical system and does not vary significantly when points are spectrally far apart. When both $\Delta_x$ and $\Delta_\lambda$ are close together, many more frames are needed to resolve the points. When the points get spectrally farther apart (increasing $\Delta_\lambda$), only a few frames difference is required. There may also be special cases where beyond diffraction-limited resolution is possible. If two points are spaced closely ($\Delta_x$ small), but distant spectrally, then there is obviously a benefit from the increased information provided by the extra frames. It should be obvious that two points are present in the scene if there are two mutually exclusive zones where one
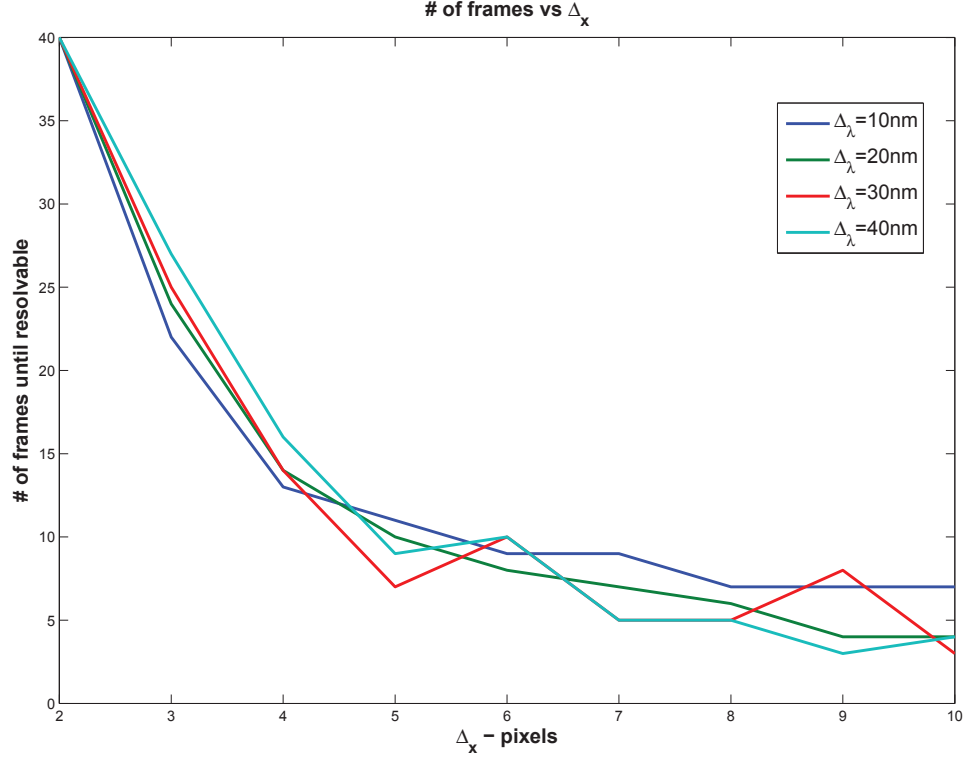
Figure 5.9: Number of frames required to resolve various spatial separations using the CRLB and standard deviation-based resolution metric. Only a few frames difference are needed for various $\Delta_\lambda$ values.

point is in focus, and the other point is out of focus. The spatial resolution is improved by knowing the spectral characteristics of the lens. This simple object however is not as common, and beyond diffraction-limited resolution should not be normal given an average object. Because of this, we conclude that for an average spectral scene, the spatial resolution of the CTHIS should not be significantly different from a diffraction-limited case.

For spectral resolution, figure 5.10 shows the number of frames required to resolve 2 points spectrally. For $\Delta_x = 2 - 4$ pixels, fewer frames are needed to resolve the points when $\Delta_\lambda$ is small. As $\Delta_\lambda$ increases, fewer frames are needed to see the spectrum of the object. Notice that for $\Delta_x = 5 - 7$, only $\Delta_x = 7$ appears to be shown. That is because for the CRLB, the profile for $\Delta_x > 4$ is exactly the same. In other

words, when the points are much farther apart spatially, it is much easier to resolve the points spectrally. For this case, beyond $\Delta_x > 4$ pixels, there is no difference in the number of frames required to determine the spectrum of those points. When $\Delta_x$
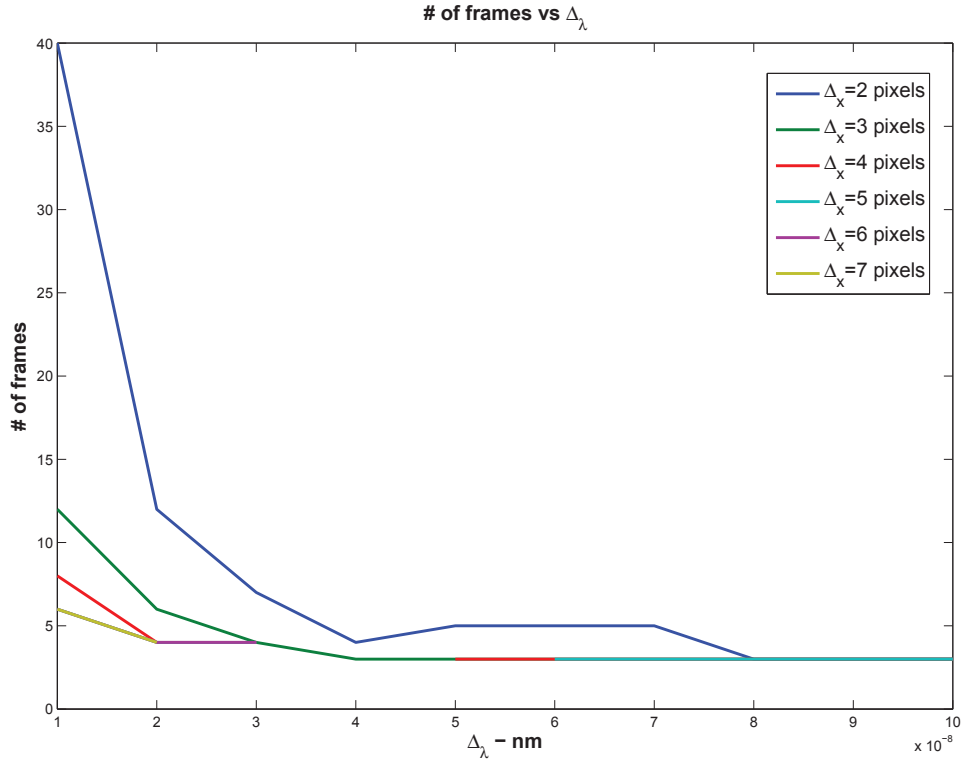


Figure 5.10: Number of frames required to resolve various spectral separations.

is small, many more frames are needed to determine the spectrum. Finally, the closer the spectrum is spaced, the more frames are needed. As a result, it seems obvious that a coarse resolution spectrometer can be made using a very simple standard optical setup, for only a slightly higher cost of data collection and computation. The chromatic aberration of a lens is something that is present in many optical systems, and the possibility of collecting more information for only a slightly higher complexity is very appealing.

## 5.4 Spectral Resolution of Lens-Based CTHIS

In the previous chapter a resolution criteria based on the minimum estimator variance was presented. The CRLB was given for a low-signal scenario. This was done because initial measurements indicated that the signal to noise ratio was low. After the data was measured and converted to photons, it was found that the signal to noise ratio was very high. Also, after simulating the reconstruction method developed above over 500 different noise realizations, it was found that reconstructions did not vary within 10 orders of magnitude due to noise, and another resolution criteria needed to be developed. This section discusses the new resolution criteria, and the results of both the simulation and the experiment.

*5.4.1 Resolution Criteria.* After noisy images were simulated, the reconstructor developed in section 3.1 was used to reconstruct the object for varying lens positions. Multiple noisy simulations were used however, the Poisson noise did not change the resulting reconstruction for varying noise samples. This is due to the fact that there is a very large signal to noise ratio. Therefore, only 1 realization of noise was used per frame, or simply stated, the simulation was not repeated multiple times per frame. Because of the lack of variation, a variance across multiple random realizations frames could not be determined.

In the experiment, positions were taken between the $420.4mm$ and $469.2mm$ from the camera. These were taken to give equal distances between the focal lengths for the 550nm and the $645nm$ and equal distances on either side of the focal length. A total of 20 positions were taken representing $2.5mm$ which was the smallest distance that could be taken with the measurement device. In simulation, the start position was taken between $420.4mm$ and $422mm$ and subdivided 40 times, to average for any resolution criteria no matter how many frames were used from 3-20. A minimum of 3 frames were taken so there was always 1 frame on either side of the focal point of the two LED wavelengths. Although more wavelengths were used in simulation, the experiment only had 2 wavelengths represented.

78
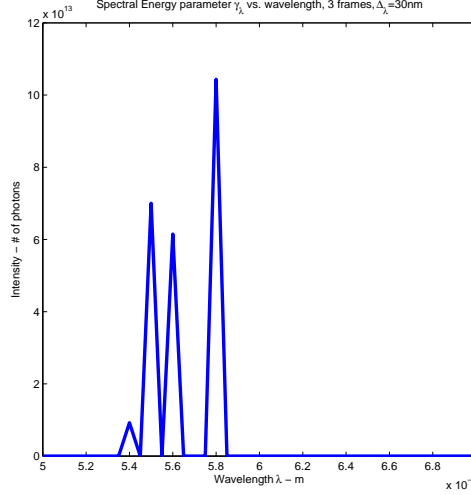
Figure 5.11:    Simulated reconstruction for $\Delta_\lambda$=30nm using 3 frames

After the images were simulated for this criteria, the objects were reconstructed. Since we are primarily concerned with spectral resolution for this study, only the spectral energy parameter $\gamma_\lambda$ was actually compared with the actual spectral separation $\Delta_\lambda$. Multiple iterations were attempted, and it was found that 2000 iterations worked best for both the simulated and experimental data. On average more iterations did not help the reconstruction further and in some cases increased the amount of noise present. When examined, reconstructions using only a few frames had multiple false peaks. For this simulation and experiment it is known that there are only 2 points. Figure 5.11 shows an example of multiple peaks for 3 frames. The primary peak should be at $\lambda = 550$nm, and another peak is expected at $\lambda = 580$nm. Notice the multiple peaks around the $\lambda = 550$nm, and that the peak at $\lambda = 580$nm is almost twice as large as the first peak, this is because the energy for the first point is spread across multiple wavelengths and more information is needed for an accurate reconstruction. Notice how when more frames are added, as in figure 5.12, the reconstruction algorithm is able to find the wavelengths of the two peaks, even down to 30nm in simulation. The peak at $\lambda = 550$nm has almost twice the number of photons as the second peak at 580nm. So for this analysis the number of peaks is used as a resolution criteria and when two peaks are detectable. When only two peaks are detected, then the image

79
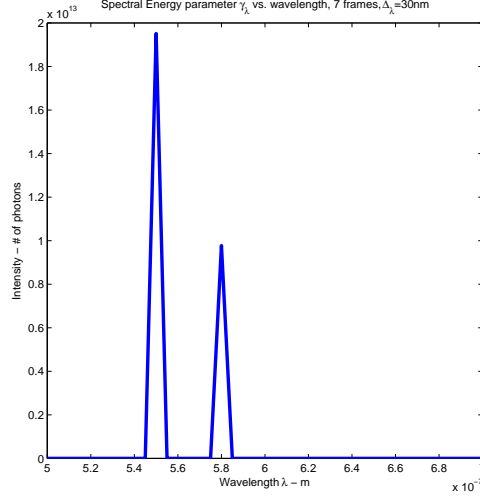
Figure 5.12:    Simulated reconstruction for $\Delta_\lambda$=30nm using 7 frames

is considered spectrally resolved. This resolution criteria is in keeping with the FAD algorithm discussed earlier, as well as other iterative maximum-likelihood estimators in the literature where the values for which the algorithm converges are considered the correct parameter for estimation. In the case of the FAD algorithm, the amount of focus error is considered a correct estimate when the estimation converges. Figure 5.11 represents an unresolved case and figure 5.12 represents a resolved case. A modified first derivative test was used to detect peaks. The first derivatives were taken and the zero crossings were determined to find the critical points. The zero crossing location were compared to determine if they were an inflection point, a minima or a maxima. If a maxima occurs at the critical point, the peaks were kept if they were within 2 orders of magnitude of the known intensity for the second peak (in this case at $580nm$). Specifically the threshold is at $5 \times 10^{11}$ for this case.

   *5.4.2   Simulation and Laboratory Results.*    Images were simulated and collected as described above for each set of different frames. The total number of frames were taken for each start position, then frames were successively added in and each set then was reconstructed using the algorithm developed in section 3.1, and the modified second derivative test applied to determine the peaks. The number of peaks over each
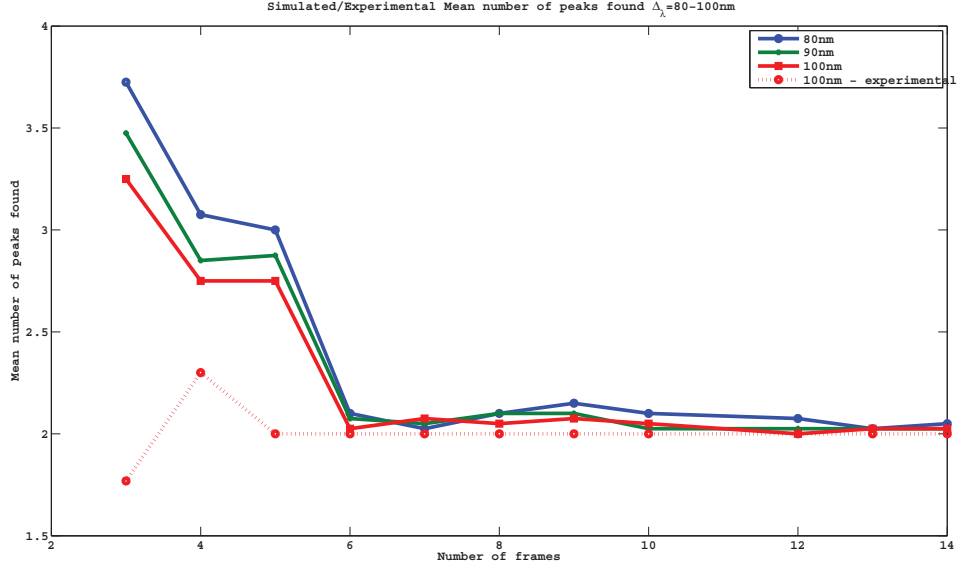
Figure 5.13:    Mean Number of peaks, simulated and experimental

start position was averaged for the simulation, and averaged using a weighted average for the experimental data. Figure 5.13 shows how the number of frames affects the average number of peaks for $80nm$ to $100nm$. Although the data was simulated for $10nm$ to $100nm$ only $80nm$ to $100nm$ is displayed because this region displays the clearest trend. As the wavelength increases, the number of peaks slightly decreases. In other words, the farther away two points are in spectrum, the better the reconstruction is, with fewer frames. Because the trend is so strong with only the first few frames between 3 frames and 7 frames, improvement due to increased $\Delta_\lambda$ is only slight, however it does demonstrate that the farther apart two wavelengths are being reconstructed, the easier it is to resolve them. Notice also that after 7 or 8 frames, almost all of the wavelengths are resolvable. At this point we have demonstrated the trend with wavelength on resolvability, we now seek to understand how closely the measured $\Delta_\lambda$ relates to the actual $\Delta_\lambda$. For the experimental data, we see the same trend: the farther apart the points, the fewer frames that are needed to resolve the data. Notice in figure 5.14 of the experimental data that the two points are clearly separated unlike figure 5.11 and are therefore resolvable. However, the intensities are

81
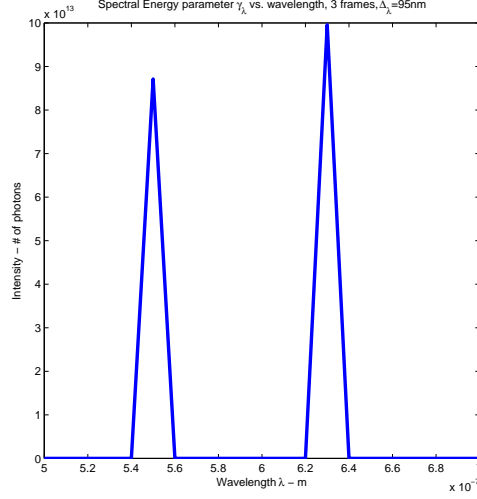
Figure 5.14: Experimental reconstruction for $\Delta_\lambda$=95nm using 3 frames

not the expected values. The first peak is at 550nm as expected, but the second peak is at $620nm$ which is only $\Delta_\lambda = 70$nm when the actual value is $\Delta_\lambda = 95$nm as determined by the Young's experiment described in section 4.2. The data is resolvable with only 3 frames, however the intensity and the spectral accuracy are still not what we expect. Figure 5.15 shows for an example of the experimental data that for 7 frames, the intensities are closer to their expected values, especially their relative values. However the spectral accuracy is still only $\Delta_\lambda = 80$nm rather than $\Delta_\lambda = 95$nm as expected. As another example using the full 20 frames reconstruction, the intensities are exactly where they should be, and the points are clearly resolvable, however, $\Delta_\lambda = 70nm$ rather than $\Delta_\lambda = 95nm$. The discrepancy in the measured spectral accuracy with the calibration vs. the reconstructed data may be due to the measurement error in the Young's calibration, or most likely due to the sensitivity of the reconstructed wavelength bins. Point spread functions were generated every 10nm for the reconstruction, and there might be some sensitivity in the experimental data to an optimal wavelength spacing for PSFs compared to the distance the lens is moved in between frames. Since the data was simulated for multiple wavelengths, the spectral accuracy can be computed from the simulated data. Figure 5.17 shows a graph of the average spectral accuracy (computed $\Delta_\lambda$) as a function of the number of
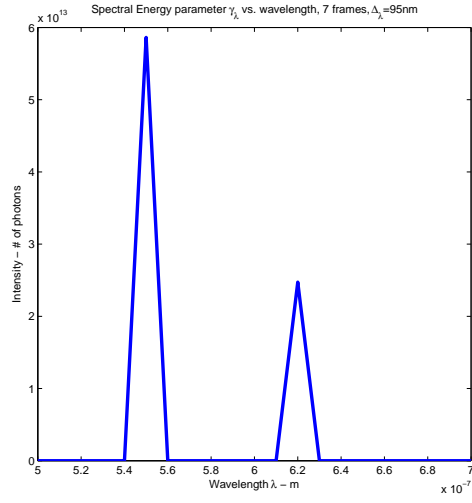
Figure 5.15:     Experimental reconstruction for $\Delta_\lambda$=95nm using 7 frames
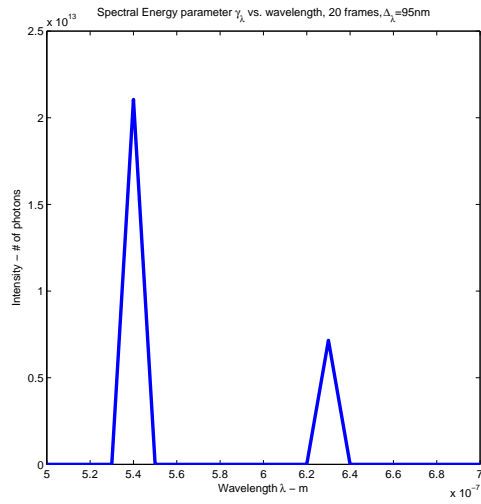


Figure 5.16:     Experimental reconstruction for $\Delta_\lambda$=95nm using 20 frames
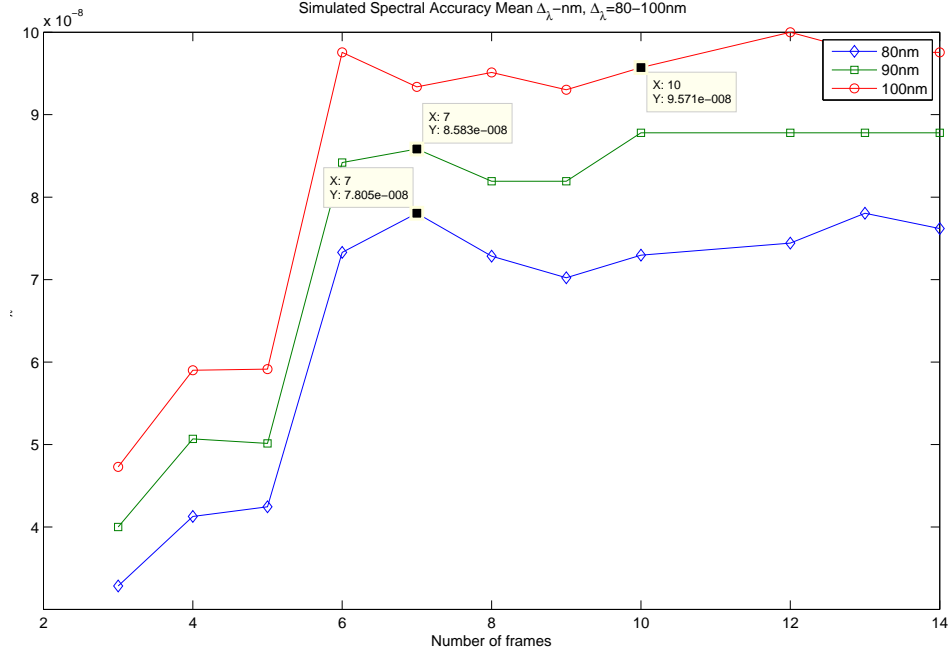
Figure 5.17: Mean simulated spectral accuracy for 80-100nm vs. number of frames

frames. Notice that although the data is close to the simulated $\Delta_\lambda$ value, the values are around $5nm$ away from the actual value even after the data is resolvable. Another metric that can be calculated when examining spectral accuracy is the sum squared error. This is calculated by squaring the difference between $\Delta_\lambda$ and $\widehat{\Delta_\lambda}$ the estimated value. Figure 5.18 shows that the error drops off significantly after $6 - 7$ frames. At less than 6 frames the greater the separation $\Delta_\lambda$, the lower the error. Figure 5.19 that the CRLB bounds the performance of the simulated and experimental results and provides a metric for determining spectral resolution performance. It should be noted that the CRLB has more information than the reconstructor due to the fact that the object structure (2 points) is known for the CRLB. This is required in order to compute the CRLB, but although a two-point reconstructor could be developed it would not be a realistic algorithm for experimental use as it could only detect two-point objects.

84
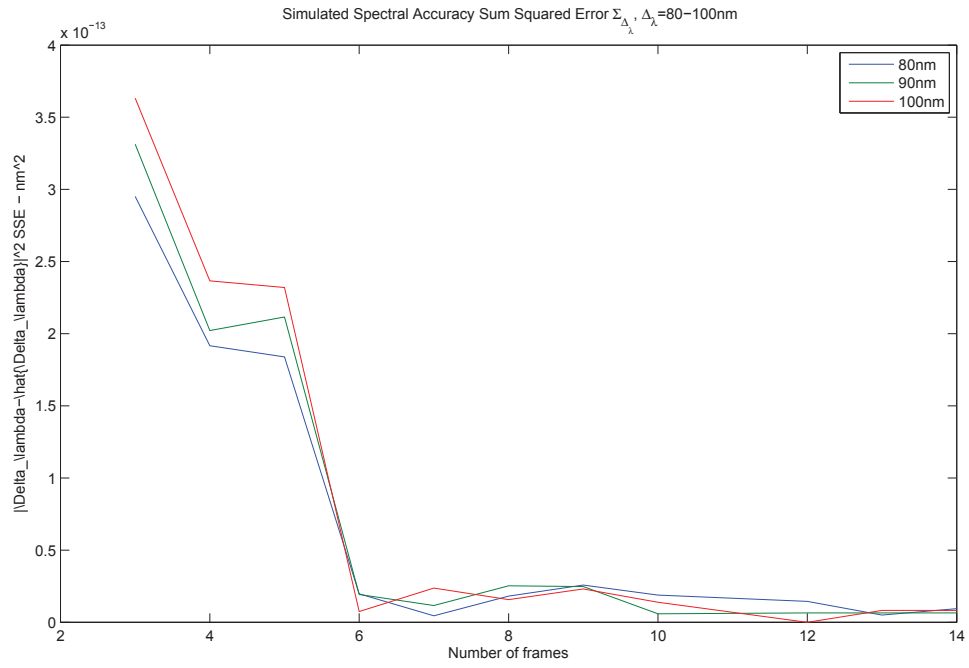
Figure 5.18: Sum Squared Error simulated spectral accuracy for 80-100nm vs. number of frames
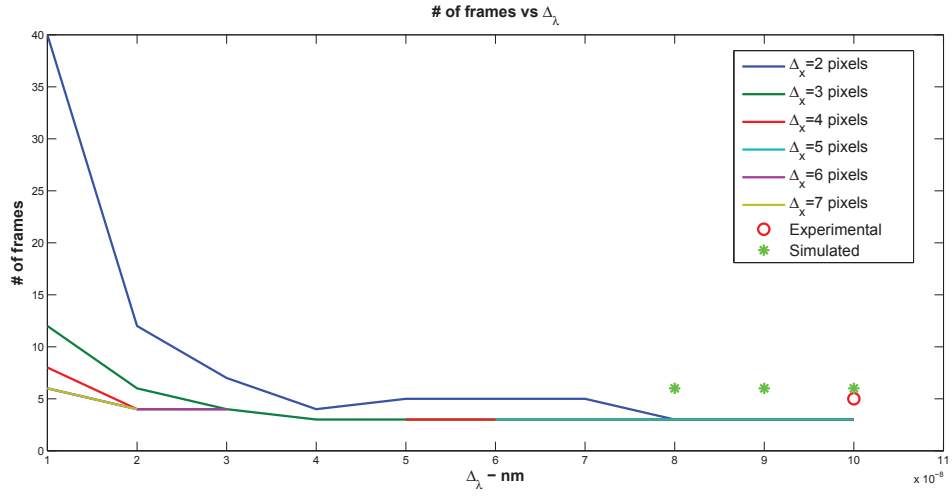


Figure 5.19: CRLB Plotted with Simulation and Experimental results

## 5.5 Lens Point Spread Function Modelling Signal-to-Noise Ratio as Compared to the CRLB

In calculating real results, it is necessary to compare the models to laboratory data. Since the model does not match the real noise also received in the image, the simplified point spread function does not account for everything from the real-world scenario. This section will discuss the quantification of this modelling error and lay the foundation for comparing the Cramer-Rao lower bound to the real experiment. The real PSF in the presence of modelling error is given by:

$$h(x, y) = (g(x, y) + e(x, y)) \tag{5.4}$$

where $g(x, y)$ is the modelled PSF and the image resulting from this noisy PSF (with an ideal object) is:

$$i(x, y) = h(x, y) * o(x, y) \tag{5.5}$$

As we can see from equation (5.4), the PSF has modelling error in it that is not accounted for by the model. This error is then present in the received images used for calibrating the PSF of the lens. Using the deconvolution mentioned above, the estimated point spread function $h'(x, y)$ is calculated which was then used to determine the parameters of the lens. To compare the model to the real PSF we start by normalizing the power in the PSF to unity:

$$h_d(x, y) = \frac{h'(x, y) - E[h'(x, y)]}{\sum_x h'(x, y)} \tag{5.6}$$

Then, the normalized PSF $h_d(x, y)$ is convolved with an ideal object to come up with an estimate of the image with error:

$$i_d(x, y) = h_d(x, y) * o(x, y) \tag{5.7}$$

where $o(x, y)$ is the same object used in the simulation of the CRLB and the simulation and we call the image with error $i_d(x, y)$. Next, the modelled PSF $g(x, y)$ convolved with the ideal object to calculate an estimate of the error-free image.

$$i(x, y) = g(x, y) * o(x, y) \tag{5.8}$$

Finally the estimate of the modelling signal to noise ratio is computed using the mean of the ratio of the image divided by the error. This is done for some small distance around the peak (a square of 10 pixels) to capture signal, and leave out the background.

$$SNR_{model} = E_{x,y} \left[ \frac{i(x, y)}{|i(x, y) - i_d(x, y)|} \right] \tag{5.9}$$

The SNR of the CRLB is calculated using the intensities of the sources divided by the diffuse background intensity.

$$SNR_{CRLB} = E_{x,y} \left[ \frac{i(x, y)}{\sqrt{B}} \right] \tag{5.10}$$

In this case, the $SNR_{model} = 8.24$ and with $o_1 = o_2 = 300$ and $B = 10$, the $SNR_{CRLB} = 3.59$. This compares well and shows that even though the intensity of the experiment was much higher than the signal of the CRLB, the SNR of the modelling error for the experiment compares well with the SNR of the CRLB.

## 5.6    CRLB as a Metric for Lower Bound on Spectral Resolution

This chapter has examined a simulation and laboratory verification of spectral resolution and also examined factors affecting spectral accuracy. The primary factor in this study was determined to be the number of frames. There appears to be a minimum number of frames required in order to resolve two closely-spaced spectral points, beyond which more frames gives little to no additional information. The farther apart these points, the fewer the frames necessary to resolve two points, and the greater the spectral accuracy. A simulation was set up to determine the extent

that these factors affect spectral resolution and spectral accuracy. An experiment was set up and demonstrated the ability of the presented algorithm to extract meaningful color information from a series of defocused frames using chromatic aberration. Also, the trend for more frames to not affect spectral resolution and accuracy beyond 6 frames for this setup was determined by the simulation and verified by the experiment. The CRLB compares well with the simulated and experimental results as shown in section 5.1 where the CRLB was used to determine what effect lens dispersion would have on spectral performance, as well as in section 5.4.2 where the parameter study of the number of frames was compared with both a simulation and an experiment. While the CRLB does not completely characterize the design of a lens-based CTHIS, it can be useful as a method of bounding the effects of various parameters on reconstruction and useful for finding proper parameters to design a sensor. While the analysis of this chapter has focused on a lab-based setup for sensor testing, the next chapter gives a simple study for the lens-based CTHIS in the presence of the atmosphere, which has the potential to significantly degrade the sensor performance and makes it more difficult to use these CTHIS sensors in real-world applications.

# VI. Blind Deconvolution and Hyperspectral reconstruction in the presence of Atmosphere

## 6.1 *Atmospheric Results*

In this section, the algorithm given in section 3.1 is re-derived for a CTHIS in the presence of the effects of atmospheric turbulence. This is a blind deconvolution approach which attempts to determine the seeing parameter of the atmosphere from a series images collected with a known amount of chromatic aberration produced by a lens. The differences for the assumptions from a laboratory setup are discussed in section 6.2. Section 6.3 discusses how the Expectation-Maximization approach for estimating a spectral and spatial scene derived in section 3.1 can be extended to jointly estimate the background and the spatial-spectral object in the presence of an atmospheric Optical Transfer Function (OTF) and also used to estimate the seeing parameter. Finally, section 6.4 discusses the simulation of two scenarios showing the application of this algorithm.

## 6.2 *CTHIS System Design and Modelling*

The model used in (2.26) was strictly based on an assumption of the focal length. A more accurate lens model for a lens-based CTHIS incorporates the index of refraction change with wavelength $n(\lambda)$. The wavelength dependence of the focal length of a typical uncorrected thin lens with equal radii of curvature, $R$, for the front and back surfaces is given by equation (6.1).

$$f(\lambda_l) = \frac{R}{2n(\lambda_l) - 2} \qquad (6.1)$$

In this equation $\lambda_l$ is the wavelength of the light passing through the lens associated with a discrete spectral component indexed by $l$ and $n$ is the index of refraction [11]. As previously, the focal length is assumed known as a function of wavelength, and it is used to define the known point spread function (PSF) of the optical system, $h_{opt}$,

which is approximated by equation (6.2).

$$h_{opt}(x, y, l, k) \approx \left| \sum_{u=1}^{N} \sum_{v=1}^{N} A(u, v) e^{\frac{j\pi}{\lambda} \left( \frac{1}{z_k} - \frac{1}{f(\lambda_l)} \right)(u^2 + v^2)\Delta u^2} e^{-\frac{j2\pi(ux+vy)\Delta x \Delta u}{\lambda_l z_k}} \right|^2 \qquad (6.2)$$

This is the same as previously assumed in (2.24) where $z_k$ is the distance between the lens and the detector plane. The PSF model presented in equation (6.2) is a fairly good approximation of the true function when the object being imaged is far enough away from the system to be considered at infinity [11]. The distance $z_k$ from the lens to the plane where the image is formed for the $k^{th}$ image taken by the sensor, $A$ is the pupil function, $(x,y)$ are sample locations in the detector plane, $(u,v)$ are sample locations in the pupil plane, $\Delta_u$ is the sample spacing in the pupil plane and $\Delta_x$ is the sample spacing in the detector plane. A discrete approximation of the PSF is needed to model the PSF in a computer. The OTF ($H_{opt}$) is the 2-dimensional Fourier transform of the PSF generated using equation (6.2).

Another diffraction related effect is contributed by atmospheric turbulence and can be modelled using an average optical transfer function model. The effective average transfer ($H_{atm}$) in equation (6.3) is for an optical system viewing an object through a long-exposure image viewed through turbulent atmosphere with a seeing parameter of $r_o(\lambda_l)$ [13].

$$H_{atm}(f_x, f_y, l) = e^{-3.44(f_x^2 + f_y^2)\left( \frac{\lambda_l f(\lambda_l)}{r_o(\lambda_l)} \right)^2} \qquad (6.3)$$

In this equation $(f_x, f_y)$ are coordinates in frequency space [10]. The seeing parameter is dependent on which spectral band is used in the model and is assumed to vary with wavelength via the following function:

$$r_o(\lambda_l) = r_o^{\min} \left( \frac{\lambda_l}{\lambda_{\min}} \right)^{6/5} \qquad (6.4)$$

where $\lambda_{min}$ is the minimum wavelength in the pass-band of the optical filter and $r_o^{min}$ is the seeing parameter corresponding to this wavelength. The atmospheric and optical

components of the transfer function combine to form the total transfer function ($H_{tot}$). The total PSF ($h_{tot}(x, y, l, k, r_o^{min})$) is the 2-D inverse FFT of $H_{tot}$.

$$H_{tot}(f_x, f_y, l, k, r_o^{\min}) = H_{opt}(f_x, f_y, l, k)H_{atm}(f_x, f_y, l) \tag{6.5}$$

The images formed by the CTHIS sensor are panchromatic images featuring one wavelength of light in focus and others across the remaining spectral components out of focus to varying degrees. The optical system is modeled as being linear in intensity and wavelength allowing the superposition principle to be used in modeling the signal vectorized by the charge-coupled device (CCD) array. The equation for the sampled projection vector in units of photons, $I$, is shown in equation (6.6).

$$I(m, k) \approx \sum_i \sum_l \sum_x \sum_y o(x, y, l)h_{tot}(i - x, m - y, l, k, r_o^{\min}) \tag{6.6}$$

$$= \sum_l \sum_y o(y, l)h_{tot}(m - y, l, k, r_o^{\min}) \tag{6.7}$$

In this equation, $o$ is the intensity of light in units of photons falling on the detector at any point $(x,y)$ predicted by geometric optics. The variables $(i,m)$ are also detector coordinates in units of samples. An index $l$ indicates which spectral component of the scene is under consideration and $k$ is an index referencing the discrete distance $z_k$ between the lens and the image plane. Note that equations (6.2) and (6.6) are approximations due to modelling both the electro-magnetic spectrum and the images at each spectral component as discrete portions of the true intensity seen on the CCD array. Because of the projection operation and associated dimensionality reduction the model can be simplified in terms of the spectral scene vector, $o$ and the vector impulse response of the system, $h_{tot}$ shown in equation (6.6).

The data gathered by this sensor contains random components as well as those predicted by radiometry and diffraction theory. The noise present on the sensor is assumed to be generated by two components, Poisson noise and read noise. The first is due to the random arrival times of photons in the light itself which is known to have

a Poisson probability mass function. The second is the noise generated from the dark current flowing through the CCD detectors. The expected number of dark counts at each detector pixel $(B)$ is assumed to be unknown at the time of observation and is the mean of a Poisson random variable representing the number of actual dark counts measured at each pixel location. The total signal $D$ measured by the system is shown in equation (6.8). $C(m)$ is a function that is binary in nature and represents an area of the CCD where light passes to the detector array. The purpose of this detector aperture function is to define an area where the signal exists in order to facilitate the estimation of the photo-detector bias without photons from the scene. This can be done in the laboratory with a stop or mask placed before the detector.

$$D(m, z_k) = C(m)I(m, z_k) + B + q_o(m, z) + q_b(m, z) \tag{6.8}$$

### 6.3  Scene Reconstruction and Seeing Parameter Estimation

In this section, the reconstructor previously developed in section 3.1 is extended. The lens-based chromotomagraphic hyperspectral sensor takes a series of images each having a known defocus from the other images. Given the collected image data, the originating scene is unknown so an estimator the must be used. In this case, the unknown parameters are the scene intensity at each pixel location and spectral component, $o(y, l)$, the seeing parameter of the atmosphere $r_o$ and the dark current generated bias signal level at each detector pixel $B$.

The EM algorithm discussed in section 3.1 is applicable to estimating the parameters of interest with a bit of modification. Substituting equation (6.8) into the joint probability of all the data previously derived in section 3.1 (equation (3.16)) the joint probability mass function is shown in equation (6.9).

$$P[D = d \forall (m, k)] = \prod_{m=1}^{N} \prod_{k=1}^{K} \frac{(C(m)I(m, z_k) + B)^{d(m,z_k)}}{d(m, z_k)!} e^{-(C(m)I(m,z_k)+B)} \tag{6.9}$$

The products in equation (6.9) are over the number of pixels in the vertical directions as well as the number of images gathered from the system, $K$. Maximizing this joint probability as a function of the scene, $o$, the pixel bias, $B$ and the seeing parameter $r_o$, is challenging. However, using the EM algorithm (figure 3.1), the previous derivations can be modified to be used in this situation. Previously the background was only computed or directly measured as a constant rather than estimated each iteration. In this setup, the background was jointly estimated with the object. To incorporate a background estimate $B$ into each iteration, we assume the complete data are random variables, $D_1$ and $D_2$ whose means are given by:

$$E[D_1(m, y, l, k)] = C(m)o(y, l)h_{tot}(m - y, l, k, r_o{}^{\min}) \tag{6.10}$$

and

$$E[D_2(m, k)] = B \tag{6.11}$$

where $D_1$ is using the total transfer function and includes the atmospheric seeing parameter $r_o$. The choice to define two distinct sets of complete data is not by any means the only one, but has been shown to be advantageous in other imaging problems. As previously, the complete data are related to the incomplete data via the following transformation.

$$D(m, k) = \sum_{y=1}^{N} \sum_{l=1}^{L} D_1(m, y, l, k) + D_2(m, k) \tag{6.12}$$

This relationship is statistically consistent if the complete data sets are chosen to be independent Poisson random variables since the sum of Poisson random variables is Poisson as well. Also adding together Poisson random variables produces a Poisson whose mean is equal to the means of the random variables being added together. With the statistical model for the complete data in hand, and using the techniques previously discussed in section 3.1, the iterative update solution for the spatial-spectral

object $o(y_o, l_o)$ is given by:

$$o^{new}(y_o, l_o) = o^{old}(y_o, l_o) \sum_k \sum_m \frac{d(m,k)h_{tot}(m - y_o, k, l_o, r_o^{\min})}{(I^{old}(m,k) + B^{old}) \sum_k \sum_m C(m)h_{tot}(m - y_o, k, l_o, r_o^{\min})}.$$

(6.13)

Similar in form, the joint estimation for the background is given by the following update equation:

$$B^{new} = B^{old} \sum_{k=1}^{K} \sum_{m=1}^{M} \frac{d(m,k)}{K(C(m)I^{old}(m,k) + B^{old})}$$

(6.14)

This solution has the advantageous property that the estimated bias level is always positive. The update equations in (6.13) and (6.14) are repeated every iteration until a termination criteria is satisfied. In the case where photon counting noise is the dominant source of error, the following criteria can be used to stop the iteration:

$$\sum_m \sum_k (d(m,k) - C(m)I^{new}(m,k) - B^{new})^2 \leq \sum_m \sum_k d(m,k)$$

(6.15)

This criterion is derived from the relationship between the mean and variance of a Poisson random variable. The left side of the equation is related to the variance of the estimated noise and the left side is related to the sample mean in that both sides are the non-normalized versions of the variance and mean respectively. The iterations continue until either this criterion is met or a maximum number of iterations are reached.

Thus far no mention has been made of how to estimate the seeing parameter, $r_o$, from the imagery. The strategy for estimating the seeing parameter is to execute the EM algorithm for a number of different values of $r_o$ and choose the smallest value for which the convergence criteria is satisfied. The hypothesis for using multiple values of $r_o$ is that if the seeing parameter is too low, the estimated noise will be much larger than the shot noise component. The estimator will then not be able to match the data with a choice of spectral scene in cases where the seeing parameter is too low,

Table 6.1:    System parameters chosen for the simulation

| | | |
|---|---|---|
| Band-Pass Filter Transmission | none | 1 or 0 |
| Band-Pass Filter Bandwidth | nm | 500-690 (10 nm steps) |
| CD array Array Size | pixels | 128 X 128 |
| CCD array Pixel Pitch | mm | 5.0 (center to center) |
| Focusing Optics Diameter | Meters | 0.5 (across the optic) |
| Focusing Optics Focal Length | Meters | 10 (for 500 nm light) |
| Focusing Optics Focal Length | Meters | 10.01 (for 700 nm light) |

due to the limited bandwidth of the impulse response. The mismatch between system bandwidth and data bandwidth produces excess noise which prevents the algorithm from converging. Convergence is possible for larger seeing parameter values. However the larger the seeing parameter is, the lower the bandwidth of the reconstructed spectral scene $o$. Since we desire the sharpest spectral scene reconstruction while still obtaining algorithm convergence, the minimum seeing parameter value that achieves the criterion in equation (6.15) is selected.

## 6.4    Algorithm Performance

The performance of the proposed algorithm is tested using simulated binary source data featuring different separations of the sources in both wavelength and space. Different signal levels are explored as well as different levels of background radiation. In this way the signal to noise ratio of the data can be controlled as different levels of spectral and spatial resolution are investigated. The simulated system used to generate the data is described in subsection 6.4.1 of this chapter. The results obtained from testing the algorithm on the simulated data are shown in subsection 6.4.2.

*6.4.1   Closely Spaced Sources Separated in Wavelength by 100 nm.*    A specific set of system parameters are chosen for simulating realistic CTHIS data. The particular system parameters are consistent with those of a small telescope imaging system. Table 6.1 contains the parameters of the electro-optical system. The simulated system is designed to take 20 vectors sampled at regular intervals as the distance between the
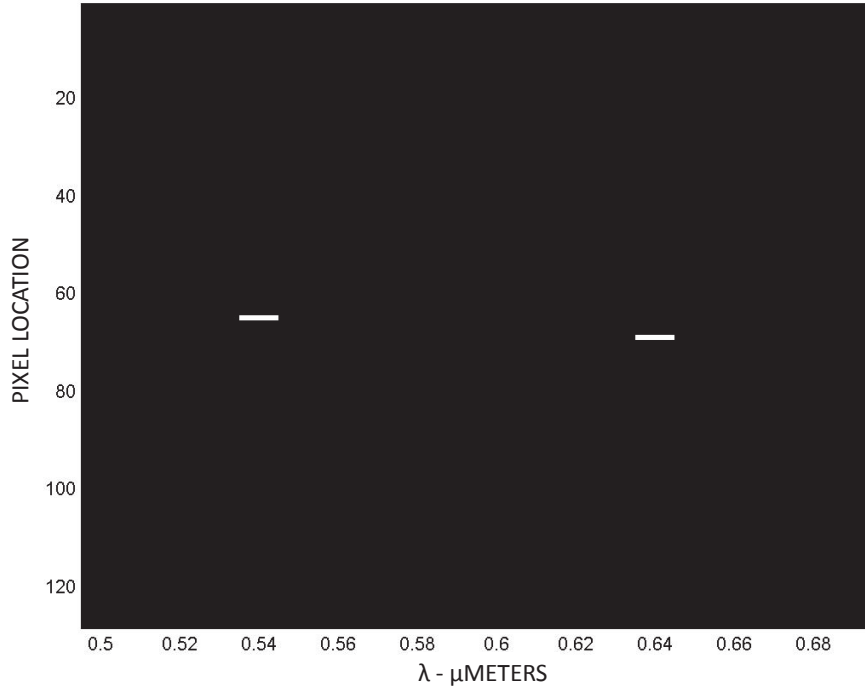
95

Figure 6.1:    2 optical sources in position (Vertical) and wavelength (Horizontal)

lens and the CCD array changes from 10 meters to 10.01 meters. The targets viewed by the system are mono-chromatic sources separated by varying degrees in space and wavelength. The first experiment carried out in this study involves the two sources placed on top of one another, (no physical separation) but separated in wavelength by 100 nanometers. The sources each provide 10000 photo-electrons to the imaging system for each frame taken with 100 photo-electrons of dark current being read out at each detector pixel. The seeing parameter is chosen to be 15 centimeters. Figure 6.1 shows an image of the sources as a function of wavelength and position. Figure 6.2 shows simulated frames of spectral vectors as a function of lens position away from the focal length of 10 m. Figure 6.3 shows the reconstructed spectral image. The algorithm identified the seeing parameter as being equal to 15 centimeters when searching on a range from 10 to 20 cm.

The experiment was repeated for a lower value of signal photons. In this second case the photon level of the sources was dropped to 1000 photons. The raw projection data is shown in Figure 6.5.
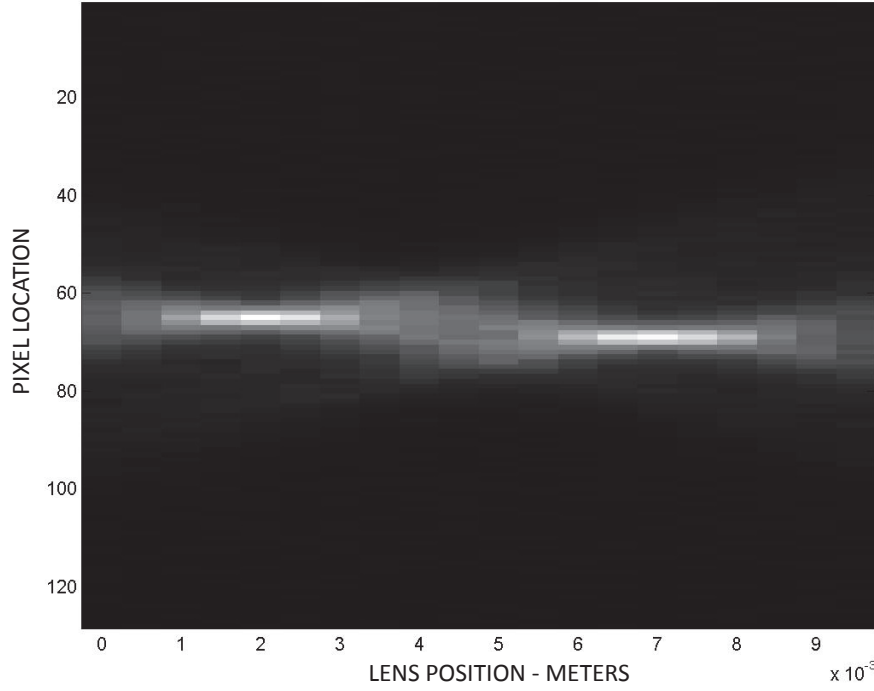
96

Figure 6.2:     Simulation of 2 optical sources as viewed through a lens-based chromo-tomographic imager. The vector projection readout is shown in the columns of the image. Each column corresponds to a frame of data taken at a position marked on the horizontal axis that represents a deviation from the 10 meter position from the primary focusing optic.

The reconstructed spectral projection estimates are shown in figure 6.5. Although the estimated spectral projections are fairly accurate (but demonstrate some additional spectral width), the estimated seeing parameter was 15 cm. The error in the spectral projection estimates due to the lower signal to noise ratio did not affect the algorithm's ability to calculate the correct value for the seeing parameter.

*6.4.2   Sources Separated Only in Wavelength by 40 nm.*     The sources each provide 10000 photo-electrons to the imaging system for each frame taken with 100 photo-electrons of dark current being read out at each detector pixel. The seeing parameter is chosen to be 15 centimeters. Figure 6.1 shows an image of the sources as a function of wavelength and position. Figure 6.6 shows simulated frames of spectral data at the distances where the two sources would be in focus. Figure 6.7 shows the
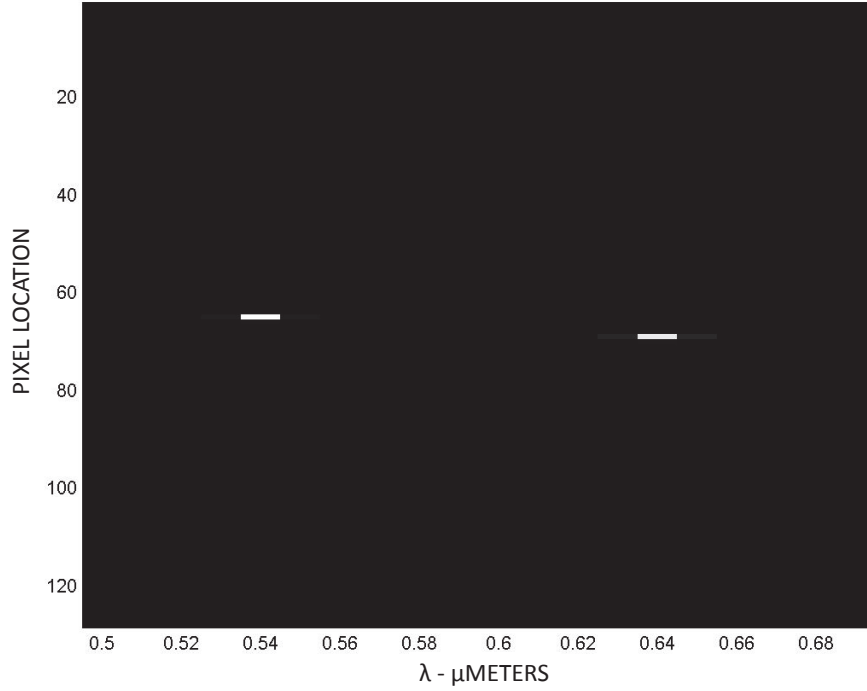
Figure 6.3: Reconstructed spectral image of the two optical sources from the data presented in Figure 6.2. The seeing parameter was estimated to be 15 cm and the true value was 15 cm.

reconstructed spectral image. The algorithm identified the seeing parameter as being equal to 15 centimeters when searching on a range from 10 to 20 cm.

## 6.5 Discussion of Blind Deconvolution of Hyperspectral Data in the presence of Atmosphere

The proposed algorithm for reconstructing spectral projections from chromoto-mographic vector projection data while simultaneously estimating the seeing parameter through which the image data is gathered is demonstrated to work at signal to noise ratios between 30 and 100. The algorithm is presumed to work properly for higher SNR conditions but would require more time to converge thus making that study more time consuming. Further trials need to be conducted to determine the range of signal to noise ratios and achievable spectral resolutions over which the algorithm will perform well. Also, experiments with measured data should be conducted
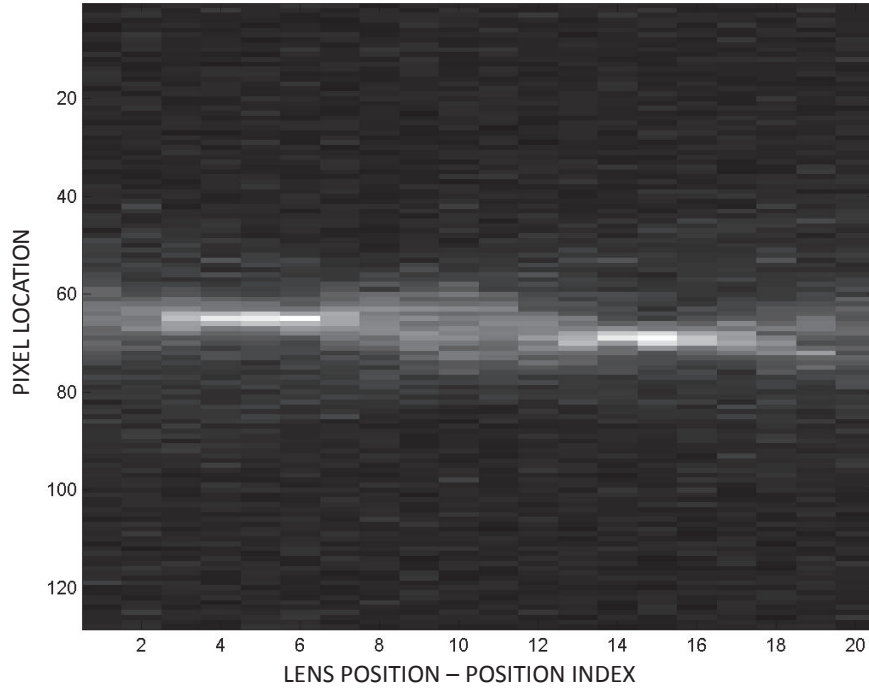
98

Figure 6.4:    Raw projection data for the case where both sources provide 1000 photons during the measurement time and the background level is set at 100 photons.
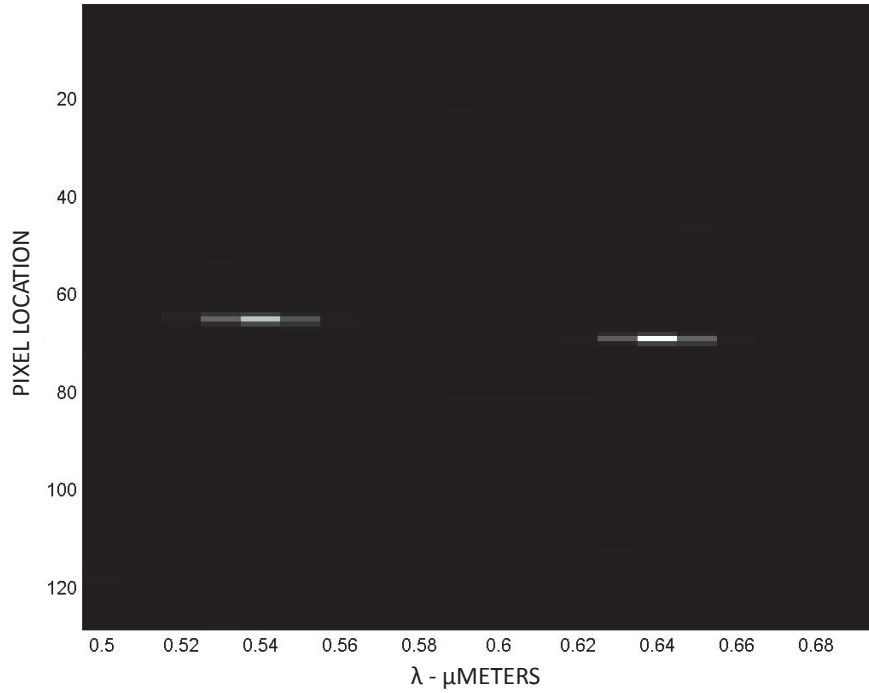


Figure 6.5:    Reconstructed spectral projections for the low SNR case. The spectral features are broadened but still distinguishable.

99

Figure 6.6:    Raw projection data of two objects 4 pixels apart and separated by 40 nanometers in wavelength.

to demonstrate the utility of the algorithm in the presence of modeling error and other unaccounted for but unavoidable effects.

Figure 6.7:    Reconstructed spectral projections of features separated by 40 nanometers.

# VII. Conclusions

This research has examined several factors affecting resolution of a lens-based chromotomographic hyperspectral imaging sensor in the presence of noise. A lower bound 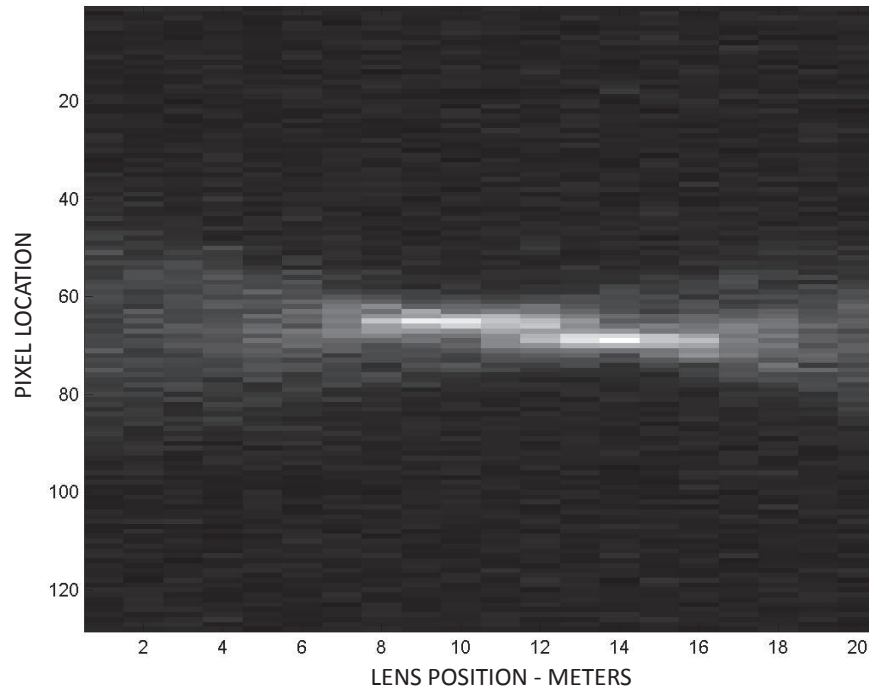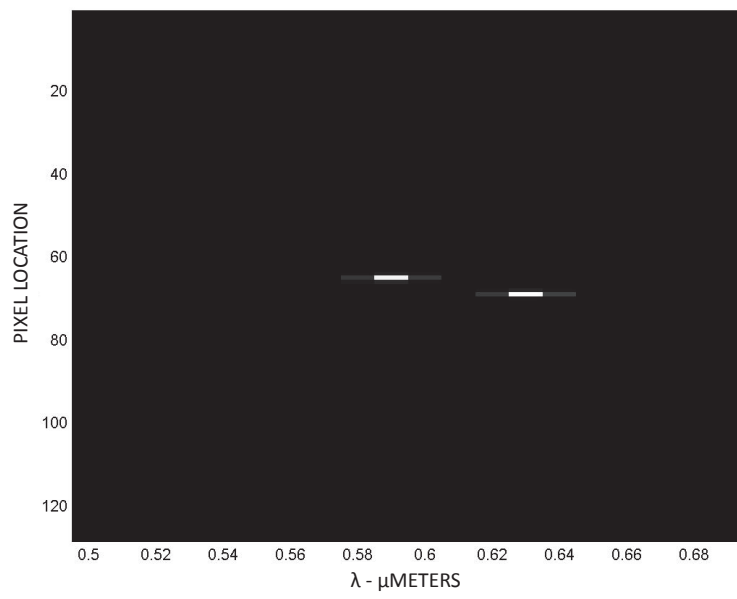on resolution was developed to use as an engineering design tool to determine how changes in sensor design affected resolution. A reconstructor was derived to account for background noise which accounted for a realistic laboratory setup. Finally, a simple experiment was performed and used with the reconstructor to verify the lower-bound and its usefulness as a metric. The effects of the amount of lens chromatic aberration was studied and determined to be a factor, but the most significant factor affecting spectral resolution of a lens-based CTHIS was found to be the number of defocus planes. This number of defocus planes compares well with simulation and the experiment. Also, a modified blind reconstructor was derived in order to account for the presence of atmospheric turbulence. This blind reconstructor estimates jointly the background, the spatial-spectral scene, and the atmospheric seeing parameter for the first time. The algorithm performance was measured using a simple simulation and was found to estimate the seeing parameter well. In the future, this blind estimator could be used to take these sensors from a laboratory environment and make use of existing optical telescopes with this aberration present. Future work should focus on using this sensor in the presence of atmosphere and an experimental test of this algorithm. Further work could also be done on designing a model that incorporates the lower-bound as a test parameter and determining the limits of its applicability to broad sensor system design by changing the parameters and testing them against actual sensors.

## Bibliography

1. "NASA Sensor Completes Initial Gulf Oil Spill Flights", 2010. URL http://www.nasa.gov/topics/earth/features/oil20100527.html. [Online; accessed 23 March 2012 - NASA/JPL-Caltech/Dryden/USGS/UC Santa Barbara].

2. Barrett, H. H. and W. Swindell. *Radiological imaging the theory of image formation, detection and processing*, volume 2. Academic, New York, NY, 1981.

3. Bulygin, F. V., G. N. Vishnyakov, G. G. Levin, and D. V. Karpukhin. "Spectrotomography-a new method of obtaining spectrograms of 2-D objects". *Optical Spectroscopy*, 71(6):561–563, June 1991.

4. Burr, T. and N. Hengartner.

5. Cain, S. "High-throughput dispersive imaging spectromoter for astronomy at visible wavelengths". *Proceedings of the SPIE*, 527–538. Bellingham, WA, 2001.

6. Dempster, A. P., N. M. Laird, and D. B. Rubin. *Journal of the Royal Statistical Society. Series B (Methodological)*, (1).

7. Descour, M. and E. Dereniak. "Computed-tomographic imaging spectrometer - experimental calibration and reconstruction results". *Applied Optics*, 34(22):4817–4826, August 1995.

8. Descour, M. R., C. E. Volin, E. L. Dereniak, T. M. Gleeson, M. F. Hopkins, D. W. Wilson, and P. D. Maker.

9. Gerchberg, R. W. and W. O. Saxton. "A Practical algorithm for the determination of phase from image and diffraction plane pictures". *OPTIK*, 35(2):237–246, 1972.

10. Goodman, J. W. *Statistical Optics*. Wiley Interscience, New York, 2000.

11. Goodman, J. W. *Introudction to Fourier Optics*. Roberts and Company, Greenwood Village, CO, 2005.

12. Gould, M. and S. Cain. "Development of a fast chromotomographic spectrometer". *OE Letters*, 44(11):110503:1–3, November 2005.

13. Hardy, J. W. *Adaptive Optics for Astronomical Telescopes (Oxford Series in Optical & Imaging Sciences)*, volume 2. Oxford University Press, USA, New York, NY, 1998.

14. Johnson, W. R., K. Hege, D. O'Connell, and E. L. Dereniak. "Recovery of a flawed hyperspectral imager calibration using optical modeling". *Optics Express*, 10(12):2251–2257, May 2004.

15. Kalacska, M. and M. Bouchard. "Using Police Seizure Data and Hyperspectral Imagery to Estimate the Size of an Outdoor Cannabis Industry". *Police Practice and Research: An International Jounal*, 12(5):424–434, 2011.

16. Levin, G. G. and G. N. Vishnyakov. "On the possibilities of chronotomography of high speed processes". *Optics Communications*, 56(4):231–234, December 1985.

17. Lyons, D.M. and K. Whitcomb. "Image spectrometry with a diffractive optic". *Proceedings of the SPIE*, 2689(12):274–283, August 1996.

18. Mantravadi, S. and S. Cain. "Analysis and verification of resolution limits of a hyperspectral imager using computed tomography". *Proceedings of the SPIE*. Bellingham, WA, August 2008.

19. Mantravadi, S. V. "Spatial and spectral resolution limits of hyperspectral imagers using computed tomography: A comparison". *IEEE Aerospace Conference Proceedings*. March 2007.

20. Mooney, J. M. and A. K. Brodzik. "Convex projections algorithm for restoration of limited-angle chromotomographic images". *Journal of the OSA*, 16(2):246–257, February 1999.

21. Mooney, J. M., V. E. Vickers, M. An, and A. K. Brodzik. "High-throughput hyperspectral infrared camera". *Journal of the OSA*, 14(11):2951–2961, November 1997.

22. NASA. "Advanced Spaceborne Thermal Emission and Reflection Radiometer spectra". URL `http://asterweb.jpl.nasa.gov`. [Online; accessed 23 March 2012].

23. NASA. "AVIRIS Data Cube", 2000. URL `http://aviris.jpl.nasa.gov/html/aviris.cube.html`. [Online; accessed 23 March 2012].

24. NASA. "What Doesn't Stay in Vegas? Sprawl", 2009. URL `http://www.nasa.gov/topics/earth/features/vegas-sprawl.html`. [Online; accessed 23 March 2012].

25. Okamoto, T., A. Takahashi, and I. Yamaguchi. "Simultaneous Acquistion of Spectral and Spatial Intensity Distribution". *Applied Spectroscopy*, 47(8):1198–1202, March 1993.

26. Okamoto, T. and I. Yamaguchi. "Simultaneous Acquistion of Spectral image information". *Optics Letters*, 16(16):1277–1279, August 1991.

27. Schulz, T. J. "Convex projections algorithm for restoration of limited-angle chromotomographic images". *Journal of the OSA*, 5(10):1064–1073, May 1993.

28. Shepp, L. A. and Y. Vardi. "Maximum likelihood reconstruction for emission tomography". *IEEE Trans. Med. Imag.*, MI-1(2):113–122, 1982.

29. Smith, A. M. and R. E. Blasckshaw. *Geoscience and Remote Sensing Symposium 2002*, volume 4, 1962–1965.

30. Strong, D. *Polarimeter Blind Deconvolution Using Image Diversity.* Ph.D. dissertation, Graduate School of Engineering, Air Force Institute of Technology (AETC), Wright-Patterson AFB OH, March 2007. AFIT/DS/ENG/07-20.

31. Thiessen, B. *Satellite Detection of Cannabis Sativa Outdoor Grow Operations.* In-House TR-04-2007, Defence Research and Development; www.drdc-rddc.gc.ca, Canada, Ottowa, Ont, March 2007.

32. Trees, H. L. Van. *Detection, Estimation and Modulation Theory.* John Wiley & Sons, Inc., New York, NY, 1968.

33. USGS. "USGS Earth Explorer Central Park, New York, NY". URL `http://earthexplorer.usgs.gov/`. [Online; searched for 'Central Park', accessed 23 March 2012].

34. Vandervlugt, C., H. Masterson, N. Hagen, and E. Dereniak. "Reconfigurable liquid crytal dispersing element for a Computed Tomography Imaging Spectrometer". *Proceedings of the SPIE*, 65650O. Bellingham, WA, May 2007.

# *Index*

The index is conceptual and does not designate every occurrence of a keyword. Page numbers in bold represent concept definition or introduction.

# REPORT DOCUMENTATION PAGE

*Form Approved*
*OMB No. 0704–0188*

The public reporting burden for this collection of information is estimated to average 1 hour per response, including the time for reviewing instructions, searching existing data sources, gathering and maintaining the data needed, and completing and reviewing the collection of information. Send comments regarding this burden estimate or any other aspect of this collection of information, including suggestions for reducing this burden to Department of Defense, Washington Headquarters Services, Directorate for Information Operations and Reports (0704–0188), 1215 Jefferson Davis Highway, Suite 1204, Arlington, VA 22202–4302. Respondents should be aware that notwithstanding any other provision of law, no person shall be subject to any penalty for failing to comply with a collection of information if it does not display a currently valid OMB control number. **PLEASE DO NOT RETURN YOUR FORM TO THE ABOVE ADDRESS.**

| 1. REPORT DATE *(DD–MM–YYYY)* | 2. REPORT TYPE | | 3. DATES COVERED *(From — To)* |
|---|---|---|---|
| 14–06–2012 | Doctoral Dissertation | | Sept 2005—Apr 2012 |

| 4. TITLE AND SUBTITLE | 5a. CONTRACT NUMBER |
|---|---|
| Resolution study of a Hyperspectral Sensor using Computed Tomography in the presence of Noise | |
| | **5b. GRANT NUMBER** |
| | **5c. PROGRAM ELEMENT NUMBER** |

| 6. AUTHOR(S) | 5d. PROJECT NUMBER |
|---|---|
| | N/A |
| Mantravadi, Samuel V., Major, USAF | **5e. TASK NUMBER** |
| | **5f. WORK UNIT NUMBER** |

| 7. PERFORMING ORGANIZATION NAME(S) AND ADDRESS(ES) | 8. PERFORMING ORGANIZATION REPORT NUMBER |
|---|---|
| Air Force Institute of Technology<br>Graduate School of Engineering and Management (AFIT/EN)<br>2950 Hobson Way<br>WPAFB OH 45433-7765 | AFIT/DEE/ENG/12-06 |

| 9. SPONSORING / MONITORING AGENCY NAME(S) AND ADDRESS(ES) | 10. SPONSOR/MONITOR'S ACRONYM(S) |
|---|---|
| Air Force Research Laboratory, Optics Division<br>Attn: Dr. Victor Gamiz 3550 Aberdeen Avenue SE<br>Kirtland Air Force Base, NM 87117- 5776<br>(505)846-8464, (DSN: 246-8464), victor.gamiz@kirtland.af.mil | AFRL/RDSAS |
| | **11. SPONSOR/MONITOR'S REPORT NUMBER(S)** |

**12. DISTRIBUTION / AVAILABILITY STATEMENT**

DISTRIBUTION STATEMENT A: APPROVED FOR PUBLIC RELEASE; DISTRIBUTION UNLIMITED.

**13. SUPPLEMENTARY NOTES**

This material is declared a work of the U.S. Government and is not subject to copyright protection in the United States.

**14. ABSTRACT**

Recently, a new type of hyperspectral imaging sensor has been proposed which simultaneously records both spectral data and multiple spatial dimensions. Unlike dispersive imaging spectrometers, chromo-tomographic hyperspectral imaging sensors (CTHIS) record two spatial dimensions as well as a spectral dimension using computed tomography (CT) techniques with only a finite number of spatially-spectrally diverse images. To date, the factors affecting resolution of these sensors have not been examined. This research examines factors affecting resolution, specifically the number of the focus planes needed to resolve a particular object calculated from a theoretical lower bound, determine a method of reconstructing a hyperspectral object in the presence of noise and background and verify the proposed method of reconstruction and the lower bound applying the proposed reconstruction method to laboratory data. Finally, a simple method is proposed and tested to use this sensor in the presence of atmospheric turbulence with a modified reconstructor to blindly estimate the seeing parameter.

**15. SUBJECT TERMS**

Computed Tomography Hyperspectral Imaging Sensor, Cramer Rao Lower Bound, Blind Deconvolution, Atmospheric Turbulence

| 16. SECURITY CLASSIFICATION OF: | | | 17. LIMITATION OF ABSTRACT | 18. NUMBER OF PAGES | 19a. NAME OF RESPONSIBLE PERSON |
|---|---|---|---|---|---|
| a. REPORT | b. ABSTRACT | c. THIS PAGE | | | Stephen Cain |
| U | U | U | UU | 121 | **19b. TELEPHONE NUMBER** *(include area code)*<br>(937) 255–3636, ext 4716 stephen.cain afit.edu |

**Standard Form 298 (Rev. 8–98)**
Prescribed by ANSI Std. Z39.18